

# Quantum non-demolition measurements and quantum simulation

Thesis submitted to the  
Faculty of Mathematics, Computer Science and Physics  
of the Leopold-Franzens University of Innsbruck  
in partial fulfillment  
of the requirements for the degree of

Doctor rerum naturalium

by

**Gerhard Kirchmair**

Innsbruck, July 2010

---

---

# Abstract

Quantum information processing (QIP) has developed into one of the “hot topics” in physics during the last decade. More and more experiments appeared aiming at the realization of a quantum computer and/or quantum simulations. Strings of ions stored in a Paul trap are currently one of the most promising systems for realizing quantum algorithms. The great challenges ion traps are facing is the realization of robust high fidelity operations, scalable traps and the combination of all DiVincenzo criteria in one system.

This thesis reports on the realization of simple QIP sequences and a quantum simulation with trapped  $^{40}\text{Ca}^+$  and  $^{43}\text{Ca}^+$  ions. For both isotopes the quantum bit (qubit) is encoded in an optical transition. It consists of the ground state  $S_{1/2}$  and the metastable excited state  $D_{5/2}$ . The isotope  $^{43}\text{Ca}^+$  has a nuclear spin of  $I = 7/2$  and thus exhibits a very complicated level structure. The advantage of this isotope is that hyperfine levels can be used as a robust memory for quantum information.

In the framework of this thesis a high fidelity Mølmer-Sørensen gate operation was implemented. Two ion Bell states and three ion GHZ states were created with a respective fidelity of 99.3% and 98.4% using  $^{40}\text{Ca}^+$  ions. It was demonstrated that the Mølmer-Sørensen gate operation works nearly as well for ions cooled to the ground state as for ions in thermal states of motion. The fidelity achieved for thermal ions was still 98.4%. A thorough experimental analysis of the gate mechanism indicated possible error sources.

A combination of four DiVincenzo criteria (initialization, long coherence times, a universal set of gates, readout) was realized by utilizing  $^{43}\text{Ca}^+$  hyperfine states. Bell states, created on the optical qubit, were stored in the qubit  $S_{1/2}, F = 4, m_f = 0 \leftrightarrow S_{1/2}, F = 3, m_f = 0$  for 20 ms.

The experience gained with the entangling operation rendered it possible to do non-demolition two-qubit measurements. The non-demolition measurements were used to experimentally test hidden variable theories, more precisely the Kochen Specker theorem. The experiments conducted showed that hidden variables assuming non-contextuality of measurements cannot reproduce the behavior of quantum systems. This was proven by violating an inequality akin to Bell tests. The experimental results also demonstrated the state-independence of the Kochen Specker argument. A possible compatibility loophole was closed by taking into account experimental errors in the theory. The resulting modified equation was found to be violated in our experiments.

Finally, a proof of principle quantum simulation of the Dirac equation was implemented. Position and momentum of the Dirac particle were mapped onto the respective quadrature components of the ion trap harmonic oscillator. A new method to measure the expectation value of position and momentum was implemented. The particle trajectories obtained showed effects like *Zitterbewegung*. Using the high degree of control available in the experiment specific initial states were created showing different trajectories.



---

# Zusammenfassung

Quanteninformationsverarbeitung (QIV) hat sich in eines der meist diskutierten Themen in der Physik im letzten Jahrzehnt entwickelt. Immer mehr Experimente werden gebaut, die darauf abzielen, einen Quantencomputer oder Quantensimulator zu realisieren. Besonders Ionen, gespeichert in einer Paul-Falle, gehören zu den vielversprechendsten Systemen, um Quanten-Algorithmen zu realisieren. Die großen Herausforderungen, die es bei Ionenfallen zu lösen gilt, sind die Realisierung von Quantengattern mit hoher Güte, der Bau von skalierbaren Fallen und die Kombination aller DiVincenzo Kriterien in einem System.

Die vorliegende Arbeit beschreibt die Realisierung von einfachen Sequenzen zur QIV und zu Quanten-simulation mit  $^{40}\text{Ca}^+$  und  $^{43}\text{Ca}^+$  Ionen. Bei beiden Isotopen erfolgt die Kodierung des Quanten-Bits (Qubit) in einem sogenannten optischen Qubit, bestehend aus dem Grundzustand  $S_{1/2}$  und dem metastabilen angeregten Zustand  $D_{5/2}$ . Das Isotop  $^{43}\text{Ca}^+$  hat einen Kernspin von  $I=7/2$  und daher ein sehr kompliziertes Termschema. Der Vorteil dieses Isotops ist, dass Hyperfein Niveaus, sogenannte "Uhrenübergänge", als robuste Speicher für Quanteninformation verwendet werden können.

Im Rahmen dieser Doktorarbeit wurde ein Mølmer-Sørensen Gatter hoher Güte realisiert. Es wurden mit diesem Gatter Bell-Zustände mit einer Güte von 99.3% und GHZ-Zustände, bestehend aus drei Ionen, mit einer Güte von 98.4% hergestellt. Weiters wurde gezeigt, dass das Mølmer-Sørensen Gatter auch mit Ionen funktioniert, die nicht in den Grundzustand gekühlt wurden. Die erreichte Güte unter diesen Voraussetzungen betrug immer noch 98,4%. Mögliche Fehlerquellen der Gatter Operation wurden durch eine gründliche Untersuchung quantifiziert.

Durch Verwendung von  $^{43}\text{Ca}^+$  Hyperfein-Zuständen war es möglich, vier der fünf DiVincenzo Kriterien (Initialisierung, lange Kohärenzzeiten, universeller Satz an Gattern, Zustands- Detektion) in einem System zu vereinen. Bell Zustände, die auf dem optischen Qubit erzeugt wurden, konnten ins Hyperfein-Qubit  $S_{1/2}, F = 4, m_F = 0 \leftrightarrow S_{1/2}, F = 3, m_F = 0$  übertragen werden und für mehr als 20 ms gespeichert werden.

Die mit den Gatter Operationen gewonnene Erfahrung ermöglichte die Realisierung von nicht destruktiven Quantenmessungen. Diese nicht-destruktiven Messungen wurden dazu verwendet um sogenannte Theorien versteckter Variablen zu testen. Die durchgeführten Experimente zeigten, dass Theorien versteckter Variablen, aufbauend auf nicht kontextuellen Messungen, quantenmechanische Systeme nicht richtig beschreiben. Dies wurde gezeigt durch Verletzung einer Ungleichung sehr ähnlich der Bellschen Ungleichung. Weiters ergaben die Messungen, dass die Verletzung der Ungleichung unabhängig vom Quantenzustand ist. Das Kompatibilitätsschlupfloch wurde geschlossen durch Einbeziehen der experimentellen Fehler in die Theorie.

Letztendlich wurde eine Quantensimulation der Dirac Gleichung experimentell realisiert. Ort und Impuls des simulierten Teilchens wurden auf die betreffende Quadraturkomponente des har-

monischen Oszillators abgebildet. Eine neue Methode wurde verwendet, um den Erwartungswert des Orts und Impuls des simulierten Teilchens zu bestimmen. Die gemessene Teilchentrajektorien zeigten relativistische Effekte wie *Zitterbewegung*. Durch Ausnützen der außergewöhnlichen experimentellen Kontrolle konnten verschiedene Anfangszustände erzeugt werden die unterschiedliche Trajektorien zeigten.

---

# Contents

<b>Abstract</b>	<b>i</b>
<b>Zusammenfassung</b>	<b>iii</b>
<b>1. Introduction</b>	<b>1</b>
<b>2. Trapped calcium ions as qubits</b>	<b>5</b>
2.1. Quantum computation and quantum bits . . . . .	5
2.2. Quantum harmonic oscillator and phase space . . . . .	10
2.3. Atomic Structure . . . . .	13
<b>3. Laser-ion interaction</b>	<b>19</b>
3.1. Ion laser Hamiltonian . . . . .	19
3.2. Non-resonant interactions . . . . .	21
3.3. The $S_{1/2} \rightarrow D_{5/2}$ transition . . . . .	23
3.4. Microwave transitions . . . . .	25
3.5. Mølmer-Sørensen gate . . . . .	25
3.6. Creating a coherent displacement . . . . .	30
<b>4. Experimental setup</b>	<b>33</b>
4.1. Linear ion trap and electrode wiring . . . . .	33
4.2. Vacuum vessel . . . . .	35
4.3. Magnetic field coils . . . . .	36
4.4. Optical access and single ion addressing . . . . .	36
4.5. Fluorescence detection . . . . .	37
4.6. Laser system . . . . .	40
4.7. Computer control and RF generation . . . . .	45
<b>5. Experimental techniques</b>	<b>47</b>
5.1. Loading ions by photoionization . . . . .	47
5.2. Experimental sequence . . . . .	48
5.3. Referencing the 729 nm laser to the ions . . . . .	51
5.4. Implementation of arbitrary qubit operations and ion shuttling . . . . .	52
5.5. State tomography . . . . .	55

<b>6. Entangling calcium ions</b>	<b>57</b>
6.1. High fidelity two ion Bell states . . . . .	57
6.2. Three ion entangled states and arbitrary operations on three qubits . . . . .	67
6.3. High fidelity entanglement of $^{43}\text{Ca}^+$ hyperfine clock states . . . . .	70
6.4. Comparison between $^{40}\text{Ca}^+$ and $^{43}\text{Ca}^+$ . . . . .	74
<b>7. Experimental test of quantum contextuality</b>	<b>77</b>
7.1. The Kochen-Specker theorem . . . . .	78
7.2. Experimental realization of QND measurements . . . . .	81
7.3. Testing the Kochen Specker inequality . . . . .	83
7.4. Including imperfect measurements to close loopholes . . . . .	86
7.5. Experimental results on imperfect measurements . . . . .	89
<b>8. Quantum simulation of the Dirac equation</b>	<b>91</b>
8.1. Introduction . . . . .	91
8.2. The Dirac equation . . . . .	92
8.3. Experimental realization . . . . .	94
<b>9. Summary and Outlook</b>	<b>101</b>
<b>A. The Kochen Specker measurements</b>	<b>105</b>
A.1. Detailed results for the Kochen Specker measurements . . . . .	105
A.2. Hiding the second ion in the Kochen Specker measurements . . . . .	106
<b>B. Methods for simulating the Dirac equation</b>	<b>107</b>
B.1. Constructing a pure negative energy spinor . . . . .	107
B.2. Setting the phase of the Displacement pulse . . . . .	107
<b>C. Physical and optical properties of Calcium</b>	<b>109</b>
<b>D. Journal Publications</b>	<b>111</b>

---

# 1. Introduction

Quantum mechanics (QM) was among the greatest developments in the twentieth century. The foundations of this theory were established around 1925 by Werner Heisenberg, Erwin Schrödinger, Max Born, Wolfgang Pauli, Niels Bohr, Albert Einstein, Paul Dirac and many others. Initially invented for a better understanding of atomic spectra, quantum mechanics opened the door to a completely new field in physics. Nowadays it successfully explains chemical processes, material behavior and semiconductor devices, enabling the development of the modern computer technology. Computers in turn helped to numerically solve quantum mechanical problems which could not be solved analytically. In the following decades physicists realized that this approach has its limits as quantum systems consisting of only a few quantum bits (qubits) are already impossible to simulate with current computer technology.

In the early 1980's Paul Benioff [1] and Richard Feynman [2] came up with the idea of simulating one quantum system by using another one. This so called quantum computer would only need an amount of qubits on the same order as the simulated system. Back in the 80's these ideas were considered as mere "Gedankenexperimente" and not as realistic scenarios that could be developed into experiments. It was considered impossible to use a single atom as a carrier for quantum information. Richard Feynman said in a lecture in 1986: "*... we are to be even more ridiculous later and consider bits written on one atom instead of the present  $10^{11}$  atoms. Such nonsense is very entertaining to professors like me. I hope you will find it interesting and entertaining also.*"

Today such procedures are experimental routine and quantum information processing as well as quantum simulation are major research fields in theoretical and experimental physics. The big interest was sparked by the discovery of a factorization algorithm on a quantum computer, which is much faster than its classical counterpart, by Peter Shor in 1994 [3]. A large scale experimental realization of this algorithm would render public key encryption useless. Two years later Lov K. Grover found that a quantum computer can search unsorted databases faster than a classical computer [4]. Barenco et. al. [5] as well as DiVincenzo [6] showed in 1995 that an arbitrary quantum algorithm can be constructed with a limited set of single and two-qubit gates. This "universal" set of operations is similar to the classical approach of constructing logic circuits out of NAND gates. To actually build a quantum computer certain prerequisites have to be met. These requirements were formulated by DiVincenzo [7] and are often called *DiVincenzo criteria*, according to which any quantum computer implementation requires

1. A scalable physical system with well characterized qubits
2. The ability to faithfully initialize the qubit to a simple well defined state
3. Long relevant coherence time, much longer than the gate operation time
4. A "universal" set of quantum gates

## 5. Qubit specific measurement capability

Later two additional requirements were added to incorporate quantum communication between distant nodes of a quantum network

## 6. The ability to interconvert stationary and flying qubits

## 7. The ability to faithfully transmit flying qubits between specified locations

Throughout the last decade research has shown that there are several experimental implementations that fulfill most or even all of these points and might be considered as candidates for a quantum computer: nuclear spins [8], superconducting Josephson junctions [9, 10], quantum dots [11], neutral atoms [12], photons [13] and ions [14]. While nuclear spins are the most advanced system when it comes to an actual implementation of algorithms and the number of qubits [15], they suffer from the inability to create pure states. This prevents scaling of this technology to higher numbers of quantum bits. Solid state implementations offer the promise of easy scalability akin to integrated circuits as soon as one is able to reliably manufacture and control the basic building blocks. In the last few years these devices made remarkable progress realizing Bell states [16], two-qubit gates [17] and quantum process tomography [18]. The limiting factor at the moment is the coherence time of a few microseconds [19]. Recent experiments with neutral atoms demonstrated the extraordinary control physicists have over single atoms [20] and ultracold ensembles [21]. These systems seem to be good candidates for quantum simulations of solid state models [22].

One of the most promising systems for realizing a quantum computer are trapped ions [23]. They already fulfilled three of the five DiVincenzo criteria even before they were considered as a system for quantum information processing (QIP): initialization [24], readout [25–27] and long coherence times [28]. Laser-cooled strings of ions had been observed [29–31] qualifying as well characterized qubits which could be used as a quantum register. The trapping of charged particles in electric fields was first proposed by K.H. Kingdon in 1923 [32]. Radio frequency traps were developed by Wolfgang Paul in the 1950's and a single ion was trapped the first time by Neuhauser et al. in 1980. The trapping of ions had a huge influence on atomic physics and sparked the development of optical clocks and mass spectrometers. Furthermore it opened up the possibility of controlling well-isolated quantum systems for processing quantum information. This point was first noticed in the seminal paper by Peter Zoller and Ignacio Cirac in 1995 [14]. They proposed to use the collective motion of an ion string as a bus system to couple individual ions. A series of laser pulses acting on one ion at a time can be used to realize a two-qubit gate. This approach is also scalable as the resources increase only polynomially with the number of qubits. Within the same year a two-qubit gate was demonstrated [33] with a single ion which set the starting point for quantum information processing with trapped ions.

In the last years ion trap experiments have shown a tremendous control of experimental parameters. This control was the key to demonstrate the first steps towards a quantum computer and/or quantum simulations. Meanwhile all seven DiVincenzo criteria have been achieved in at least proof of principle experiments. Some of the milestones are the investigation of several two-qubit gates [34–40], deterministic quantum teleportation with atoms [41, 42], quantum error correction [43], entanglement purification [44], the creation of six [45] and eight ion entangled states [46]

---

and the implementation of simple algorithms like the Deutsch-Josza algorithm [47] and Grover's search algorithm [48]. Along the way, several analysis techniques were developed like quantum state tomography and quantum process tomography [49, 50]. The so called decoherence-free subspace was investigated [51] and universal ion-trap quantum computation with decoherence-free qubits was realized [52]. Ions trapped in separate traps have been entangled [53] and quantum teleportation has been demonstrated [54] fulfilling the additional DiVincenzo criteria.

Today the big challenges on the road towards an ion trap quantum computer are the following: scaling current technology to a few ten or hundred qubits; combining all building blocks in one system; improving all operations to enter the *fault tolerant regime*. Scaling the trap technology to a high number of ions is a difficult but important task as for a real commercially useful implementation of Shor's factoring algorithm some  $10^5$  qubits are needed. Several research groups are currently constructing and testing miniaturized traps but progress is slow. Recent experiments have demonstrated the combination of the basic DiVincenzo criteria in one experiment [55, 56].

Entering the *fault tolerant regime* is important for realizing a large scale quantum computer capable of doing arbitrary long quantum algorithms. For this purpose quantum error correction protocols similar to classical computation are indispensable. The first protocols were discovered by Peter Shor [57] and Andrew Steane [58]. Furthermore, Peter Shor showed that it is possible to realize quantum algorithms with arbitrarily small errors even when using imperfect operations [59]. This is possible as soon as all operations enter the *fault tolerant regime* which means errors below  $10^{-2} \dots 10^{-4}$ . The exact threshold depends on the overhead in the number of qubits one is willing to accept [60–62].

Even though all building blocks for an ion trap quantum computer have been demonstrated it will still take time until a large scale functioning quantum computer will become reality. Nevertheless, ion trap systems might soon outperform classical computers when it comes to quantum simulations. Here the demands on the quality of the operations and the number of qubits is much less. Decoherence might be even used to mimic the effect of an environment. Recently a proof of principle experiment showed the simulation of a quantum magnet [63], demonstrating a phase transition from a paramagnetic to a ferromagnetic order with two-qubits. Another proof of principle experiment, the simulation of the free Dirac equation will be presented in chapter 8. So even relativistic quantum effects might be simulated with a quantum computer. Soon experiments will be able to control and do simulations with 10-20 interacting qubits which is already a next to impossible problem for a classical computer.

The high control over experimental parameters in ion traps opens up the possibility to do fundamental tests of QM. These tests are important as it is still debated whether quantum mechanics can be explained with so called *hidden variable models*. Hidden variables were introduced as some physicists were unhappy with the Copenhagen interpretation of quantum mechanics which only predicts the probabilities for the outcome of a measurement. Another intriguing attribute of QM are its nonlocal features, e.g. a measurement of two entangled particles shows correlations which are bigger than classically possible. This was first discovered by Einstein, Podolsky and Rosen in their famous paper from 1935 [64]. This point led physicists to the conclusion that QM is incomplete and other unknown physical phenomena beyond QM have to be included. In 1964 John Bell showed that hidden variable theories have to be non local to explain all effects of quantum mechanics [65].

He presented his famous Bell inequality which is satisfied by local hidden variables but violated by QM. Several experiments have meanwhile proven that QM violates Bell's inequality [66–69]. Another class of hidden variable theories are non-contextual theories which are the subject of a theorem developed by Kochen, Specker and Bell [70–72] in the 60's. Recent experiments [73–75], one of them presented in Chapter 7, have shown that also this model cannot explain QM. So far it seems there is no better theory than QM covering all observed phenomena.

The thesis is structured as follows: Chapter 2 contains a review of the main ideas and terms of quantum information processing followed by a quick review of the quantum harmonic oscillator. The level structure of  $^{40}\text{Ca}^+$  and  $^{43}\text{Ca}^+$  ions is described and possible choices for qubits are illustrated. Chapter 3 summarizes the interaction of the ions with electromagnetic fields with a special focus on the Mølmer-Sørensen entangling gate. Chapter 4 describes the apparatus consisting of the vacuum chamber, the lasers and the electronic control. Chapter 5 explains standard experimental techniques necessary for running the apparatus and realizing the experiments presented in the subsequent chapters. Chapter 6 describes the realization of an entangling operation working on  $^{40}\text{Ca}^+$  and  $^{43}\text{Ca}^+$  ions. Bell states with fidelities as high as 99.3% were created and the gate operation was analyzed in detail. Furthermore we achieved an entanglement of  $^{40}\text{Ca}^+$  ions in thermal states of motion and a mapping of the entanglement from the optical qubit onto the hyperfine qubit in  $^{43}\text{Ca}^+$ . Finally three-ion entangled states with  $^{40}\text{Ca}^+$  were created and the first block of a new scheme for universal quantum computation with trapped ions was implemented. Chapter 7 details on a test of the non-contextual hidden variable theory proposed by Kochen, Specker and Bell in a two ion system. Data are presented that demonstrate that QM measurements are contextual even in the presence of experimental noise. Chapter 8 describes the realization of an experiment with a single ion simulating the free Dirac equation. The particle position measured as a function of time shows Zitterbewegung and other relativistic effects. Chapter 9 concludes the thesis with a summary and outlook to future experiments.

The main findings of this thesis were published in the references [75–78].

---

## 2. Trapped calcium ions as qubits

This chapter will quickly review the mathematical notation for a two-level system and the basic ideas of quantum computation. The mathematical excursus is continued by a description of a quantum harmonic oscillator with an emphasis on canonical variables and the phase space description. The energy level structure of the Calcium isotopes  $^{40}\text{Ca}^+$   $^{43}\text{Ca}^+$  will be outlined and a number of possible implementations of a qubit in calcium ions will be shown.

### 2.1. Quantum computation and quantum bits

Inspired by [79] this section will present the mathematical description of a two-level system and will give a brief summary on quantum computation. It will introduce the notions “qubit“ and “entanglement“ as well as single and two-qubit operations.

#### 2.1.1. Qubits

For a real physical implementation of a quantum computer, quantum information has to be stored and manipulated. Akin to classical computation we will make use of two states of a system. These states will represent the quantum states  $|\downarrow\rangle$  and  $|\uparrow\rangle$  instead of the logical 0 and 1. In trapped ions, a qubit can be realized by identifying two long-lived atomic states with the qubit states  $|\downarrow\rangle$  and  $|\uparrow\rangle$ . The main difference from the classical case is that the system cannot only be in one of the two states but also in a linear superposition

$$|\Psi\rangle = \alpha |\downarrow\rangle + \beta |\uparrow\rangle \quad (2.1)$$

with  $\alpha$  and  $\beta$  complex numbers and the normalization condition  $|\alpha|^2 + |\beta|^2 = 1$ . Such a two-level system is called *quantum bit/qubit* in analogy to the classical case. The numbers  $|\alpha|^2$  and  $|\beta|^2$  represent the probability of measuring the qubit in state  $|\downarrow\rangle$  or  $|\uparrow\rangle$ . A single measurement will just show either  $|\downarrow\rangle$  or  $|\uparrow\rangle$ . Only by many repetitions the full information about a quantum state can be acquired.

A convenient and often used form of rewriting equation (2.1) is

$$|\Psi\rangle = \cos\left(\frac{\theta}{2}\right) |\downarrow\rangle + \sin\left(\frac{\theta}{2}\right) e^{i\phi} |\uparrow\rangle \quad (2.2)$$

where a global phase factor was dropped that is not observable in experiments. Thus a pure quantum state is completely described by two real numbers  $\theta$  and  $\phi$ . This representation allows us to visualize the qubit’s state on sphere a with unit radius, where  $\theta$  and  $\phi$  are the rotation angles of the *Bloch vector*. This sphere, called *Bloch sphere*, is shown in figure 2.1.

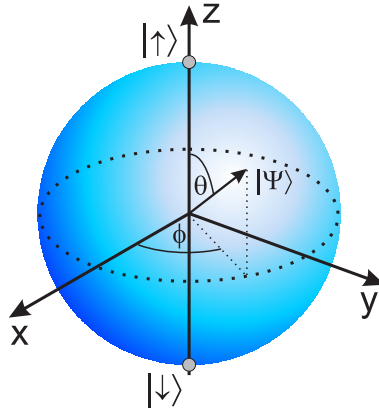


**Figure 2.1.:** Bloch sphere representation of a pure qubit state  $|\Psi\rangle$  described by the rotation angles  $\theta$  and  $\phi$ .

The state description can be extended to N-qubits by using a set of basis states composed of the  $2^N$  product states

$$|n\rangle = |i_N\rangle \otimes \dots \otimes |i_2\rangle \otimes |i_1\rangle \quad (2.3)$$

with  $i \in \{0, 1\}$ . With the vectors  $|n\rangle$  we can now describe every possible state consisting of N qubits as

$$\Psi_N = \sum_{n=0}^{2^N-1} \alpha_n |n\rangle \quad (2.4)$$

where the state amplitudes  $\alpha_n$  have to satisfy the normalization condition  $\sum_{n=0}^{2^N-1} |\alpha_n|^2 = 1$ . Unfortunately, the convenient Bloch sphere representation is not extendable to more than one qubit.

### 2.1.2. Quantum gates

A universal language to describe quantum algorithms is the quantum circuit model. In analogy to classical computing, where a computation is built up of logic gates, in this model a quantum computation consists of concatenations of elementary quantum operations acting on the qubits. It can be shown, that there exists a small set of single qubit operations and a universal two-qubit gate that can be used to perform arbitrary quantum algorithms [79].

The simplest interaction acting on an N-qubit system is a single qubit operation. These operations have to preserve the norm of the state and can be conveniently described by using the Pauli matrices plus the Identity matrix

$$\sigma_x = \begin{pmatrix} 0 & 1 \\ 1 & 0 \end{pmatrix}, \quad \sigma_y = \begin{pmatrix} 0 & -i \\ i & 0 \end{pmatrix}, \quad \sigma_z = \begin{pmatrix} 1 & 0 \\ 0 & -1 \end{pmatrix}, \quad \hat{I} = \begin{pmatrix} 1 & 0 \\ 0 & 1 \end{pmatrix}. \quad (2.5)$$

In the Bloch sphere representation, single qubit operations can be described as a rotation around the x, y, z axis or an arbitrary axis  $\phi$  in the equatorial plane by an angle  $\theta$ . The rotation matrixes

## 2.1 Quantum computation and quantum bits

---

are given by

$$U_x^{(j)}(\theta) = e^{-i\frac{\theta}{2}\sigma_x} = \begin{pmatrix} \cos\frac{\theta}{2} & -i\sin\frac{\theta}{2} \\ -i\sin\frac{\theta}{2} & \cos\frac{\theta}{2} \end{pmatrix} \quad (2.6)$$

$$U_y^{(j)}(\theta) = e^{-i\frac{\theta}{2}\sigma_y} = \begin{pmatrix} \cos\frac{\theta}{2} & -\sin\frac{\theta}{2} \\ \sin\frac{\theta}{2} & \cos\frac{\theta}{2} \end{pmatrix} \quad (2.7)$$

$$U_z^{(j)}(\theta) = e^{-i\frac{\theta}{2}\sigma_z} = \begin{pmatrix} e^{-i\frac{\theta}{2}} & 0 \\ 0 & e^{i\frac{\theta}{2}} \end{pmatrix} \quad (2.8)$$

$$U^{(j)}(\theta, \phi) = e^{-i\frac{\theta}{2}\sigma_\phi} = \begin{pmatrix} \cos\frac{\theta}{2} & -ie^{-i\phi}\sin\frac{\theta}{2} \\ -ie^{i\phi}\sin\frac{\theta}{2} & \cos\frac{\theta}{2} \end{pmatrix}, \quad (2.9)$$

where  $\sigma_\phi = \cos(\phi)\sigma_x + \sin(\phi)\sigma_y$  and  $j$  denote the ion subject to the rotation. Setting  $\phi = 0$  in  $U^{(i)}(\theta, \phi)$  results in a  $U_x^{(i)}(\theta)$  rotation and similarly setting  $\phi = \pi/2$  results in  $U_y^{(i)}(\theta)$ . If we can apply these rotations to every qubit of our quantum computer it is sufficient to introduce one particular type of multi-qubit operation to construct all arbitrary operations. There are many different choices for universal gate operations. The best known example is the *controlled*-NOT (CNOT) operation where the state of the target qubit is flipped or not depending on the state of the control qubit. The matrix representation of this operation is

$$U_{CNOT} = \begin{pmatrix} 1 & 0 & 0 & 0 \\ 0 & 1 & 0 & 0 \\ 0 & 0 & 0 & 1 \\ 0 & 0 & 1 & 0 \end{pmatrix} \quad (2.10)$$

where the matrix is notated with respect to the basis order  $\{|\downarrow\downarrow\rangle, |\downarrow\uparrow\rangle, |\uparrow\downarrow\rangle, |\uparrow\uparrow\rangle\}$ . Another important two-qubit operation is the Mølmer-Sørensen [80, 81] (MS) gate operation. This gate was implemented in this thesis and will be further discussed theoretically in chapter 3 and experimentally in chapter 6. Its matrix representation is

$$U_x^{MS}\left(\frac{\pi}{2}\right) = e^{-i\frac{\pi}{4}\sigma_x \otimes \sigma_x} = \frac{1-i}{2} \begin{pmatrix} 1 & 0 & 0 & i \\ 0 & 1 & -i & 0 \\ 0 & -i & 1 & 0 \\ i & 0 & 0 & 1 \end{pmatrix}. \quad (2.11)$$

This gate introduces collective spin flips on two ions and can be extended to an N-qubit gate (see chapter 3.5). The normalization factor in front of the matrix is required because two-qubit operations have to preserve the norm such that  $U_{gate}^\dagger U_{gate} = \hat{I}$ . The Mølmer-Sørensen gate is completely equivalent to a CNOT operation up to some single qubit rotations.

### 2.1.3. Quantum state measurement

At the end of a quantum algorithm/simulation during which the system evolved according to a unitary operation the outcome needs to be determined. This requires a detection of the qubit states by a projective measurement. Its experimental implementation for the case of trapped ions will be

discussed in chapter 4.5. Mathematically this process can be described by a set of measurement operators  $\{M_m\}$  such that the results  $m$  of a measurement occur with a probability

$$p(m) = \langle \Psi | M_m^\dagger M_m | \Psi \rangle. \quad (2.12)$$

The state of the system after the measurement is one of the eigenstates of the measurement operator

$$|\tilde{\Psi}\rangle = \frac{M_m |\Psi\rangle}{\sqrt{\langle \Psi | M_m^\dagger M_m | \Psi \rangle}} \quad (2.13)$$

The natural measurement basis for trapped ions are the projectors onto the energy eigenstates. Thus one can only measure the  $\sigma_z$  components of every qubit state  $\Psi$  by a simple fluorescence detection. If projections onto other spin components  $A = \vec{n}\vec{\sigma}$  are of interest (where  $\vec{n}$  is the direction of the desired spin component) a modified technique has to be employed.

The measurement basis can be changed by applying a unitary state transformation  $U$  prior to the state detection on each qubit individually. This means the subspace  $\mathcal{H}_A^+ = \{\psi | A\psi = \psi\}$  is mapped onto the subspace  $\mathcal{H}_{\sigma_z}^+ = \{\psi' | \sigma_z \psi' = \psi'\}$ . Thus a  $\sigma_z$  measurement on the transformed state  $|\Psi'\rangle = U|\Psi\rangle$  is equivalent to a measurement of the desired observable  $A$  on the original state  $|\Psi\rangle$ . The unitary state transformation  $U$  satisfies

$$A = U^\dagger \sigma_z^i U \quad (2.14)$$

and is given by a rotation around an axis on the Bloch sphere that is both perpendicular to  $\vec{e}_z$  and to  $\vec{n}$ . The final inverse operation  $U^\dagger$  maps the projected state onto an eigenstate of the observable  $A$  which is in general not necessary. Nevertheless it becomes important when one is interested in doing non-demolition measurements in succession (see chapter 7). The mapping on an eigenstate ensures that subsequent commuting measurements will still determine the right value.

An additional complication appears if e.g. a spin correlation like  $\sigma_z \otimes \sigma_z$ , the so called *parity*, of a two ion state should be measured. If exactly this observable should be determined in a non-demolition measurement it is necessary to apply entangling two-qubit gates together with single qubit operations, that map this information on a single qubit. An example for such an operation  $U$  is a CNOT gate which will map the parity of the two ions on the state of the target ion.

initial state	mapped state	initial state	mapped state
		$\sigma_z \otimes \sigma_z$	$I \otimes \sigma_z$
$ \downarrow\downarrow\rangle$	$ \downarrow\uparrow\rangle$	$(-1) \cdot (-1) = +1$	+1
$ \downarrow\uparrow\rangle$	$ \downarrow\downarrow\rangle$	$(-1) \cdot 1 = -1$	-1
$ \uparrow\downarrow\rangle$	$ \uparrow\downarrow\rangle$	$1 \cdot (-1) = -1$	-1
$ \uparrow\uparrow\rangle$	$ \uparrow\uparrow\rangle$	$1 \cdot 1 = +1$	+1

By measuring only the state of the second ion after the mapping, it is ensured, that the parity measurement reveals a single bit of information. It is important to note, that such a measurement is not equivalent to measuring  $\sigma_z$  on every ion and correlating the results afterwards to get  $\sigma_z \otimes \sigma_z$ . In the latter case one would not only get the information whether the ions are in the same or opposite spin state but also in which state each ion is.

### 2.1.4. Entanglement

Called *Spooky Action at a Distance* [64] by Einstein, Podolsky and Rosen, entanglement brings up some of the most striking features of quantum mechanics. Let us consider an entangled state for two qubits, the so called *Bell state*

$$|\Psi\rangle = \frac{|\uparrow\uparrow\rangle + |\downarrow\downarrow\rangle}{\sqrt{2}} \quad (2.15)$$

which was created in several experiments described in this thesis (see chapter 6). Whenever the state of one qubit of this entangled state is measured, one will find a perfectly correlated result when measuring the other. If the first qubit is in the state  $|\downarrow\rangle/(|\uparrow\rangle)$  the second qubit will be in  $|\downarrow\rangle/(|\uparrow\rangle)$  or vice versa so both qubits will always be found in the same state. This behavior will violate one or both of the assumptions Einstein and Co. made for a *physical realistic theory*:

- *Realism*: The assumption that the physical properties of a system have definite values which exist independent of observation
- *Locality*: The assumption that a measurement on one particle does not influence the result of the measurement on the second particle.

These assumptions seem to be intuitively plausible but nevertheless experiments conducted with these states [66] show that they disobey the so called Bell inequality [72]. This then leads to the conclusion that they have to disobey one or both of the upper points. There is still a lot of discussion going on about the results of these experiments that go beyond the scope of this work. More information about this subject can be found in references [82–84].

A more rigorous criterion for entangled states can be phrased as: *A state is entangled if its composite wavefunction cannot be written as a product of wavefunctions of the subsystems.* Mathematically this means

$$|\Psi_{AB}\rangle \neq |\Psi_A\rangle \otimes |\Psi_B\rangle. \quad (2.16)$$

Creating entangled states is nowadays a standard procedure which can be employed in several different physical systems [46, 85–87]. A single application of a Mølmer-Sørensen-gate to  $|\downarrow\downarrow\rangle$  creates already an entangled state of the form shown in equation (2.15) They can be used as resources for secure quantum communication [88] or certain types of quantum computation [89]. Entanglement seems to appear in most quantum algorithms however it is still a matter of debate if the power of an algorithm comes from entanglement or not.

In chapter 7 of this thesis another peculiar feature of quantum-mechanics, the so called *contextuality* of measurements, will be discussed. *Contextuality* of measurements means that certain types of measurements influence another even though they should not. The states measured inherit entanglement not from the beginning but entanglement will be created during the measurement process. Entanglement plays a central role in quantum mechanics.

### 2.1.5. Density matrix description

So far the description of a qubit is sufficient for pure states but fails for states which are mixed or not completely known. Here the density operator language provides a convenient means to describe these systems. All postulates for quantum mechanics regarding state description, state

evolution and measurement can be reformulated in terms of density operators [79]. For a system which can be in pure states  $\Psi_i$  with a probability  $p_i$  the density operator is given by

$$\rho = \sum_i p_i |\Psi_i\rangle \langle \Psi_i|. \quad (2.17)$$

One has to note that the probabilities  $p_i$  are only well defined for an ensemble of states. A density matrix has to satisfy the conditions

1. the trace of  $\rho$  is equal to one
2.  $\rho$  is a positive operator.

For a  $d$ -dimensional quantum system it is possible to expand the density matrix  $\rho$  using a basis of  $d^2$  hermitian matrices that are mutually orthogonal. A handy choice for a single qubit are the Pauli matrices together with the identity

$$\rho = \frac{1}{2} \sum_{i=x,y,z,\hat{I}} \lambda_i \sigma_i. \quad (2.18)$$

The parameters  $\lambda_i$  which completely characterize the state are given by

$$\lambda_i = Tr\{\rho \sigma_i\}. \quad (2.19)$$

So each of these parameters corresponds to the outcome of a projective measurement determining the expectation values of the Pauli operators  $\langle \sigma_i \rangle$ . This will become handy for reconstructing the quantum state in the experiment with a technique called state tomography (chapter 5). As one can see from equation (2.20) it is sufficient to determine all  $\lambda_i$  to get the full knowledge of a quantum state. The parameters  $\lambda_i$  uniquely define a vector on the Bloch sphere (similar to figure 2.1) but not only the angles but also the length of the vector is now of importance. The length of the vector is given by  $\sum_{x,y,z} \lambda_i^2$  and it shows the purity of a state. A pure state has a unit length vector, a partially mixed state has a vector with a length smaller than 1 and a completely mixed state has a vector with a length equal to zero.

This description can be straightforwardly extended to multi-qubit systems. The density matrix for a  $N$ -qubit system is written in terms of tensor products of the Pauli matrices

$$\rho_N = \frac{1}{2^N} \sum_{i_1, i_2, \dots, i_N, =x,y,z,\hat{I}} \lambda_{i_1, i_2, \dots, i_N} \sigma_{i_1} \otimes \sigma_{i_2} \otimes \dots \otimes \sigma_{i_N}. \quad (2.20)$$

Normalization requires that  $\lambda_{I,I,\dots,I} = 1$  such that  $4^N - 1$  parameters define the state in the Hilbert-space. Each  $m_{i_1, i_2, \dots, i_N}$  corresponds again to a projective measurement determining  $\langle \sigma_{i_1} \otimes \dots \otimes \sigma_{i_N} \rangle$ .

## 2.2. Quantum harmonic oscillator and phase space

An ion in a trap is one of the best model systems for a perfect quantum harmonic oscillator. Usually the harmonic oscillator is only used to mediate interactions between the ions but is not

## 2.2 Quantum harmonic oscillator and phase space

---

regarded by itself as an interesting system. In chapter 8 it will be shown that using a single ion in the harmonic oscillator of the trap one can conduct a simulation of the Dirac Equation. The information of the position and the momentum of the Dirac particle will be encoded in the position and momentum observables of the harmonic oscillator. Hence this section will revivie the analysis of a quantum harmonic oscillator with an emphasis on the phase space description. At the end a classical driving force will be introduced and the effects on the state of the oscillator will be shown. This chapter is strongly inspired by [37, 90, 91].

### 2.2.1. Harmonic oscillator hamiltonian

A quantum harmonic oscillator is a particle of mass  $m$  moving in a 1-d quadratic potential  $V(x_c) = m\omega^2 x_c^2/2$ . Classically the state of a harmonic oscillator is defined by its position and momentum coordinates  $x_c$  and  $p_c$ . A classical harmonic oscillator is best described in phase space which is given by the complex plane spanned by the variable  $x_c + ip_c$ . The motion of the particle can be described by a point in phase space which is rotating with an angular frequency  $\omega$  along an ellipse centered at the origin. In quantum mechanics the position and momentum will be replaced by the observables  $\hat{x}$  and  $\hat{p}$ . They obey the commutation relation

$$[\hat{x}, \hat{p}] = i\hbar. \quad (2.21)$$

With these operators the Hamiltonian for a quantum harmonic oscillator reads as

$$H_m = \frac{\hat{p}^2}{2m} + \frac{1}{2}m\omega^2 \hat{x}^2. \quad (2.22)$$

Introducing the non-hermitian operator  $a$  and its conjugate  $a^\dagger$  such that

$$\hat{x} = (a + a^\dagger)\Delta \quad \text{and} \quad \hat{p} = i\frac{a^\dagger - a}{2}\frac{\hbar}{\Delta} \quad (2.23)$$

with the characteristic length  $\Delta = \sqrt{\hbar/(2m\omega)}$  one can rewrite equation (2.22) and arrive at the well known quantized version of the harmonic oscillator Hamiltonian

$$H_m = \hbar\omega \left( a^\dagger a + \frac{1}{2} \right). \quad (2.24)$$

The spectrum of this Hamiltonian is a ladder of equidistant energy levels  $E_N$  with a spacing of  $\hbar\omega$  starting at the ground state energy of  $E_0 = \hbar\omega/2$ . The corresponding wavefunctions  $|N\rangle$  are called *Fock States* and will obey the following relations

$$a^\dagger |n\rangle = \sqrt{n+1} |n+1\rangle \quad (2.25)$$

$$a |n\rangle = \sqrt{n} |n-1\rangle \quad (2.26)$$

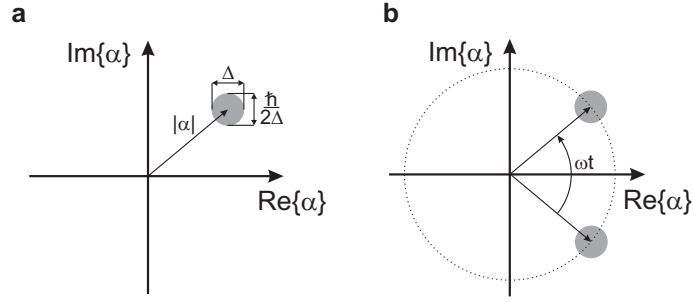


**Figure 2.2.:** (a) Phase space representation of a coherent state  $|\alpha\rangle$ . The coordinates of the center of the disk correspond to  $\langle x\rangle$  and  $\langle p\rangle$ . The size of the disk represents the variance of the state here with unit length along  $p$  and  $x$ . (b) Time evolution of a coherent state. The state rotates with the trap frequency  $\omega$  around the origin.

and

$$a^{\dagger n} |0\rangle = \sqrt{n!} |n\rangle \quad (2.27)$$

$$a^{\dagger} a |n\rangle = n |n\rangle. \quad (2.28)$$

Often  $a$  and  $a^{\dagger}$  are called lowering and raising operators, because they can be used to climb up and down the ladder of states. The spatial extension of the ground state  $|0\rangle$  is given exactly by  $\Delta$ .

## 2.2.2. Driven quantum harmonic oscillator

If a harmonic oscillator is driven by a classical force

$$F(t) = A \sin(\omega_{drive}t + \phi) = \frac{A}{2i} (e^{i(\omega_{drive}t + \phi)} - e^{-i(\omega_{drive}t + \phi)}) \quad (2.29)$$

the Hamiltonian is given by

$$H_{force} = -\hat{x}F(t). \quad (2.30)$$

The action of this force on the ground state of the harmonic oscillator can be best explained by changing into the interaction picture. A suitable transformation to do this is given by  $U|\Psi\rangle = |\Psi'\rangle$  with  $U = e^{iH_m t/\hbar}$ . The Hamiltonian in the interaction picture then reads as

$$H_{force}^i = -\Delta(ae^{-i\omega t} + a^{\dagger}e^{i\omega t})F(t). \quad (2.31)$$

For  $\omega = \omega_{drive}$  a resonance appears and using the rotating wave approximation the Hamiltonian reduces to

$$H_{force}^i = -\frac{A\Delta}{2i} (ae^{-i\phi} + a^{\dagger}e^{i\phi}) \quad (2.32)$$

The evolution of the ground state under the action of this Hamiltonian is given by the unitary operator

$$D(\alpha) = e^{\alpha^* a - \alpha a^{\dagger}} \quad (2.33)$$

## 2.3 Atomic Structure

---

with  $\alpha = -A\Delta t/(2\hbar)e^{-i\phi}$ . This propagator is a so called *displacement operator*. Applying it to the ground state of motion creates the coherent state  $|\alpha\rangle$

$$D(\alpha)|0\rangle = |\alpha\rangle = e^{-|\alpha|^2/2} \sum_n \frac{\alpha^n}{\sqrt{n!}} |n\rangle. \quad (2.34)$$

This can be generalized to cover the displacement of a coherent state  $|\beta\rangle$  by using the Baker–Campbell–Hausdorff relation  $D(\alpha)D(\beta) = D(\alpha + \beta)e^{i \operatorname{Im}\{\alpha\beta^*\}}$

$$D(\alpha)|\beta\rangle = D(\alpha)D(\beta)|0\rangle = e^{i \operatorname{Im}\{\alpha\beta^*\}}|\alpha + \beta\rangle. \quad (2.35)$$

A coherent state obeys the following relations

$$a|\alpha\rangle = \alpha|\alpha\rangle \quad (2.36)$$

$$\langle\alpha|a^\dagger = \alpha^*\langle\alpha| \quad (2.37)$$

and

$$\langle\alpha|\hat{x}|\alpha\rangle = 2\Delta \operatorname{Re}\{\alpha\} \quad (2.38)$$

$$\langle\alpha|\hat{p}|\alpha\rangle = \frac{\hbar}{\Delta} \operatorname{Im}\{\alpha\}. \quad (2.39)$$

The real part of  $\alpha$  corresponds to the mean position while the imaginary part corresponds to the mean momentum. A convenient way to display these states is a phase space diagram (see figure 2.2(a)) with  $\alpha = \langle\hat{x}\rangle + i\langle\hat{p}\rangle$  with  $x$  in units of  $2\Delta$  and  $p$  in units of  $\hbar/\Delta$ . The variance for position and momentum is also given by  $\Delta$  as

$$\delta x = \Delta \quad \text{and} \quad \delta p = \frac{\hbar}{2\Delta}. \quad (2.40)$$

A coherent state is the closest analogy to classical states one can achieve for a quantum harmonic oscillator and is hence called *quasi-classical state*. The state evolution, a rotation in phase space (see figure 2.2(a)), cannot be seen in ion trap experiments because the laser creating the displacement acts as a reference oscillator rotating with the coherent state. How to create a displacement operator with laser fields will be explained in chapter 3.

## 2.3. Atomic Structure

There are several ways to experimentally realize a good approximation of a two-level system. Ideally the ion has to be completely separated from the environment and should only interact with the laser. Experimentally this means, that the laser-ion coupling has to be much larger than any coupling to the environment. A suitable choice for a qubit are either hyperfine/Zeeman ground states or states connected by a forbidden transition. The element used to realize a qubit in this thesis is the single charged alkali earth ion  $\text{Ca}^+$ . This section describes the relevant level structure of the two isotopes  $^{40}\text{Ca}^+$  and  $^{43}\text{Ca}^+$  as well as the qubits realized in these ions. A more detailed description of  $^{40}\text{Ca}^+$  can be found in [92] and [93] whereas for  $^{43}\text{Ca}^+$  the reference is [94].

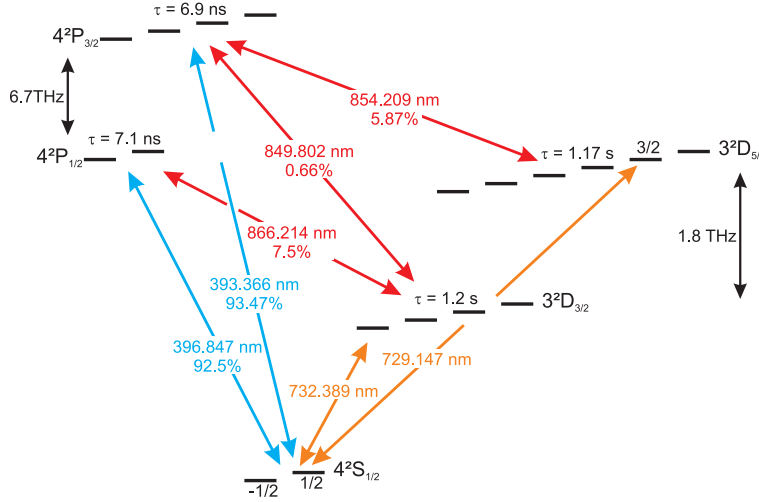


**Figure 2.3.:** Detailed energy level scheme showing all Zeeman sublevels of the three lowest orbitals of the  $^{40}\text{Ca}^+$  ion. Laser light at 397 nm is used for Doppler-cooling, optical pumping and detection. The lasers at 866 nm, 850 nm and 854 nm pump out the D-states. An ultra-stable laser at 729 nm is used for manipulating the qubit encoded in the quadrupole transition, state preparation, optical shelving and ground-state cooling. The qubit is encoded in the states  $S_{1/2}(m_j = 1/2)$  and  $D_{5/2}(m_j = 3/2)$ . The wavelength in air, natural lifetimes  $\tau$  and the branching fractions (denoted as XX% for the respective transition) are taken from references [95–98].

## Level scheme, Zeeman splitting and qubit choice

The coarse level structure for  $^{40}\text{Ca}^+$  and  $^{43}\text{Ca}^+$  is the same. The energy level schemes showing the lowest three orbitals of the valence electron for  $^{40}\text{Ca}^+$  and  $^{43}\text{Ca}^+$  can be seen in figure 2.3 and figure 2.4. The  $S_{1/2}$  ground state is connected via a 397 nm dipole transition with the  $P_{1/2}$  state and a 393 nm dipole transition with the  $P_{3/2}$  state. The P-levels both having a lifetime of about 7 ns exhibit a branching ratio such that one out of 14 decays populates the D-levels.<sup>1</sup> To avoid population trapping in the long lived D-states one can use the dipole transitions at 854 nm, 850 nm and 866 nm to pump out these levels. These wavelengths connect the two D-states to either a  $P_{1/2}$  or  $P_{3/2}$  level via a dipole transition. A quadrupole transition at 729 nm connects the  $S_{1/2}$  and the  $D_{5/2}$  level. Since this transition is dipole-forbidden, the  $D_{5/2}$  level is metastable and has a lifetime of about 1.2 s which sets an upper time limit for the usefulness of a qubit encoded in this state.

## Calcium 40

In a magnetic field all levels split up into sublevels due to the Zeeman effect (see figure 2.3). The splitting of the states is a few MHz for the magnetic fields typically used in experiments. Thus it is well resolved for the quadrupole transition. For all the other transitions the splitting is hidden within the linewidth of the transition. The  $S_{1/2}$  ground state splits up in two Zeeman sublevels with  $m_S = \pm 1/2$  and the  $D_{5/2}$  level splits up in six Zeeman sublevels with  $m_D = \pm 1/2, \pm 3/2, \pm 5/2$ . For

<sup>1</sup>An exact measurement of the  $P_{3/2}$  branching ratio measurements using QIP methods can be found in reference [95].

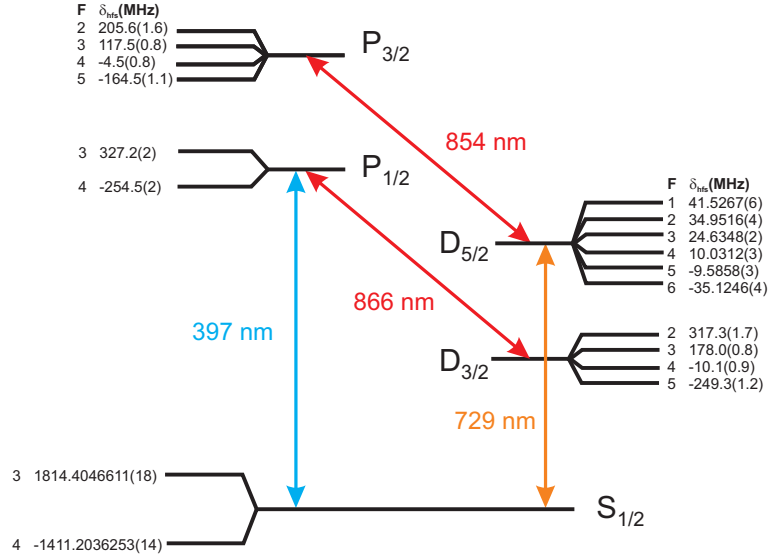


**Figure 2.4.:**  $^{43}\text{Ca}^+$  level scheme showing the hyperfine splitting of the lowest energy levels. Hyperfine shifts  $\delta_{hfs}$  of the levels are quoted in MHz (the splittings are taken from [94, 99, 100]). Laser light at 397nm is used for Doppler-cooling, optical pumping and state detection. The lasers at 866 nm, 850 nm and 854 nm pump out the D-states. An ultra stable laser at 729 nm is used for manipulating the qubit encoded in the quadrupole transition, state preparation, optical shelving and ground-state cooling.

a quadrupole transition changes in the magnetic quantum number of  $\Delta m = 0, \pm 1, \pm 2$  are allowed by the selection rules. This results in a total of ten possible transitions from  $S_{1/2}$  to  $D_{5/2}$ .

One of these pairs of levels, the  $S_{1/2}, m_j = 1/2$  together with the  $D_{5/2}, m_j = 3/2$  was used as a qubit for the experiments described in this thesis. The only exception to this choice are some of the experiments presented in chapter 6.1 where the  $S_{1/2}, m_j = 1/2$  level together with the  $D_{5/2}, m_j = 5/2$  level was used. These kinds of qubit are often termed *optical qubits* because the transition frequency lies in the optical domain. As already mentioned, the sensitivity of the qubit on the environment, here especially magnetic field fluctuations, is of importance. The dependence of the transition frequency on the magnetic field  $B$  is given by

$$\Delta\omega_{S \rightarrow D} = \mu_B (m_s g_{S_{1/2}} - m_D g_{D_{5/2}}) B \quad (2.41)$$

where  $\mu_B$  denotes the Bohr magneton and  $g_{S_{1/2}}/g_{D_{5/2}}$  the Lande-g-factor of the  $S_{1/2}/D_{5/2}$  level. In the best case the lowest sensitivity one could get with respect to changes in the magnetic field is 560kHz/G for the  $\Delta m = 0$  transitions which are usually used as a qubit. The employed  $S_{1/2}, m_j = 1/2 \rightarrow D_{5/2}, m_j = 3/2$  transition has a factor of two higher dependence but comes with the advantage that the coupling strength can be maximized by properly setting the polarization and direction of the laser light with respect to the magnetic field (see chapter 3). This effectively reduces the time needed for operations.

## Calcium 43

The isotope  $^{43}\text{Ca}^+$  is the only stable calcium isotope with a non-zero nuclear spin. It has a nuclear spin of  $I = 7/2$ . Its level scheme is shown in figure 2.4. The coupling between electronic angular momentum  $J$  and nuclear spin results in a hyperfine structure. The total angular momentum  $F$  can take on the values  $|J - I| \leq F \leq |J + I|$ . For the ground state of  $^{43}\text{Ca}^+$  we get two hyperfine states with  $F=3$  and  $F=4$  split by a frequency difference of 3.225 GHz [99]. The D state with  $J = 5/2$  consists of 6 hyperfine states ranging from  $F=1$  to  $F=6$ . In a magnetic field all hyperfine levels split up in  $2F + 1$  Zeeman states.

This huge state manifold opens up several possibilities to encode a qubit. Two choices are implemented in the experiments conducted in this thesis. An encoding in the two hyperfine ground states termed *hyperfine qubit* or, similar to  $^{40}\text{Ca}^+$ , an encoding using an optical qubit.

The first choice is interesting because there is no limitation by spontaneous decay. Furthermore we can get a qubit which is insensitive to magnetic field fluctuations by choosing the  $m_F = 0$  sublevels of the two hyperfine ground states. This particular qubit was implemented in this thesis (see chapter 6). From the *Breit-Rabi* formula [101] one can directly obtain that these sublevels exhibit no first order Zeeman shift. However the linear dependence vanishes only for zero magnetic field. For a finite field the differential shift is given by a second order approximation as [94]

$$\Delta\omega_{0 \rightarrow 0} = \frac{(g_J - g_I)^2 \mu_B^2}{2\hbar \Delta E_{hfs}} B^2 \simeq 2\pi \cdot 1.2 \text{ kHz/G}^2 \cdot B^2 \quad (2.42)$$

with the nuclear g-factor  $g_I$  accounting for the complex structure of the nucleus and the Landé factor

$$g_J \simeq 1 + \frac{J(J+1) + S(S+1) - L(L+1)}{2J(J+1)}. \quad (2.43)$$

This means that for a typical magnetic field of 4 G the magnetic field sensitivity is 19.2 kHz/G which is much lower than for the best transition in  $^{40}\text{Ca}^+$ . An additional advantage of hyperfine qubits is that the transition frequency is in the GHz range so that the transition can be directly addressed with a  $\mu$ -wave field. Stable frequency sources with computer controlled power, phase and frequency are readily available. If additional single ion addressing is required, one can switch to a Raman laser setup as the microwave field cannot be focused. The two laser beams for the Raman setup can be derived from the same laser source. The frequency splitting is achieved by frequency shifting the light fields with acousto-optical modulators which ensures phase coherence. An example for the implementation of a Raman laser with  $^{43}\text{Ca}^+$  ions can be found in [94] and [102]. In this thesis the hyperfine qubit is solely manipulated by a microwave field.

The second choice, an optical qubit manipulated on the quadrupole transition is also appealing. Although one is still limited by the finite lifetime of the D-state one can find transitions which are insensitive to magnetic field fluctuations. This is due to the additional coupling of the nuclear magnetic moment to the electron spin and the magnetic field which modifies equation (2.41). The transition frequencies depend in a nonlinear way on the magnetic field which gives rise to a number of different transitions which are insensitive to magnetic field fluctuations at a non zero magnetic field. A good example is the  $S_{1/2}, F = 4, m_F = 4 \rightarrow D_{5/2}, F = 4, m_F = 3$  transition which becomes field insensitive at 3.38 G and 4.96 G with a second-order Zeeman shift of  $\mp 16 \text{ kHz/G}^2$ .

## 2.3 Atomic Structure

---

A much more detailed explanation of the hyperfine splitting in  $^{43}\text{Ca}^+$  and the interaction with static magnetic fields is given in [94]. Although the optical qubit in  $^{43}\text{Ca}^+$  is insensitive to magnetic field variations one should not forget that the coherence on all optical qubits is still limited by the line width of the laser mediating the coupling. With the currently available quadrupole laser the coherence time for a single ion is limited to about 8 ms (see chapter 4.6.2).

In the experiment two different qubits on the quadrupole transition were realized. One qubit was realized using the levels  $S_{1/2}, F = 4, m_F = 0 \leftrightarrow D_{5/2}(F = 6, m_F = 1)$  at a magnetic field of 6 G. The second qubit was realized using the levels  $S_{1/2}, F = 4, m_F = 0 \leftrightarrow D_{5/2}(F = 4, m_F = 2)$  at a magnetic field of 3.4 G. Both were chosen because they are separated from other transitions by several MHz, have a moderate magnetic field dependence of 350 kHz/G and 220 kHz/G and high coupling strength. Furthermore, their coupling strength can be maximized by properly setting the polarization and direction of the laser light with respect to the magnetic field (see chapter 3).



---

## 3. Laser-ion interaction

This chapter summarizes the interactions between an ion trapped in a Paul trap and an incident laser beam. The first two parts review resonant and non-resonant single-qubit interactions. The following sections describe the interactions relevant for a quadrupole transition and a microwave transition. Then the focus shifts to the implementation of a two-qubit operation by making use of a bichromatic light field. This part was also published in [76]. Finally the bichromatic light field will be used to create coherent displacement forces acting on the ion trap harmonic oscillator. Furthermore, the bichromatic light field is used to measure the expectation values of position and momentum for the harmonic oscillator.

### 3.1. Ion laser Hamiltonian

The Hamiltonian describing the trapped ion consists of two parts. The first part describes the ion that can be treated as a two-level system with a laser tuned close to this transition. The second part describes the ion in the external confining potential of the trap that forms a harmonic oscillator. In the following description we assign a pseudo-spin to the qubit. The qubit states can then be identified with  $|\downarrow\rangle$  ( $|\uparrow\rangle$ ) for the lower(upper) energy level. For an ion with mass  $m$  oscillating with frequency  $\omega$  in the harmonic potential the system can be described by the following Hamiltonians

$$H_m = \frac{p^2}{2m} + \frac{1}{2}m\omega^2x^2 \quad (3.1)$$

$$H_e = \frac{1}{2}\hbar\nu\sigma_z \quad (3.2)$$

$$H_l = \hbar\Omega(\sigma^+ + \sigma^-)(e^{i(kx - \nu_l t + \phi)} + e^{-i(kx - \nu_l t + \phi)}) \quad (3.3)$$

where  $\sigma_z, \sigma^+ = \frac{1}{2}(\sigma_x + i\sigma_y), \sigma^- = \frac{1}{2}(\sigma_x - i\sigma_y)$  are Pauli spin operators and  $\nu$  denotes the frequency splitting of the qubit levels. Furthermore,  $\Omega$  includes all details about the exact form of the atom light interaction and is called the *Rabi frequency*, while  $k$  is the wave vector,  $\nu_l$  the laser frequency and  $\phi$  the phase of the light field.  $H_m$  describes the motion of the ion in the harmonic potential, while  $H_e$  describes the ions internal state. The laser-ion interaction is contained in the Hamiltonian  $H_l$ . Using the creation and annihilation operators  $a^\dagger, a$  the Hamiltonians  $H_m$  and  $H_l$  can be reexpressed as

$$H_0 = H_m + H_e = \hbar\omega(a^\dagger a + \frac{1}{2}) + \frac{1}{2}\hbar\nu\sigma_z \quad (3.4)$$

$$H_l = \hbar\Omega(\sigma^+ + \sigma^-)(e^{i\eta(a+a^\dagger)}e^{-i(\nu_l t - \phi)} + e^{-i\eta(a+a^\dagger)}e^{i(\nu_l t - \phi)}) \quad (3.5)$$

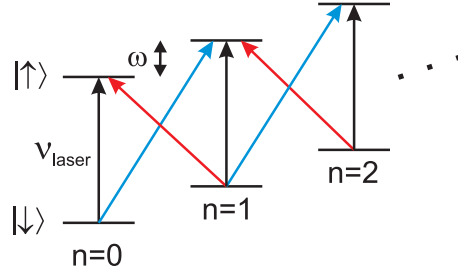


**Figure 3.1.:** Combined energy levels of a two-level system and a harmonic oscillator. The black arrows indicate carrier transitions whereas the red/blue arrows indicate the respective sideband transitions.

Here the *Lamb Dicke* parameter  $\eta$  is used, which is defined as

$$\eta = \vec{k} \vec{e}_z \sqrt{\frac{\hbar}{2m\omega}} \quad (3.6)$$

where  $\vec{e}_z$  denotes the oscillation axis. The *Lamb Dicke* parameter relates the spatial extension of the harmonic oscillator ground state to the wavelength of the atomic transition. It describes the ability of the light field to couple to the motion of the ion in the harmonic oscillator.

Transforming  $H = H_0 + H_l$  into the interaction picture with  $H_{int} = U^\dagger H U$ ,  $U = e^{iH_0 t/\hbar}$  and using the rotating wave approximation leads to the Hamiltonian

$$H_{int}(t) = \hbar\Omega(\sigma^+ e^{i\eta(ae^{-i\omega t} + a^\dagger e^{i\omega t})} e^{-i((\nu_l - \nu)t - \phi)} + h.c.). \quad (3.7)$$

Depending on the detuning  $\Delta = \nu_l - \nu$  of the laser from the transition frequency  $\nu$ , it will couple certain electronic and motional states. If the detuning is exactly  $\Delta = s \omega$  it will couple the state  $|\downarrow, n\rangle$  to  $|\uparrow, n + s\rangle$ , where  $n$  is the vibrational quantum number and  $s \in \mathbb{N}_0$ . Equation (3.7) contains all details about the laser ion interaction.

### 3.1.1. Lamb Dicke regime

An ion is said to be in the Lamb Dicke regime if the extension of its wavefunction is small compared to the wavelength of the light. In this regime, the inequality  $\eta^2 x_{rms} \ll 1$  is fulfilled with  $x_{rms}$  the extent of the vibrational mode's wave function. Then equation (3.7) can be simplified by a Taylor expansion of

$$e^{i\eta(ae^{-i\omega t} + a^\dagger e^{i\omega t})} = 1 + i\eta(ae^{-i\omega t} + a^\dagger e^{i\omega t}) + O(\eta^2). \quad (3.8)$$

Only first order terms need to be considered, that is transitions which change the vibrational quantum number by no more than  $\pm 1$ . The interaction Hamiltonian is now given by

$$H_{int}(t) = \hbar\Omega\sigma^+(1 + i\eta(ae^{-i\omega t} + a^\dagger e^{i\omega t}))e^{-i((\nu_l - \nu)t - \phi)} + h.c.. \quad (3.9)$$

This Hamiltonian gives rise to three different resonances:

- For  $\nu_l = \nu$  only the electronic state of the ion is altered while  $\Delta n = 0$ . The transition  $(|\downarrow, n\rangle \rightarrow |\uparrow, n\rangle)$  is called *carrier transition* where the coupling strength, including a second

## 3.2 Non-resonant interactions

---

order term, scales as  $\Omega_{n,n} = (1 - \eta^2 n)\Omega$ . The small correction  $\approx n$  is obtained going beyond the approximation (3.9). The effective Hamiltonian is given by

$$H_{car}(t) = \hbar\Omega_{n,n}(\sigma^+ e^{i\phi} + \sigma^- e^{-i\phi}). \quad (3.10)$$

Depending on the angle  $\phi$  one can implement  $\sigma_x, \sigma_y$  interactions realizing two of the three single qubit operations described in chapter 2.1.2.

- For  $\nu_l = \nu - \omega_z$  the electronic state of the ion is changed and  $n$  decreases by one. The laser couples the states  $|\downarrow, n\rangle \rightarrow |\uparrow, n-1\rangle$ . The coupling strength for this *red sideband* transition scales as  $\Omega_{n-1,n} = \eta\sqrt{n}\Omega$ . The Hamiltonian is given by

$$H_{red}(t) = i\hbar\Omega_{n-1,n}(a\sigma^+ e^{i\phi} - a^\dagger\sigma^- e^{-i\phi}). \quad (3.11)$$

- Similar for  $\nu_l = \nu + \omega_z$  the electronic state of the ion is changed and  $n$  increases by one. The laser couples  $|\downarrow, n\rangle \rightarrow |\uparrow, n+1\rangle$ . The coupling strength for this *blue sideband* transition scales as  $\Omega_{n+1,n} = \eta\sqrt{n+1}\Omega$ . The Hamiltonian is given by

$$H_{blue}(t) = i\hbar\Omega_{n+1,n}(a^\dagger\sigma^+ e^{i\phi} - a\sigma^- e^{-i\phi}). \quad (3.12)$$

A graphical illustration of carrier and sideband transitions is shown in figure 3.1. It shows the combined energy levels of a two-level system and a harmonic oscillator.

With the help of sideband transitions one can convert the internal excitation of one ion into a collective motion of the whole ion string. For example the state  $|\uparrow\downarrow \dots \downarrow, 0\rangle$ , carrying one electronic excitation, will be transformed into the state  $|\downarrow\downarrow \dots \downarrow, 1\rangle$ , carrying one phonon, by a  $\pi$ -pulse on the red sideband. This excitation can be transferred onto any other ion in the string by another red sideband pulse. In this way two or more ions can interact with another. The motion acts as a kind of bus system mediating the interaction.

## 3.2. Non-resonant interactions

So far we have only considered resonant interactions. However, also non-resonant interactions play a crucial role in the ion-light interaction. On one hand, they can be used to create desired interactions, on the other hand they cause unwanted effects. Non-resonant interactions become especially important when driving sideband transitions. Due to the small coupling of the sidebands to the laser a lot of light is needed. This causes a frequency shift on the atomic levels due to the carrier and population transfer on the carrier.

### 3.2.1. Light shifts

A light field which is off-resonant from a transition will shift the atomic levels. This effect is known as AC-Stark-effect. Consider a two-level atom with an unperturbed energy difference  $E = \hbar\nu$  and a detuning of the light field by  $\delta = \nu - \nu_l$  from this transition. The amplitude of the light field is given by a Rabi frequency  $\Omega$ . The level shift is calculated by going along the same line of

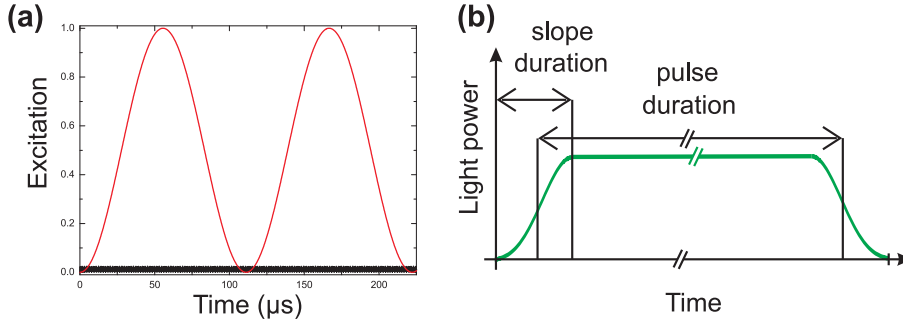


**Figure 3.2.:** (a) Rabi oscillations on the sideband (red) with a Rabi frequency  $\Omega = 2\pi \cdot 45$  kHz. The black line with an amplitude of 0.025 are Rabi oscillations with a frequency of 1.2 MHz taking place on the carrier transition. The oscillation frequency and amplitude is given by equation (3.15). (b) Pulse form of a shaped pulse. The slopes are shaped as a Blackman window, the figure shows the definitions of pulse and slope duration.

reasoning as done for equation (3.7) and calculating the new eigenenergies of the system from the Hamiltonian

$$H_{stark} = \frac{\hbar\delta}{2}\sigma_z + \hbar\Omega\sigma_x. \quad (3.13)$$

Here only carrier transitions were taken into account. For  $\delta \gg \Omega$  one finds that the upper level will be shifted by  $\Omega^2/\delta$  and the lower level will be shifted by  $-\Omega^2/\delta$ . This amounts to a total frequency shift of the transition by

$$\delta_{stark} = 2\frac{\Omega^2}{\delta}. \quad (3.14)$$

From the Hamiltonian one can already see that such an interaction is proportional to a  $\sigma_z$  rotation on a qubit. Thus by shining in a detuned light field for a certain amount of time one can perform an arbitrary rotation around the z-axes realizing the third single qubit operation mentioned in chapter 2.1.2.

So far it seems that Stark shifts are only desired interactions. This changes when one considers exciting sideband transitions like  $|\downarrow, 0\rangle \rightarrow |\uparrow, 1\rangle$  which are needed for some two-qubit gate implementations [14]. These gate-operations are similar to interference experiments, thus it is of utmost importance that the phase relation between pulses does not vary over time. Due to the AC-Stark shift generated by the carrier, intensity fluctuations would be immediately transferred into phase fluctuations and thus spoil the quality of the gate operation. A possibility to get rid of these amplitude-dependent Stark shifts is to shine in a second light field detuned in opposite direction with a Rabi frequency exactly canceling the effect. This light field is derived from the same beam as the driving field and thus has the same amplitude fluctuations which together leads to a common-mode rejection of the Stark shift. A thorough explanation and analysis of this technique can be found in [93, 103].

### 3.2.2. Off resonant excitation

A light field resonant with the transition  $|\downarrow, 0\rangle \rightarrow |\uparrow, 1\rangle$  will not only drive Rabi oscillations on this transition but also off-resonantly drive the carrier transition  $|\downarrow, 0\rangle \rightarrow |\uparrow, 0\rangle$ . This effect can be understood by looking at the time evolution of the  $|D, 0\rangle$  population, which is obtained by solving

### 3.3 The $S_{1/2} \rightarrow D_{5/2}$ transition

---

the optical Bloch equations [104]

$$P_{|\uparrow,0\rangle} = \frac{(2\Omega)^2}{(2\Omega)^2 + \Delta^2} \sin^2 \left( \frac{1}{2} \sqrt{(2\Omega)^2 + \Delta^2} t \right). \quad (3.15)$$

Typical experimental parameters are  $\Omega = 2\pi \cdot 45$  kHz and an axial trap frequency and thus detuning of  $\Delta = \omega_{ax} = 2\pi \cdot 1.2$  MHz. This will result in off-resonant oscillations with an amplitude of 2.5% and a frequency of 1.2 MHz. Rabi oscillation on the carrier and the sideband are shown in figure 3.2(a). As gate operations have to reach fidelities exceeding 99% one has to find a method to avoid this effect.

The method of choice is to switch pulses adiabatically as shown in figure 3.2(b). This pulse shaping has two effects. First, it suppresses high frequency components in the Fourier transform of the pulse which are related to the off-resonant excitations. Second, due to the adiabatic switching which starts and stops with a zero amplitude of the pulse, the off-resonant excitations are adiabatically transformed to zero. Typical pulse slopes are 5 to 10  $\mu$ s for a light power equivalent to performing a full rabi oscillation within 100  $\mu$ s on the blue sideband. Further information on pulse shaping and off-resonant excitations can be found in [105].

### 3.3. The $S_{1/2} \rightarrow D_{5/2}$ transition

For all but one experiment in this thesis the dipole forbidden transition  $S_{1/2} \rightarrow D_{5/2}$  of  $^{40}\text{Ca}^+$  and  $^{43}\text{Ca}^+$  was used to realize a qubit. In this section the excitation of the quadrupole transition  $S_{1/2} \leftrightarrow D_{5/2}$  by laser light is discussed which is important to understand the experiments presented in chapters 6, 7 and 8.

#### 3.3.1. Rabi frequency and geometrical considerations

For a quadrupole transition, the induced electric quadrupole moment  $Q$  couples to the gradient of the applied electric field  $E$ . The Hamiltonian describing this interaction is given by

$$H_I = -Q \cdot \nabla E(t). \quad (3.16)$$

This type of interaction takes on the shape of equation (3.3) when the Rabi frequency is defined as

$$\Omega = \left| \frac{eE_0}{4\hbar} \langle S_{1/2}, F, m_F | (\vec{\epsilon} \cdot \vec{r})(\vec{k} \cdot \vec{r}) | D_{5/2}, F', m'_F \rangle \right| \quad (3.17)$$

with  $E_0$  the electric field amplitude and  $\vec{r}$  the position operator of the valence electron relative to the atomic nucleus. For  $^{40}\text{Ca}^+$  the quantum numbers  $F, F'$  can be ignored and  $m_F, m'_F$  be replaced by  $m_j, m'_j$ . The selection rules allow for  $\Delta m = m_j - m'_j = 0, \pm 1, \pm 2$ . In the case of  $^{43}\text{Ca}^+$ , the same rules apply for  $m_F, m'_F$  but additionally  $\Delta F = F - F' = 0, \pm 1, \pm 2$  has to be fulfilled. From the term  $(\vec{\epsilon} \cdot \vec{r})(\vec{k} \cdot \vec{r})$  one can already guess that the effective coupling strength depends on the laser beam direction and polarization relative to the quantization axis defined by

the magnetic field vector. The expression for the Rabi frequency can be rewritten in the form [94]

$$\Omega = \frac{eE_0}{4\hbar} \sqrt{\frac{15}{c\alpha} \frac{\Gamma_{D_{5/2}}}{k^3}} \Lambda(F, m, F', m') g^{\Delta m}(\phi, \gamma) \quad (3.18)$$

with the fine structure constant  $\alpha$ , the speed of light  $c$ , the electron charge  $e$  and the spontaneous decay rate  $\Gamma_{D_{5/2}}$ . The coupling strength  $\Lambda(F, m, F', m')$  contains all properties of the atomic transition apart from geometrical factors. The coefficients for all transitions in  $^{40}\text{Ca}^+$  and  $^{43}\text{Ca}^+$  are listed in Appendix C.

The function  $g^{\Delta m}(\phi, \gamma)$  contains the geometry dependence of  $\Omega$  [92, 98] where  $\phi$  denotes the angle between the laser beam and the magnetic field and  $\gamma$  describes the angle between a linear polarization and the magnetic field vector projected onto the plane of incidence. Choosing  $\vec{B} = B_0(0, 0, 1)$ , one obtains for  $\vec{k} = k(\sin \phi, 0, \cos \phi)^1$  and  $\vec{\epsilon} = (\cos \gamma \cos \phi, \sin \gamma, -\cos \gamma \sin \phi)$

$$g^{(0)} = \frac{1}{2} |\cos \gamma \sin(2\phi)| \quad (3.19)$$

$$g^{(\pm 1)} = \frac{1}{\sqrt{6}} |\cos \gamma \cos(2\phi) + i \sin \gamma \cos \phi| \quad (3.20)$$

$$g^{(\pm 2)} = \frac{1}{\sqrt{6}} \left| \frac{1}{2} \cos \gamma \sin(2\phi) + i \sin \gamma \sin \phi \right| \quad (3.21)$$

These terms change for circularly polarized light with  $\vec{\epsilon} = \frac{1}{\sqrt{2}}(p \cdot i \cos \phi, 1, -p \cdot i \sin \phi)$  and  $p = \pm 1$  for  $\sigma^\pm$  polarized light to

$$g^{(0)} = \frac{1}{\sqrt{8}} |\sin(2\phi)| \quad (3.22)$$

$$g^{(\pm 1)} = \frac{1}{\sqrt{12}} |\cos(\phi) - \Delta m \cdot p \cdot \cos(2\phi)| \quad (3.23)$$

$$g^{(\pm 2)} = \frac{1}{\sqrt{12}} \left| \frac{1}{2} \sin(2\phi) + \sin \phi \right| \quad (3.24)$$

Since any Zeeman transition from  $S_{1/2} \rightarrow D_{5/2}$  can be used for coherent manipulation of the ions' quantum state, it is interesting to look at the possibility to change the coupling strengths of these transitions. Three cases are especially useful when it comes to maximizing the coupling strength of a particular transition and minimize others:

- **Linear polarized light with  $\phi = 90^\circ$ ,  $\gamma = 90^\circ$ .** Exciting only  $\Delta m = +2$  and  $\Delta m = -2$  transitions. This configuration could be used for sideband cooling (see chapter 5).
- **Linear polarized light with  $\phi = 45^\circ$ ,  $\gamma = 0^\circ$ .** Here the  $\Delta m = 0$  transitions couple strongest to the laser while  $\Delta m = \pm 1$  are completely suppressed. In this configuration one would use e.g. the  $^{40}\text{Ca}^+$   $S_{1/2}(m = +1/2) \rightarrow D_{5/2}(m = +1/2)$  transition for storing the qubit while doing the sideband cooling on  $S_{1/2}(m = +1/2) \rightarrow D_{5/2}(m = +5/2)$ .
- **Circular polarized light along the magnetic field axis  $\phi = 0^\circ$ .** This is the only configuration where a single transition can be selected by using  $\sigma_\pm$  polarized light to excite  $\Delta m = \pm 1$  transitions. This also results in the biggest coupling strength that can be achieved.

<sup>1</sup>the y-component can be chosen to be zero due to cylindrical symmetry

### 3.4 Microwave transitions

---

A disadvantage of this configuration is that sideband cooling is not possible as the cooling cycle can only be closed via the  $P_{3/2}(m_j = +3/2)$  state when the  $S_{1/2}(m_j = +1/2) \rightarrow D_{5/2}(m_j = +5/2)$  transition is excited.

Configuration 3 is especially interesting in  $^{43}\text{Ca}^+$  to reduce the number of possible transitions by a considerable amount. Thereby one can also suppress unwanted off-resonant excitation and Stark shifts due to other carrier transitions close by. A more mathematical treatment of this subject with equations that are valid for arbitrary polarization and angle can be found in [92].

### 3.4. Microwave transitions

For the hyperfine ground state manifold of  $^{43}\text{Ca}^+$  microwave transitions are of importance to manipulate the qubit. A microwave field couples to the magnetic dipole moment of the ion. The Rabi frequency can be expressed as

$$\Omega_{MW} = \left| \frac{1}{2\hbar} \langle S_{1/2}, F = 4, m_F | \vec{\mu}_B \vec{B}_{MW} | S_{1/2}, F' = 3, m'_F \rangle \right| \quad (3.25)$$

with  $\vec{\mu}_B$  the ion's magnetic dipole moment and  $\vec{B}_{MW}$  the magnetic field of the microwave radiation. Similar to dipole transitions one can drive a  $\Delta m_F = 0$  transition with a  $\pi$ -polarized AC magnetic field, whereas for  $\Delta m_F = \pm 1$  transitions  $\sigma_{\pm}$ -polarized fields are needed.

With microwave fields it is impossible to directly drive sideband transitions as the Lamb-Dicke parameter is extremely small. For trapping frequencies of 1 MHz and the ground state hyperfine splitting in  $^{43}\text{Ca}^+$  of 3.2 GHz the Lamb-Dicke parameter is on the order of  $10^{-6}$ . Another drawback is that microwave fields can not be used to address single ions. The wavelength is so big that no focussing can be achieved with respect to the few  $\mu\text{m}$  distance of the ions. Both problems might be circumvented by either using high magnetic field gradients [106] and/or oscillating magnetic fields [107]. These approaches are quite challenging and were not pursued in this thesis.

Although microwave transitions have drawbacks they are a valuable tool for reliably driving the hyperfine qubit, especially if all ions in the trap are subject to the same operation. In this thesis the microwave field was used to map between the hyperfine and the optical qubit (see chapter 6) and to characterize the coherence properties of the hyperfine qubit.

### 3.5. Mølmer-Sørensen gate

A two-qubit quantum gate-operation that is equivalent to a controlled-NOT gate up to local operations is achieved by the action of a Hamiltonian  $H \propto \sigma_n \otimes \sigma_n$ , where  $\sigma_n = \sigma \cdot \mathbf{n}$  is a projection of the vector of Pauli spin matrices onto the direction  $\mathbf{n}$  [108]. Two prominent examples of this type of gate are the conditional phase gate [109, 110] and the Mølmer-Sørensen gate [34, 80, 111] (MS-gate). In the latter case, correlated spin flips between the states  $|\uparrow\rangle|\uparrow\rangle \leftrightarrow |\downarrow\rangle|\downarrow\rangle$  and  $|\uparrow\rangle|\downarrow\rangle \leftrightarrow |\downarrow\rangle|\uparrow\rangle$  are induced by a Hamiltonian

$$H \propto \sigma_\phi \otimes \sigma_\phi \quad \text{where} \quad \sigma_\phi = \cos \phi \sigma_x + \sin \phi \sigma_y. \quad (3.26)$$

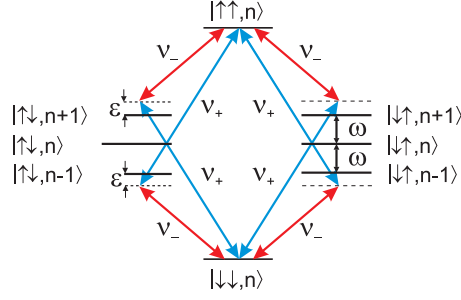


**Figure 3.3.:** Mølmer-Sørensen interaction scheme. A bichromatic laser field couples the qubit states  $|\downarrow\downarrow\rangle \leftrightarrow |\uparrow\uparrow\rangle$  via the four interfering paths shown in the figure. Similar processes couple the states  $|\uparrow\downarrow\rangle \leftrightarrow |\downarrow\uparrow\rangle$ . The frequencies  $\nu_{\pm}$  of the laser field are tuned close to the red and the blue motional sidebands of the qubit transition with frequency  $\nu_0$ , and satisfy the resonance condition  $2\nu_0 = \nu_+ + \nu_-$ . The vibrational quantum number is denoted  $n$ .

The unitary operation  $U_{\phi}^{MS} = \exp(i\frac{\pi}{4}\sigma_{\phi} \otimes \sigma_{\phi})$  maps product states onto maximally entangled states. In 1999 the proposal was made to realize an effective Hamiltonian [80, 111] taking the form (3.26) by exciting both ions simultaneously with a bichromatic laser beam with frequencies  $\nu_{\pm} = \nu_0 \pm \delta$  where  $\nu_0$  is the qubit transition frequency and  $\delta$  is close to a vibrational mode of the two-ion crystal with frequency  $\omega$ . Figure 3.3 shows the level scheme of two ions in a harmonic oscillator and the laser fields applied for a Mølmer-Sørensen interaction. Changing into an interaction picture and performing a rotating-wave approximation, the time-dependent Hamiltonian

$$H(t) = \hbar\Omega(e^{-i\delta t} + e^{i\delta t})e^{i\eta(ae^{-i\omega t} + a^{\dagger}e^{i\omega t})}(\sigma_{+}^{(1)} + \sigma_{+}^{(2)}) + \text{h.c.} \quad (3.27)$$

is well approximated by

$$H(t) = -\hbar\eta\Omega(a^{\dagger}e^{i(\omega-\delta)t} + ae^{-i(\omega-\delta)t})S_y \quad (3.28)$$

in the Lamb-Dicke regime.

In equation (3.28), we use a collective spin operator  $S_y = \sigma_y^{(1)} + \sigma_y^{(2)}$ . In the following we denote the laser detuning from the motional sidebands by  $\omega - \delta = \epsilon$ . The whole subsequent treatment of the MS-interaction can be generalized for  $N$  ions by exchanging  $S_y$  with  $S_y^N = \sum_{i=0}^N \sigma_y^{(i)}$ . The Hamiltonian (3.28) can be exactly integrated [81] yielding the propagator

$$U(t) = \hat{D}(\alpha(t)S_y)e^{(i\lambda t - \chi \sin(\epsilon t))S_y^2}, \quad (3.29)$$

where  $\alpha(t) = \frac{\eta\Omega}{\epsilon}(e^{i\epsilon t} - 1)$ ,  $\lambda = \eta^2\Omega^2/\epsilon$ ,  $\chi = \eta^2\Omega^2/\epsilon^2$ , and  $\hat{D}(\alpha) = e^{\alpha a^{\dagger} - \alpha^* a}$  is a displacement operator. For a gate time  $t_{\text{gate}} = 2\pi/|\epsilon|$ , the displacement operator vanishes so that the propagator  $U(t_{\text{gate}}) = \exp(i\lambda t_{\text{gate}}S_y^2)$  can be regarded as being the action of an effective Hamiltonian

$$H_{\text{eff}} = -\hbar\lambda S_y^2 = -2\hbar\lambda(\mathbf{1} + \sigma_y \otimes \sigma_y) \quad (3.30)$$

inducing the same action up to a global phase as the one given in (3.26). Setting  $\Omega = |\epsilon|/(4\eta)$ , a gate is realized, which is capable of maximally entangling ions irrespective of their motional state.

In the description of the gate mechanism given so far, a coupling of the light field to the carrier transition was neglected based on the assumption that the Rabi frequency  $\Omega$  was small compared

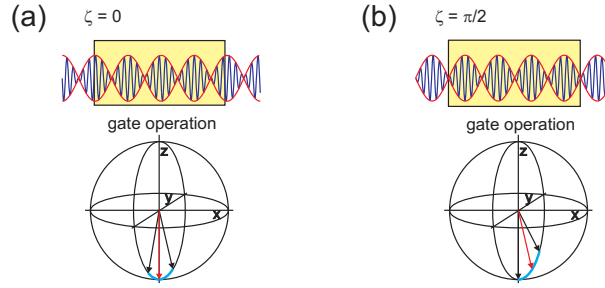


**Figure 3.4.:** Effect of non-resonant excitation of the carrier transition. (a) For  $\zeta = 0$ , the gate starts at a maximum of the intensity-modulated beam. In this case, a Bloch vector initially centered at the south pole of the Bloch sphere performs oscillations that are symmetric around the initial position. (b) For  $\zeta = \pi/2$ , the gate starts at the minimum of the intensity modulation. In this case, the average orientation of the Bloch vector is tilted with respect to its initial position.

to the detuning  $\delta$  of the laser frequency components from the transition. In this case, small non-resonant Rabi oscillations that appear on top of the gate dynamics are the main effect of coupling to the carrier transition. Since a maximally entangling gate requires a Rabi frequency  $\Omega \propto \eta^{-1} t_{\text{gate}}^{-1}$ , the question of whether  $\Omega \ll \delta$  holds becomes crucial in the limit of fast gate operations and small Lamb-Dicke factors. Our experiments [40] are exactly operating in this regime, and it turns out that non-resonant excitation of the carrier transition has further effects beyond inducing non-resonant oscillations [112]. This becomes apparent by interpreting terms in the Hamiltonian in a different way: The red- and blue-detuned frequency components  $E_{\pm} = E_0 \cos((\nu_0 \pm \delta)t \pm \zeta)$  of equal intensity may be viewed as a single laser beam  $E(t) = E_+ + E_- = 2E_0 \cos(\nu_0 t) \cos(\delta t + \zeta)$  that is resonant with the qubit transition but amplitude-modulated with frequency  $\delta$ . Here, the phase  $\zeta$  which determines whether the gate operation starts in a maximum ( $\zeta = 0$ ) or a minimum ( $\zeta = \pi/2$ ) of the intensity of the amplitude-modulated beam has a crucial influence on the gate-operation. This can be intuitively understood by considering the initial action the gate exerts on an input state in the Bloch sphere picture shown in figure 3.4. For short times, coupling to the sidebands can be neglected which justifies the use of a single-ion picture. The dynamics is essentially the one of two uncoupled qubits. The fast dynamics of the gate is induced by excitation of the ions on the carrier transition. For  $\zeta = 0$ , the Bloch vector of an ion initially in state  $|\downarrow\rangle$  will oscillate with frequency  $\delta$  along a line centered on the south pole of the Bloch sphere. For  $\zeta = \pi/2$ , the oscillation frequency is the same, however, the time-averaged position of the Bloch vector is tilted by an angle

$$\psi = \frac{4\Omega}{\delta} \sin \zeta \quad (3.31)$$

with respect to the initial state  $|\downarrow\rangle$ . This effect has a profound influence on the gate action. A careful analysis of the gate mechanism [112] taking into account the non-resonant oscillations reveals that the Hamiltonian (3.28) is changed into

$$H(t) = -\hbar\eta\Omega(a^\dagger e^{i(\omega-\delta)t} + a e^{-i(\omega-\delta)t})S_{y,\psi}, \quad (3.32)$$

where

$$S_{y,\psi} = S_y \cos \psi + S_z \sin \psi, \quad (3.33)$$

and that the propagator (3.29) needs to be replaced by

$$U(t) = e^{(-iF(t)S_x)} \hat{D}(\alpha(t)S_{y,\psi}) e(i(\lambda t - \chi \sin(\epsilon t))S_{y,\psi}^2), \quad (3.34)$$

where the term containing  $F(t) = \frac{2\Omega}{\delta}(\sin(\delta t + \zeta) - \sin \zeta)$  describes non-resonant excitation of the carrier transition. In the derivation of Hamiltonian (3.32), small terms arising from the non-commutativity of the operators  $S_y, S_z$  have been neglected [112]. The dependence of the propagator on the exact value of  $\zeta$  is inconvenient from an experimental point of view. To realize the desired gate-operation in an optimal way, precise control over  $\zeta$  is required. In addition, the gate duration must be controlled to better than a fraction of the mode oscillation period because of the non-resonant oscillation. Fortunately, both of these problems can be overcome by shaping the overall intensity of the laser pulse such that the Rabi frequency  $\Omega(t)$  smoothly rises within a few cycles  $2\pi/\delta$  to its maximum value  $\Omega_{\text{gate}} \approx |\epsilon|/(4\eta)$  and smoothly falls off to zero at the end of the gate. In this case, the non-resonant oscillations vanish and (3.31) shows that the operator  $S_{y,\psi}(t)$  adiabatically follows the laser intensity so that it starts and ends as the desired operator  $S_y$  irrespective of the phase  $\zeta$ . For intensity-shaped pulses, the propagator (3.29) provides therefore an adequate description of the gate action.

### 3.5.1. AC-Stark shifts

In the description of the gate mechanism given so far the ion was treated as an ideal two-level system. AC-Stark shifts are completely insignificant provided that the intensities of the blue- and the red-detuned frequency components are the same since in this case light shifts of the carrier transition caused by the blue-detuned part are exactly canceled by light shifts of the red-detuned light field. Similarly, light shifts of the blue-detuned frequency component non-resonantly exciting the upper motional sideband are perfectly canceled by light shifts of the red-detuned frequency component coupling to the lower motional sideband.

For an experimental implementation with calcium ions, we need to consider numerous energy levels (see figure 2.3). Here, the laser field inducing the gate action causes AC-Stark shifts on the qubit transition frequency due to non-resonant excitation of far-detuned dipole transitions and also of other  $S_{1/2} \leftrightarrow D_{5/2}$  Zeeman transitions. The main contributions arise from couplings between the qubit states and the  $4p$ -states that are mediated by the dipole transitions  $S_{1/2} \leftrightarrow P_{1/2}$ ,  $S_{1/2} \leftrightarrow P_{3/2}$ ,  $D_{5/2} \leftrightarrow P_{3/2}$ . Other transitions hardly matter as can be checked by comparing the experimental results obtained in [103] with numerical results based on the transition strengths [98] of the dipole transitions coupling to the  $4p$ -states. For suitably chosen  $k$ -vector and polarization of the bichromatic laser beam, these shifts are considerably smaller than the strength  $\lambda$  of the gate interaction.

AC-Stark shifts can be compensated by a suitable detuning of the gate laser. An alternative strategy consists in introducing an additional AC-Stark shift of opposite sign that is also caused by the gate laser beam [103]. This approach has the advantage of making the AC-Stark compensation independent of the gate laser intensity. In contrast to previous gate-operations relying on this

### 3.5 Mølmer-Sørensen gate

technique [113] where the AC-Stark shift was caused by the quadrupole transition and compensated by coupling to dipole transitions, here, the AC-Stark shift is due to dipole transitions and needs to be compensated by coupling to the quadrupole transition.

For ions prepared in the ground state of motion ( $n = 0$ ), a convenient way of accomplishing this task is to perform the gate operation with slightly imbalanced intensities of the blue- and the red-detuned laser frequency components. Setting the Rabi frequency of the blue-detuned component to  $\Omega_b = \Omega(1 + \xi)$  and the one of the red-detuned to  $\Omega_r = \Omega(1 - \xi)$ , an additional light shift caused by coupling to the carrier transition is induced that amounts to  $\delta_{ac}^{(C)} = 2(\Omega_r^2 - \Omega_b^2)/\delta = -8\Omega^2\xi/\delta$ . Now, the beam imbalance parameter  $\xi$  needs to be set such that the additional light shift exactly cancels the phase shift  $\phi = \delta_{ac}t_{gate}$  induced by the dipole transitions during the action of the gate. Taking into account that  $t_{gate} = 2\pi/\epsilon$  and  $\Omega = |\epsilon|/(4\eta)$ , this requires  $\xi = (\delta\eta^2/|\epsilon|)(\phi/\pi)$ .

Apart from introducing light shifts, setting  $\xi \neq 0$  also slightly changes the gate Hamiltonian (3.30) from  $H_{eff} = -\lambda S_y^2$  to  $H_{eff} = -\lambda(S_y^2 + \xi^2 S_x^2)$  [114] since the coupling between the states  $|\downarrow\downarrow\rangle$ ,  $|\uparrow\uparrow\rangle$  is proportional to  $2\Omega_b\Omega_r = 2\Omega^2(1 - \xi^2)$  whereas the coupling between  $|\downarrow\uparrow\rangle$ ,  $|\uparrow\downarrow\rangle$  is proportional to  $\Omega_b^2 + \Omega_r^2 = 2\Omega^2(1 + \xi^2)$ . However, as long as  $\xi \ll 1$  holds – which is the case in the experiments described in chapter 6 – this effect is extremely small<sup>2</sup> as the additional term is only quadratic in  $\xi$ .

Another side effect of setting  $\xi \neq 0$  is the occurrence of an additional term  $\propto S_z a^\dagger a$  in the Hamiltonian. It is caused by AC-Stark shifts arising from coupling to the upper and lower motional sideband which no longer completely cancel each other. The resulting shift of the qubit transition frequency depends on the vibrational quantum number  $n$  and is given by  $\delta^{(SB)} = (8\eta^2\Omega^2/\epsilon)\xi n = (\epsilon/2)\xi n$ . Simulations of the gate action based on (3.27) including an additional term  $\propto S_z$  accounting for AC-Stark shifts of the dipole transitions and power-imbalanced beams show that the unwanted term  $\propto S_z a^\dagger a$  has no severe effects for ions prepared in the motional ground state as long as  $\xi \ll 1$ . However, for ions in Fock states with  $n > 0$ , this is not the case. Taking the parameter set  $\xi = 0.075$ ,  $\omega = (2\pi) 1230$  kHz, and  $\epsilon = (2\pi) 20$  kHz as an example, the following numerical results are obtained: applying the gate to ions prepared in  $|\downarrow\downarrow\rangle|n = 0\rangle$ , a Bell state is created with fidelity 0.9993. For  $n = 1$ , the fidelity drops to 0.985, and for  $n = 2$  to even 0.942. This loss of fidelity can be only partially recovered by shifting the laser frequency by  $\delta^{(SB)}$ , the resulting fidelity being 0.993 and 0.968, for  $n = 1$  and  $n = 2$  respectively. For higher motional states, the effect is even more severe and shows that this kind of AC-Stark compensation is inappropriate when dealing with ions in a thermal state of motion with  $\bar{n} \gg 1$ . Instead of compensating the AC-Stark shift by imbalancing the beam powers, in this case, the laser frequency needs to be adjusted accordingly (see chapter 6 on the experiments with Doppler-cooled ions).

#### 3.5.2. A Mølmer-Sørensen interaction with ions in a thermal state of motion

In theory, the Mølmer-Sørensen gate does not require the ions to be cooled to the ground states of motion since its propagator (3.29) is independent of the vibrational state for  $t = t_{gate}$ . For

<sup>2</sup>The additional term  $S_x^2$  changes the gate operation from  $U = \exp(-i\frac{\pi}{8}S_y^2)$  to  $U_\xi = \exp(-i\frac{\pi}{8}(S_y^2 + \xi^2 S_x^2))$ . A short calculation shows that the minimum state fidelity  $F_{min} = \min_{\{\psi\}}(|\langle\psi|U^\dagger U_\xi|\psi\rangle|^2)$  is given by  $F_{min} = \frac{1}{2}(1 + \cos(\frac{\pi}{2}\xi^2))$  where we used  $[S_x^2, S_y^2] = 0$  and  $\exp(-i\gamma S_x^2) = 1 + \frac{1}{4}(e^{-i4\gamma} - 1)S_x^2$ . Thus, for  $\xi = 0.075$ , one obtains  $F_{min} \approx 1 - 2 \cdot 10^{-5}$ .

$t \neq t_{\text{gate}}$ , however, the interaction entangles qubit states and vibrational states so that the qubits' final state becomes dependent on the initial vibrational state. Therefore, it is of interest to calculate expectation values of observables acting on the qubit state space after applying the propagator for an arbitrary time  $t$ . Simple expressions can be derived [76] in the case of a thermally occupied motional state where the mode population probabilities are given by

$$\tilde{p}_n = \frac{1}{\bar{n} + 1} \left( \frac{\bar{n}}{\bar{n} + 1} \right)^n. \quad (3.35)$$

Not taking into account non-resonant carrier oscillations, one finds the following expressions for the qubit state populations

$$\begin{aligned} p_{\uparrow\uparrow}(t) &= \frac{1}{8} (3 + e^{-16|\alpha|^2(\bar{n}+\frac{1}{2})} + 4 \cos(4\gamma) e^{-4|\alpha|^2(\bar{n}+\frac{1}{2})}) \\ p_{\uparrow\downarrow}(t) + p_{\downarrow\uparrow}(t) &= \frac{1}{4} (1 - e^{-16|\alpha|^2(\bar{n}+\frac{1}{2})}) \\ p_{\downarrow\downarrow}(t) &= \frac{1}{8} (3 + e^{-16|\alpha|^2(\bar{n}+\frac{1}{2})} - 4 \cos(4\gamma) e^{-4|\alpha|^2(\bar{n}+\frac{1}{2})}) \end{aligned} \quad (3.36)$$

with  $\alpha = \alpha(t)$  and  $\gamma = \lambda t - \chi \sin(\epsilon t)$  containing the time dependent terms.

### 3.6. Creating a coherent displacement

Another application for bichromatic light fields is to create coherent displacement forces. This can be done by shining in two light fields resonant with the blue and red sideband transition. Putting together equations (3.12) and (3.11) and calculating a few lines to simplify the expressions one arrives at the following Hamiltonian

$$\begin{aligned} H_D &= \hbar\eta\Omega [\sigma_x \cos \phi_+ - \sigma_y \sin \phi_+] \\ &\otimes [(a + a^\dagger) \cos \phi_- + i(a^\dagger - a) \sin \phi_-]. \end{aligned} \quad (3.37)$$

Here  $2\phi_+ = \phi_r + \phi_b$  and  $2\phi_- = \phi_b - \phi_r$  are the sum and the difference, respectively, of the phases of the light fields tuned to the red and blue sideband. One can recognize the position  $\hat{x}$  and momentum operators  $\hat{p}$  in the second part of the Hamiltonian. The propagator for  $\phi_- = \phi_+ = 0$  is then

$$U_D = e^{-\frac{i\eta\Omega t}{\Delta} x \sigma_x} \quad (3.38)$$

which describes a state dependent coherent displacement operator  $D(\alpha\sigma_x)$  with  $\alpha = i\eta\Omega t/\Delta$  (see chapter 2). The propagator (3.38) displaces an eigenstate of  $\sigma_x$  along  $p$  in phase space. If the initial state was in the ground state a coherent state is created. By properly choosing the phases  $\phi_-, \phi_+$  one can create coherent states with arbitrary  $\alpha$ .

#### 3.6.1. Measurement of $\langle x \rangle$ and $\langle p \rangle$

A lot of ion trap experiments make extensive use of the harmonic oscillator created by the trap confinement for implementing two-qubit interactions. The ion trap system is always referred to as

### 3.6 Creating a coherent displacement

---

“the“ toy model for a quantum harmonic oscillator. Nevertheless the expectation values for the position and momentum operators  $\langle x \rangle$  and  $\langle p \rangle$  have never been measured with trapped ions up to now. Here a method is presented similar to one proposed in [115–117] to measure these quantities without reconstructing the full quantum state.

As already mentioned in chapter 2.1.3 the only observable that can be directly measured in ion trap experiments by fluorescence detection is  $\sigma_z$ . By using additional laser pulses one can generate a propagator  $U$  that maps other observables onto  $\sigma_z$ . In this case we apply the propagator  $U_D$  to the state  $\rho$  of the ion prior to the state detection which is equivalent to measuring the observable

$$A(t) = U_D^\dagger \sigma_z U_D = \cos(2\eta \hat{x} \Omega_p t / \Delta) \sigma_z + \sin(2\eta \hat{x} \Omega_p t / \Delta) \sigma_y \quad (3.39)$$

on the initial state because of  $\text{Tr}((U^\dagger \rho U) \sigma_z) = \text{Tr}(\rho (U \sigma_z U^\dagger))$ . If the ion’s internal initial state is the eigenstate of  $\sigma_z$  belonging to eigenvalue  $+1$ ,  $\langle A(t) \rangle = \cos(2\eta \hat{x} \Omega_p t / \Delta)$  and for the eigenstate of  $\sigma_y$  belonging to eigenvalue  $+1$ ,  $\langle A(t) \rangle = \sin(2\eta \hat{x} \Omega_p t / \Delta)$ .

Thus preparing  $\rho$  in an eigenstate of  $\sigma_y$  and taking the first derivative of the measured expectation value

$$\left. \frac{d}{dt} \langle A(t) \rangle \right|_{t=0} = 2\eta \Omega_p / \Delta \langle \hat{x} \sigma_y \rangle \quad (3.40)$$

reveals that the slope of the measured excitation at  $t = 0$  is proportional to  $\langle x \rangle$ . By changing the phase  $\phi_-$  from 0 to  $\pi/2$  it is possible to measure  $\langle p \rangle$  instead of  $\langle x \rangle$ . Furthermore all n-momenta of  $x$  can be measured by taking the n-th derivative

$$\left. \frac{d^n}{dt^n} \langle A(t) \rangle \right|_{t=0} \propto \langle \hat{x}^n \sigma_y \rangle. \quad (3.41)$$

We have applied this technique to determine position and momentum in a simulation of a Dirac particle encoded in position and momentum of the harmonic oscillator (see chapter 8).



---

## 4. Experimental setup

In this chapter an experimental setup is described used to realize the experiments discussed in the proceeding chapters. A section about the ion trap and the vacuum setup will be followed by a description of the laser system and the computer control.

### 4.1. Linear ion trap and electrode wiring

The ion trap used in this thesis is the standard Innsbruck design (see figure 4.1(a)). It is a linear Paul trap where the radio frequency (RF) drive is applied to one of two pairs of blades while the other pair is grounded. This creates the radial confinement. An additional DC voltage applied to the tips generates the axial confinement (see figure 4.1(b)). A thorough discussion of the specifications and design of the trap can be found in Jan Benhelm's thesis [94].

The ion trap is operated at a frequency of about 25.5 MHz produced by a signal generator<sup>1</sup> whose output is amplified<sup>2</sup> to 5-13 W. This signal is then coupled into a helical resonator amplifying the voltage to about 1200 V which is applied to the blades. This creates a harmonic potential with trapping frequencies between 2.5 MHz and 4 MHz in the radial directions. The two radial modes are almost degenerate in frequency and measurements showed that they are split by about 50 kHz. The orientation of these modes is along the RF-blades of the trap. This breaking of the radial symmetry is due to the fact that the RF potential is only applied to one blade pair while the other is grounded. The DC voltage applied to the tips ranges between 800-1400 V. A typical voltage of 1200 V creates an axial potential with a trap frequency of 1.36 MHz for a  $^{40}\text{Ca}^+$  ion.

<sup>1</sup>Rohde & Schwarz, SML01

<sup>2</sup>Mini Circuits LZY-1

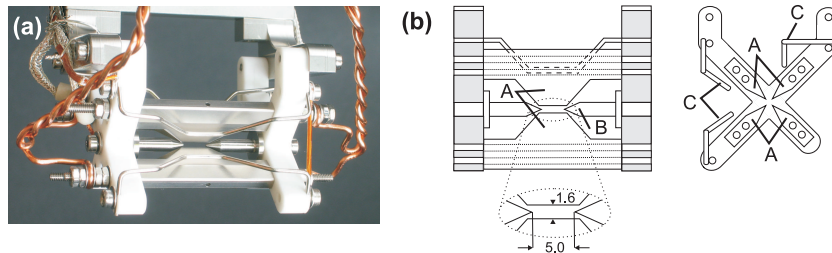


**Figure 4.1.:** (a) Picture of the linear Paul trap used in the experiment. (b) Schematic drawing of the trap. Two opposite blade shaped electrodes (A) are connected to a high voltage radio frequency while the other pair is grounded. The tips (B) are connected to a DC voltage up to 1400 V. The compensation electrodes (C) are used to shift the ions into the RF null compensating stray electric fields. The upper compensation electrode of the pair used for horizontal micromotion compensation is also used to guide microwave signals to the ions. The distance of the tips and electrodes is given in mm.

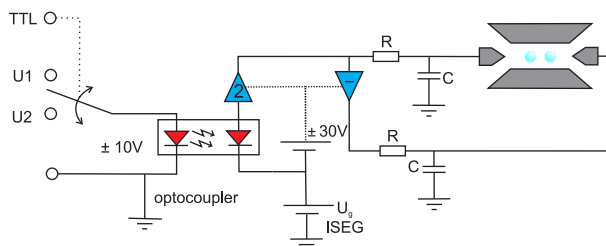


**Figure 4.2.:** Wiring of the DC-trap electrodes. Each tip is wired to a circuit that can change the voltages on the tips by twice the preset voltages  $U_1/U_2$ . A TTL signal switches between the two voltages and the RC combination is designed such that voltage reaches the desired value within  $40 \mu\text{s}$ . This time constant is given by the low pass filters attached to the tips. The virtual ground  $U_g$  for the secondary side is provided by a stable high voltage source (ISEG). The effective voltage on the tips is then given by  $U_{tip1} = U_g \pm U_{1/2}$  and  $U_{tip2} = U_g \mp U_{1/2}$ .

These voltage values lead to a string of ions in the trap along the direction of the tips. The equilibrium positions of the ions are determined by the external trapping potential and the Coulomb repulsion between the ions. For two ions of mass  $m$  the distance can be calculated analytically and is given by

$$\Delta z = \left( \frac{e^2}{2\pi\epsilon_0 m \omega_z} \right)^{1/3}. \quad (4.1)$$

For an axial center of mass frequency  $\omega_z = 1.2 \text{ MHz}$  this leads to an ion spacing of  $4.6 \mu\text{m}$ . This knowledge is used to calibrate the imaging system in combination with the precisely measurable trap frequency.

Each tip is wired separately such that it is possible to put them on different potentials. By changing the potentials applied to the tips the ion string can be moved along the trap axis. To shuttle the ions fast without compromising the stability of the trap potential we designed a circuit which can change the tip voltage by  $\pm 20 \text{ V}$ . With a TTL signal one can switch between two preset values  $U_1, U_2$  such that the voltage on the tips changes within  $40 \mu\text{s}$ . The time constant is given by the low pass filters attached to the tips. On the one hand these filters block noise going to the trap electrodes and on the other hand they shield the electronics from RF pick up by the tips. A schematic drawing of the circuit can be seen in figure 4.2. A stable high voltage<sup>3</sup> source provides the virtual ground ( $U_g = 800 - 1200 \text{ V}$ ) for the secondary side of the analog optocoupler<sup>4</sup>. A power supply referenced to the same high voltage provides the necessary current to drive the adder/multiplier circuit. This design allows one to combine the stability of the high voltage box  $< 10^{-5}$  with a fast switching capability. The instability of the voltages  $U_1, U_2$  ( $\Delta V/V \approx 10^{-3}$ ) and the noise of the electronic circuit ( $\Delta V/V \approx 10^{-3}$ ) do not harm. This comes from the fact, that the noise has to be compared to the 800 to 1200 V provided by the high voltage source. The effective noise is less than  $10^{-5}$  which is sufficient for all experiments in this thesis. The effective voltage on the tips is given by  $U_{tip1} = U_g \pm U_{1/2}$  and  $U_{tip2} = U_g \mp U_{1/2}$ .

Due to electric stray fields, the ion position can be pushed out of the RF null leading to a motion of the ion with a frequency which is the same as the drive frequency. This excess micromotion

<sup>3</sup>ISEG, EHQ F020p, 0-2kV,  $\Delta V/V < 10^{-5}$

<sup>4</sup>HCNR201 Agilent Tech.

## 4.2 Vacuum vessel

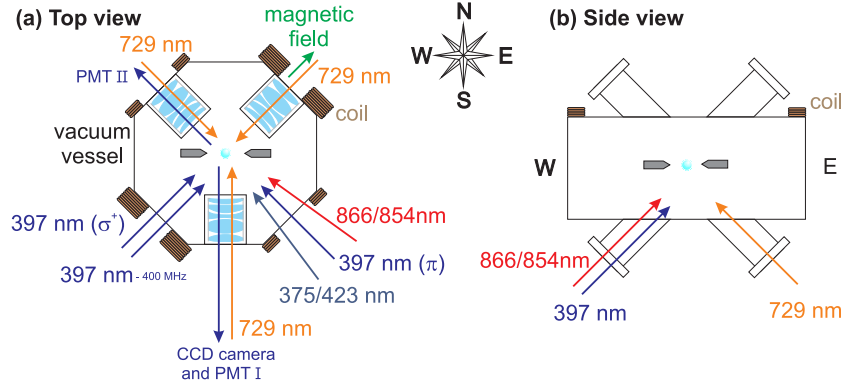


**Figure 4.3.:** (a) Schematic drawing of the trap setup viewed from atop showing trap orientation, laser beam directions and positioning of the inverted viewports. Most of the laser beams entering the chamber are within the equatorial plane. Two coils in almost Helmholtz configuration generate a magnetic field defining the quantization axes along SW-NE. An additional coil pair along SE-NW is used for compensating external magnetic stray fields. The inverted view ports allow us to place custom-made lenses close to the ions. The lenses are used to focus laser beams tightly and at the same time collect a big fraction of the fluorescence light emitted by the ions. (b) Side view of the setup. The viewports at the top and the bottom of the vacuum chamber are mounted under an angle of  $60^\circ$  with respect to the equatorial plane. Additional beams for Doppler cooling and ion state manipulation are guided through these windows. The single coil on top of the vacuum chamber is used to compensate the earth's magnetic field.

can be minimized by compensating for the stray electric fields and shifting the ion back into the potential node. This can be done by applying small voltages to the compensation electrodes, ranging typically from 1 V to 150 V.

## 4.2. Vacuum vessel

The vacuum chamber housing the ion trap is a stainless steel octagon with eight CF63 flanges. Three of the eight flanges are equipped with inverted viewports<sup>5</sup> the rest have regular viewports attached<sup>6</sup>. The inverted viewports allow us to place custom made lenses<sup>7</sup> close to the ions and to steer or replace them without opening the vacuum chamber. The proximity to the ions guarantees a good imaging resolution, a high photon collection efficiency and the ability to tightly focus lasers to address individual ions. The top and the bottom of the chamber consist of two CF200 flanges each carrying two CF40 flanges with windows mounted under an angle of  $60^\circ$  relative to the equatorial plane. Additional CF16 feedthroughs are attached to the bottom and top flange for wiring the ion trap and the calcium oven. A schematic drawing can be seen in figure 4.3a.

Not shown in this drawing are the ion getter pump<sup>8</sup>, the titanium sublimation pump<sup>9</sup> and the Bayard-Alpert-Gauge<sup>10</sup> attached to the chamber via a six way cross. The ion pump runs

<sup>5</sup>Ukaea, fused silica, anti reflection coating (Tafelmaier, 397nm and 720-870nm on vacuum side only)

<sup>6</sup>Ukaea, fused silica, anti reflection coating (Tafelmaier, 397nm and 720-870nm)

<sup>7</sup>Silloptics, Germany

<sup>8</sup>Varian Star Cell, 20 l

<sup>9</sup>Varian

<sup>10</sup>Varian, UHV-24 Gauge

permanently while the titanium sublimation pump is fired once a week. The pressure in the chamber stays below the measurement limit of the Bayard-Alpert gauge of  $2 \cdot 10^{-11}$  mbar.

### 4.3. Magnetic field coils

Two pairs of magnetic field coils are attached to the vacuum chamber (see figure 4.3a). The coil pair aligned along the SW-NE direction is generating the quantization field. The distance of the coils is 300 mm while their inner diameter is 115 mm. This mounting does not quite resemble a Helmholtz configuration but nevertheless we expect only small magnetic field gradients at the ion position. Measurements with two entangled ions confirmed that the gradient at the trap center is smaller than 0.2 G/m. This means that the frequency change, due to this gradient, is smaller than 1 Hz on the qubit transition for two ions separated by 4  $\mu\text{m}$ . The coils are made out of 300 windings of copper wire. A current of 1 A sent through these coils produces a magnetic field of 3.4 G at the ion position. The second pair aligned along the SE-NW<sup>11</sup> direction is for compensating external magnetic fields in order to align the quantization axis with the SW-NE direction. An additional single coil with a 200 mm diameter (see figure 4.3b) is mounted on the top flange to compensate for magnetic fields in the vertical direction.

All coils are powered by home-built current drivers having a relative current drift of less than  $2 \cdot 10^{-5}$  in 24 h. This is achieved by actively stabilizing the current by a servo loop. A stable reference voltage is compared with the voltage drop across a highly stable resistor<sup>12</sup> and used as a feedback signal.

### 4.4. Optical access and single ion addressing

Several laser beams enter the vacuum chamber from seven different directions (see figure 4.3). A 397 nm  $\sigma^+$ -polarized beam is aligned exactly with the magnetic field direction. It is used for optical pumping of  $^{40}\text{Ca}^+$  and  $^{43}\text{Ca}^+$  and as an additional Doppler cooling beam for  $^{43}\text{Ca}^+$ . All laser beams for Doppler cooling, repumping and photoionization are sent through the SE port of the chamber. The beams are focused by adjusting the output coupler of the fibers. Typical beam waists are on the order of 100-200  $\mu\text{m}$ . Additional beams for Doppler cooling and repumping are sent in via the viewports in the bottom of the vessel. These beams are used when a second photomultiplier tube (PMT)<sup>13</sup> at the NW port is added to the primary PMT located at the south viewport. The only beam that remains operational from the SE corner is the photoionization beam. In order not to damage the second PMT during loading the light is automatically blocked by a shutter in front of the PMT whenever the photoionization lasers are on.

Four 729 nm beams for manipulating the qubits are sent onto the ions. The one entering from the inverted viewport S is used for addressing a single ion out of a chain of ions. This is achieved by a custom-made lens system<sup>14</sup> and additional telescope lenses to widen the beam prior to the focussing (see figure 4.4(a)). With this setup the expected diffraction limited spot size is 2.9  $\mu\text{m}$ .

<sup>11</sup>all directions are given according to the compass card in figure 4.3

<sup>12</sup>Vishay, VCS 302

<sup>13</sup>Electron tubes, P25C, Quantum efficiency = 28% at 400 nm

<sup>14</sup>Sill Optics, Germany, antireflection coated for 397 nm and 729 nm

## 4.5 Fluorescence detection

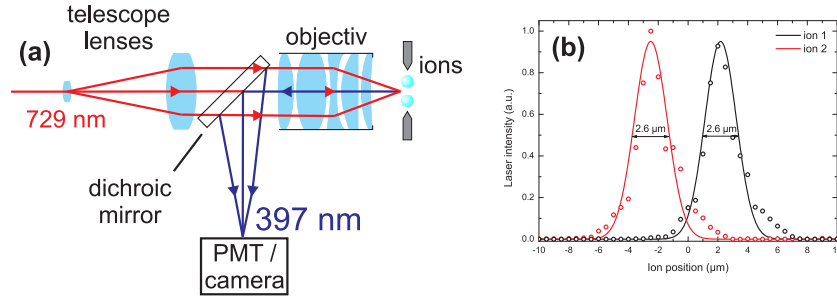


**Figure 4.4.:** (a) Custom-made lens setup for focusing a 729 nm laser down to  $< 4 \mu\text{m}$  for addressing a single ion. The same lens system together with a dichroic mirror is used to image the ion string onto the PMT and the camera. The objective covers about 2.5 % of the full solid angle. A dichroic mirror is used to separate the incoming light at 729 nm from the fluorescence light at 397 nm. (b) Measurement of the intensity profile of the laser beam at 729 nm entering from the south port of the vacuum chamber. For this measurement two ions were first shifted in position with respect to the laser beam and then excited by a laser pulse. The pulse length was chosen such that the ion undergoes  $3\pi$  Rabi flops when the beam is centered on it. The intensity of the beam was then calculated with the recorded excitation.

Two ions were used to probe the experimentally achieved width of the beam by moving them along the trap axis and exciting them with a laser beam (see figure 4.4(b)). The pulse length and intensity of the laser pulse were chosen such that the ion undergoes a  $3\pi$  rotation when the beam is centered on it. The spatial intensity profile of the beam was then deduced from the recorded excitation to the D state. This measurement revealed a FWHM of the beam of  $2.6 \mu\text{m}$ .

Two beams coming from the directions NE and NW are focused to about  $20 \mu\text{m}$ . The NE beam is  $\sigma^+$  polarized for driving the  $S_{1/2}, m_F = 1/2$  to  $D_{5/2}, m_F = 3/2$  transition with maximal efficiency. The NW beam is linearly polarized for driving  $\Delta m = \pm 2$  transitions with maximal efficiency. The beam size is a compromise between maximum intensity and the requirement to illuminate up to three ions equally. Furthermore, the ions should not reside at a position where the intensity profile has a step gradient to minimize coupling strength fluctuations due to beam steering effects. The two beams are not operated simultaneously. In the experiment we can switch from one to the other by exchanging the fiber after the switching AOM (see figure 4.7 AO3). Another 729 nm beam enters the vacuum chamber from a viewport in the bottom of the chamber under an angle of  $60^\circ$  with respect to the equatorial plane. This beam is only focused with the output coupler of the fiber to about  $150 \mu\text{m}$ . It is used to illuminate all trapped ions equally.

## 4.5. Fluorescence detection

To collect the fluorescence light at 397 nm we again utilize the custom made lens design used for focusing the beams at 729 nm (see figure 4.4(a)). It is a five-lens objective which is antireflection coated for 397 nm and 729 nm. The aberrations introduced by the fused silica window of the inverted viewport are corrected by the lens-design. The entrance diameter of the objective is  $d=38 \text{ mm}$  and the distance to the ions from the first lens is  $r=58 \text{ mm}$ . The photon collection

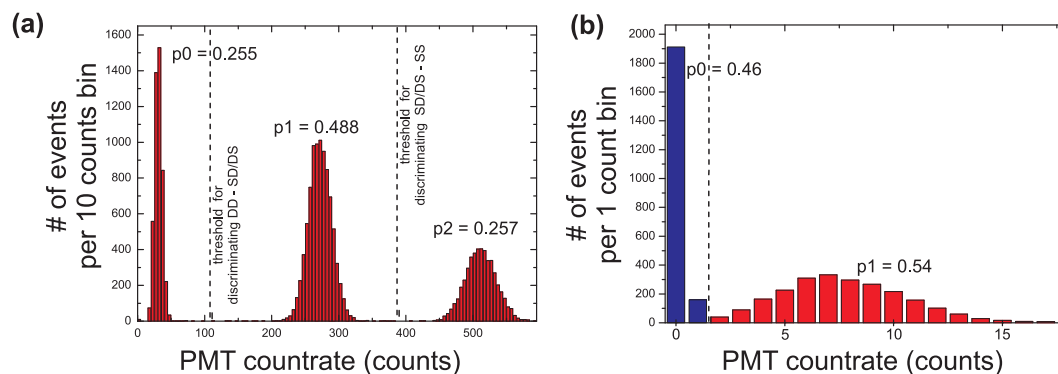


**Figure 4.5.:** (a) Fluorescence histogram for two ions each in a superposition of S and D. In this plot laser intensity and detection time (3 ms) were chosen such that a detection fidelity exceeding 99.9% was achieved. Two thresholds are used to discriminate between three different two ion states. Either both ions are in the D state, both are in the S state or one is in the D state and the other in the S state with a respective mean photon count rate of 30, 270, 510 photons in 3 ms. The probabilities of finding  $k$  bright ions are denoted  $p_k$ . (b) The histogram illustrates the discrimination of the two-qubit states  $S_{1/2}$  and  $D_{5/2}$  for a single ion using two PMTs. For each data point the fluorescence of the ion, prepared in a superposition of the S and D state, was measured for 250  $\mu s$ . On average we acquire 0.07 photons during this detection time for the ion in the D state. If the ion is in the S state 7.8 photons are detected. By introducing a threshold between one and two detected photons one can discriminate between the two states. The intensity of the detection laser was chosen such that the ion was not heated beyond the mean phonon number achieved with Doppler cooling. Additionally the time of the detection was made as short as possible to shorten the duration of the sequence. Despite these restrictions a detection infidelity of wrongly assigning a quantum state of 0.32 % was achieved. For an application of this detection technique see chapter 7.

efficiency is given by the solid angle of the objective which is

$$\frac{d\Omega}{4\pi} = \frac{1}{2} \left( \sqrt{1 - \frac{1}{1 + (\frac{2r}{d})^2}} \right) \approx \frac{1}{40}. \quad (4.2)$$

Additional losses of 4% arise due to absorption in the objective and another 6% by a narrow bandpass filter<sup>15</sup> used to suppress all light outside the wavelength range 393 nm to 397 nm. In the present setup we image the ions on two PMT's whose outputs are combined with a fast adder and then counted with a multi-purpose counter card<sup>16</sup>. In one of the imaging channels a switching box (mirror, 90:10 beamsplitter, coated window) allows us to send all light to the PMT, to distribute it between a CCD-camera and the PMT or to send all light to the camera. In front of both PMT's, at the location of the image, a variable slit aperture<sup>17</sup> is installed to suppress stray light. The imaging plane is about 1.5 m behind the objective which results in a magnification of 24.5. For all experiments conducted in this thesis, unless mentioned otherwise, state detection was performed with the PMT.

The quantum state of a single ion is detected with a PMT in the following way. For a given

<sup>15</sup>PMT II : Semrock FF01-390/18-25; PMT I : Semrock FF01-377/50-23.7-D

<sup>16</sup>National Instruments, PCI 6711

<sup>17</sup>Owis, Spalt 40

## 4.5 Fluorescence detection

---

amount of time, typically 3 ms, the fluorescence lasers at 379 nm and 866 nm are switched on and all photons detected during that time are added up by a counter card<sup>18</sup>. If the number of detected photons is below a certain threshold we assign the  $D_{5/2}$  state to the result, if it is above the threshold we assign the  $S_{1/2}$  state. The number of events above/below the threshold relative to the total amount of repetitions determines the probabilities  $p_1$  and  $p_0$  corresponding to  $|\alpha|^2$  and  $|\beta|^2$  of equation (2.1). This state discrimination also works for multiple ions by setting  $k$  thresholds and determining the  $p_k$  probabilities of  $k$  fluorescing ions. A typical histogram for the counts acquired for two ions in 3 ms with 3000 repetitions for an equal superposition of  $S_{1/2}$  and  $D_{5/2}$  can be seen in figure 4.5(a).

For the experiments conducted in chapter 7 it was important that the ions are not heated during detection as additional entangling operations had to be carried out after the state detection. Up to three state detections were required during one experiment. Thus a short detection time was essential in order to prevent a loss of phase coherence of the unmeasured quantum bits due to decohering processes occurring during the detection interval. Finally the detection fidelity had to stay above 99%. In order to fulfill all requirements we installed a second PMT and added its output to the first one and switched off/shielded all light sources in the lab. With this effort we were able to detect on average 7.8 photons within 250  $\mu$ s at a dark count rate of 0.07 when using a 397 nm laser that had its power and detuning set as for Doppler cooling. This ensured that the ions stayed at the Doppler limit during the detection. The signal to noise ratio  $>100$  enabled us to get low conditional probabilities for wrong quantum state assignments. The probability of detecting 0 or 1 photons even though the ion was in the bright state, was  $p(D|S) = 0.24\%$ . The probability of detecting more than one photon was  $p(S|D) = 0.39\%$  if the ion was in the dark state.

The second device used in some experiments for detecting the quantum state of the ions is an Electron Multiplying Charge Coupled Device (EMCCD)<sup>19</sup> camera. The focal plane of the imaging system is chosen such that the ions are imaged onto the camera chip. For state detection it is possible to define a region of interest (ROI) around the positions of the ions of typically  $10 \times 40$  pixels for two ions. Only this small region has to be read out, digitized and processed instead of the full  $1024 \times 1024$  pixels. The spatial information in the fluorescence signal obtained with the camera enables us to determine not only the number of fluorescing ions but also which ion(s) is(are) fluorescing. For a proper state discrimination two reference pictures are taken: One with all ions fluorescing, the other one with switched-off 866 nm laser for a background picture. These two pictures are subtracted from each other and then all vertical pixels are added up resulting in a fluorescence image of the ion string that is integrated in the direction perpendicular to the string. Then a Gaussian is fitted to every single peak. From these fits the  $2^N$  different possible states are being built serving as reference pictures to be compared with the picture of an ion string whose quantum states are to be measured. To determine the outcome of an experiment all pictures are treated in a similar way as the reference pictures. First the reference background is subtracted, then all vertical pixels are added up and the result is multiplied with all  $2^N$  reference states. A maximum likelihood method then determines the outcome of the measurement. With this method single ion state detection can be done within 5 ms with a fidelity exceeding 99%. State discrimination with the camera is technically more demanding than the PMT detection as

---

<sup>18</sup>National Instruments, PCI 6711

<sup>19</sup>Andor iXon DV885JCs-VP, pixel size  $8 \times 8 \mu$ m, quantum efficiency at 397nm 37%

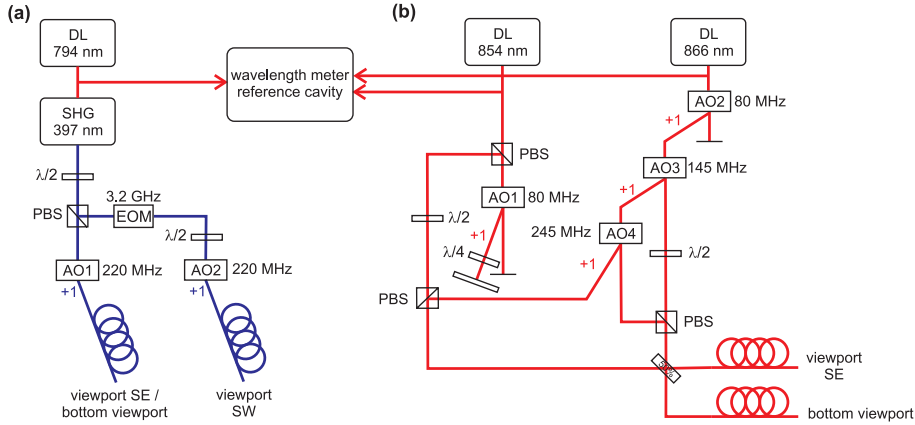


**Figure 4.6.:** (a) 397 nm laser setup providing the light for Doppler cooling, state detection and optical pumping. The EOM at 3.2 GHz generates sidebands on the light to address both of the  $^{43}\text{Ca}^+$  hyperfine ground states. (b) Laser setup for generating the light at 854 nm and 866 nm for repumping the D-states. Both light sources are combined on a 50:50 beamsplitter and sent with two polarization maintaining fibers to the vacuum vessel. For efficiently repumping the  $D_{3/2}$  state in  $^{43}\text{Ca}^+$  two additional AOM's modulate frequencies at 145 MHz and 245 MHz onto the 866 nm beam.

an additional program is required for controlling the camera and evaluating the pictures taken. Furthermore this program has to be synchronized with the experiment control software to ensure proper state detection.

## 4.6. Laser system

An advantage of calcium ions is that all necessary wavelength can be produced by solid state lasers. For all dipole transitions commercial diode laser systems from Toptica were employed in the experiments. The light for driving the  $S \rightarrow P$  transitions was generated by second harmonic generation of near infrared diode lasers. All diode lasers are stabilized to medium finesse ( $\mathcal{F}=300$ ) cavities (see Jan Benhelms thesis [94]) with the Pound-Drever-Hall method. The error signal is fed back onto the piezo of the diode laser grating as well as on the current driving the diode. This reduces the laser line width to about 100 kHz limited by acoustic vibrations of the cavity mirrors. The frequency of the diode lasers can be tuned by 3 GHz by changing the cavity length with a piezo attached to one of the mirrors. The free-spectral range (FSR) of the cavities is 1.5 GHz. The only laser that is not a diode laser is the narrowband titanium-sapphire (Ti:Sa) laser at 729 nm. It is stabilized to a high finesse cavity in order to achieve a line width below 10 Hz. The experimental setup of all laser sources will be described in the following sections.

### 4.6.1. Lasers for Doppler cooling, state detection, optical pumping and repumping

#### Laser at 397 nm

For Doppler cooling, state detection, optical pumping and repumping the ions are excited on the 397 nm dipole transition from  $S_{1/2}$  to  $D_{5/2}$  (see figure 2.3 and figure 2.4). This light is generated by frequency doubling a diode laser system<sup>20</sup> running at 794 nm. At the output of the doubling stage we have between 5 and 10 mW of blue light which is split by a polarizing beamsplitter (PBS) into a  $\sigma$  beam and a  $\pi$  beam (see figure 4.6(a)). Both beams are switched on and off by acousto-optical modulators (AOM)<sup>21</sup> driven at 220 MHz. In the  $\sigma$  beam line there is an additional electro optic modulator (EOM)<sup>22</sup> creating sidebands on the light. This is necessary to couple both hyperfine manifolds in the  $S_{1/2}$  ground state of  $^{43}\text{Ca}^+$  to the  $P_{1/2}$  hyperfine states. Both light beams are sent with polarization maintaining single-mode fibers to the vacuum vessel. The  $\sigma$  beam is sent onto the ions from the NW viewport with a  $\sigma^+$  polarization while the  $\pi$  beam enters the vacuum vessel either on the SE-viewport or the bottom viewport. An additional frequency-doubled laser system is available which can be tuned from 393 nm to 397 nm. Currently it is used to generate a 400 MHz red-detuned beam at 397 nm for Doppler cooling. This beam is needed to efficiently recrystallize two ions after a melting of the ion crystal e.g. due to a background collision. It is superimposed with the  $\sigma$  beam on a PBS having a  $90^\circ$  rotated polarization.

#### Repumping lasers

For repumping the ion from the  $D_{3/2}$  and  $P_{1/2}$  states light at 854 nm and 866 nm is needed. This light is provided by two diode laser systems<sup>23</sup>. The 854 nm laser is switched on and off by an 80 MHz AOM in double pass configuration to ensure proper switch-off(see figure 4.6(b)) of the laser beam. The 866 nm laser is switched by a single pass 80 MHz AOM. AOM's at 145 MHz and 245 MHz create additional light beams that are recombined at beamsplitters for efficiently repumping  $^{43}\text{Ca}^+$ . This increases the Doppler cooling efficiency and the fluorescence signal. These AOM's are only used when running the experiment with  $^{43}\text{Ca}^+$  ions. The light beams of both lasers are superimposed on a 50:50 beamsplitter and then sent to the SE and the bottom viewport of the vacuum vessel by two polarization maintaining single-mode fibers.

### 4.6.2. Ultra-stable titanium-sapphire laser at 729 nm

With a laser at a wavelength of 729 nm we have the capability of exciting the ions on the  $S_{1/2}$  to  $D_{5/2}$  quadrupole transition. Such a laser offers multiple applications, like:

- spectroscopy on the quadrupole transition
- sideband cooling to the motional ground state
- frequency resolved optical pumping

---

<sup>20</sup>Toptica DL-SHG

<sup>21</sup>Crystal Technology, 3220-120

<sup>22</sup>New Focus, 4431

<sup>23</sup>Toptica, DL100

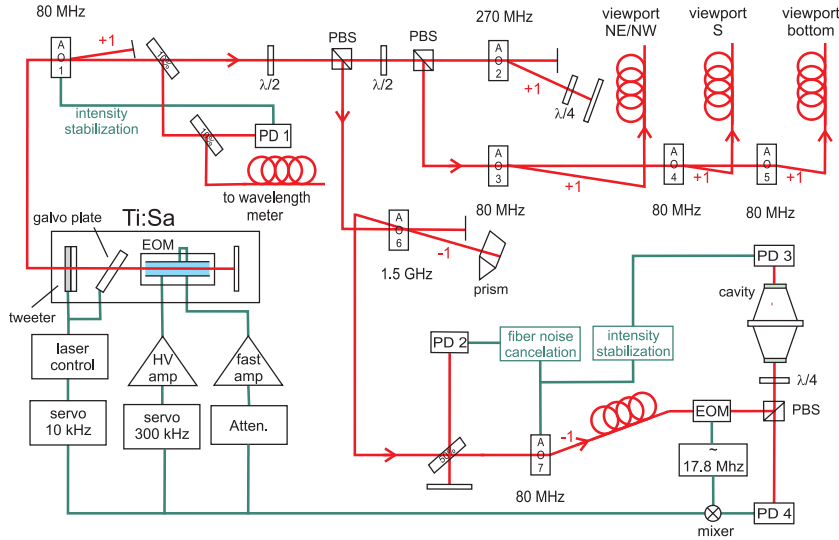


**Figure 4.7.:** Laser setup to provide 3 different 729 nm light beams and the light used for stabilizing the laser onto a high finesse cavity. The light intensity of the Ti:Sa is stabilized by feeding back the signal of PD1 to the RF power driving AO1. AO2 is used for intensity, frequency and phase manipulation of the light sent to the ions. AO3 to 5 are used as switches to guide the light through fibers to different ports of the vacuum chamber. The feedback to the Ti:Sa using a Pound Drever Hall scheme is threefold. A low frequency feedback onto the tweeter and the Brewster plate as well as a mid and a high frequency feedback to an intracavity EOM is applied.

- coherent manipulation of optical qubits
- optical shelving for state detection
- state transfer and initialization

These tasks are very demanding regarding the laser's frequency and power stability. Furthermore it necessary to tune the laser over 100 MHz within a microsecond and set it to different transitions for  $^{43}\text{Ca}^+$  and  $^{40}\text{Ca}^+$  which have a frequency difference of 5.5 GHz. The setup of the laser and its performance is described in [94] and [118]. Here the idea of the locking scheme is recapitulated and the optical setup is described.

To meet all requirements listed above, the laser is stabilized to a vertically mounted [119] high finesse cavity<sup>24</sup> ( $\mathcal{F} = 412\,000$ , line width = 4.7 kHz, FSR = 2 GHz) made out of ultra low expansion material (ULE). It rests on teflon feet inside a temperature stabilized ( $\pm 1$  mK) vacuum tank ( $10^{-8}$  mbar). The vacuum tank is inside a temperature stabilized wooden box shielding the cavity from acoustical perturbations. Typical drift rates of the cavity measured by referencing it to the ions (see chapter 5) are 3 Hz/s or less which means that the cavity spacer length changes within a year by no more than 20 nm.

This high stability comes at the price of being unable to tune the cavity as both mirrors are optically contacted to the ULE spacer. In order to get the necessary tuning range we use an AOM<sup>25</sup> with a center frequency of 1.5 GHz and a tuning range of 1 GHz in double-pass configuration. With

<sup>24</sup>Advanced Thin Films, CO, USA

<sup>25</sup>Brimrose GPF-1500-1000

## 4.6 Laser system

---

this AOM, located between the laser output and the high finesse cavity (see figure 4.7 AO6), we are thus able to tune the laser to any desired frequency. The AOM also allows us to cancel the drift of the cavity by comparing the laser frequency with the ions transition frequency and feeding back on the frequency of the AOM.

The optical setup and the servo loop for the Ti:Sa laser are shown in figure 4.7. The feedback signal is generated by a Pound-Drever-Hall (PDH) [120] locking scheme. An EOM<sup>26</sup> modulates sidebands onto the light and the light reflected by the cavity creates the error signal detected by a photodiode (P4). The locking scheme of the laser consists of three parts. Slow fluctuations are actively canceled by sending the error signal through a PI-servo and applying it to the piezo (tweeter) moving one of the Ti:Sa cavity mirrors and the scanning brewster plate. This loop has a servo bandwidth of 10 kHz limited by the mechanical resonances of the piezo. A higher servo loop bandwidth is achieved by inserting an EOM inside the laser cavity. By changing the refractive index of the EOM the effective cavity length is stabilized. On one electrode of the EOM we apply the error signal sent through a fast proportional amplifier<sup>27</sup>(10 MHz bandwidth). The other electrode is connected to a high voltage amplifier<sup>28</sup> (up to 400 V) which receives as an input the error signal sent through another PI-servo. The grounds of the two amplifiers are connected, thus the EOM is floating. With this setup we get servo bandwidths of 300 kHz for the high voltage part and 1.6 MHz for the fast amplifier.

The laser and the high finesse cavity are coupled by a polarization maintaining single-mode fiber. To avoid a frequency broadening of the light transmitted through the fiber by acoustic noise, we implemented an active fiber noise cancelation [118, 121]. The light passing the fiber is first sent through a 50:50 beam splitter. One part is retro-reflected by a mirror and sent onto a photodiode. The second part is sent through an 80 MHz AOM (see figure 4.7 AO7) and then through the fiber. The end-facet of the fiber is at right angle, thus 4% of the light intensity are back-reflected. The back-reflected light again passes the AOM and hits the same photodiode as the incoming beam. The beat note at 160 MHz contains the phase fluctuation imprinted on the light by the fiber. An error signal is created by comparing the beat note to a stable frequency source<sup>29</sup>. By implementing a phase locked loop, the frequency of the beat signal is kept in phase by feeding back onto a voltage controlled oscillator providing the input signal of the AOM. The light power sent through the fiber is power-stabilized by monitoring the power transmitted through the high finesse cavity. In this way beam pointing and polarization variations are also canceled such that the PDH error signal is not affected.

For the experiments described in chapters 6 to 8 the line width of the 729 nm laser and its spectral purity plays a crucial role. To determine these quantities we performed a beat measurement with a similar laser located at another institute 500 m away. A fiber was used to transmit the light from one building to the other. To avoid any line width broadening of the light we employed a fiber noise cancelation. The slow relative drift of the lasers was canceled by applying a continuous slow frequency change to AO7. The spectrum of the beat signal at a center frequency of 10.8 MHz was recorded with a spectrum analyzer. Figure 4.8(a) shows the power spectrum of the beat for

---

<sup>26</sup>Linos/Gsänger PM25

<sup>27</sup>Femto HVA-10M-60-F

<sup>28</sup>base on Apex, PA98

<sup>29</sup>Rhode & Schwarz, SML01

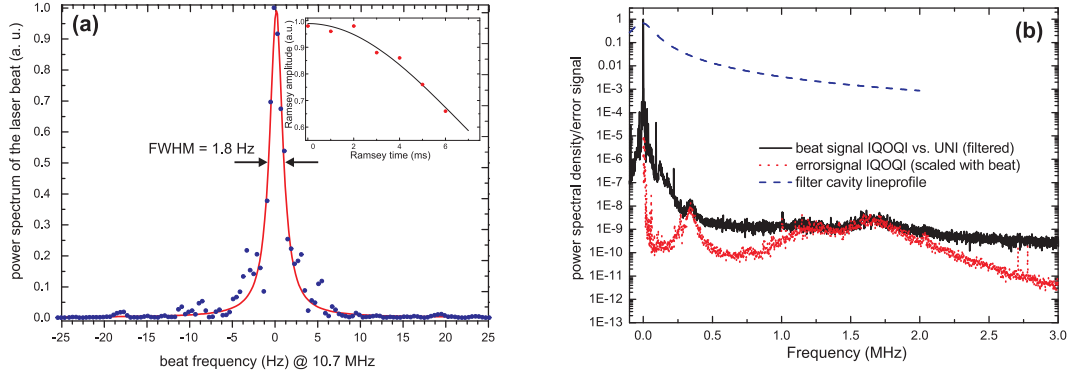


**Figure 4.8.:** (a) Beat measurement of two 729 nm laser connected via a 500 m long noise stabilized fiber. A Lorentzian fit yields a FWHM line width of 1.8 Hz within a measurement interval of 4 s. The inset shows the result of Ramsey experiments on the magnetic field insensitive transition  $S_{1/2}, F = 4, m_F = 4 \rightarrow D_{5/2}, F = 4, m_F = 3.$  of  $^{43}\text{Ca}^+$ . The contrast of the Ramsey experiments is plotted versus the Ramsey waiting time. The red line is a Gaussian fit to the data with a FWHM of 8.1 ms reflecting the loss of coherence due to the finite laser line width and additional frequency noise introduced by a 2 m fiber guiding the light to the ions. (b) Power spectral density of the laser beat with a resolution bandwidth of 1 kHz where the reference laser was spectrally cleaned with a filter cavity. The transmission curve of the filter cavity is given by the blue dashed line. The measurement is limited by the dynamic range of the spectrum analyzer and the reference laser as can be seen from the normalized spectrum of the error signal. An integration of the power spectrum shows that a fraction of less than  $10^{-4}$  of laser light power is outside a  $\pm 250$  Hz window around the laser's carrier frequency.

a 4 s acquisition time and a resolution bandwidth of 1 Hz. A Lorentzian fit yields a FWHM line width of 1.8 Hz. If we assume both lasers have the same Lorentzian frequency spectrum we get a line width for each laser of 0.9 Hz.

To get a better picture of the spectral features of our laser, the spectrum of the second laser was cleaned with a filter cavity. The transmission function of this cavity is given in figure 4.8(b) together with the normalized power spectral density of the beat measurement for a resolution bandwidth of 1 kHz. The figure also shows the spectrum of the laser lock error signal. By comparing both spectra we can easily identify the characteristic humps in the spectrum as “servo bumps“ of the laser. Furthermore we can conclude that the beat measurement is limited by the reference laser and the dynamical range of the spectrum analyzer. An integration of the power spectrum shows that a fraction of less than  $10^{-4}$  of laser light power is outside a  $\pm 250$  Hz window around the laser's carrier frequency.

For time scales larger than the 4 s used to determine the spectrum the beat is dominated by an oscillatory frequency variation with a few seconds period. This accumulates to an effective line width of 50 Hz in a 4 h acquisition time. This is also consistent with Ramsey measurements performed on the magnetic field insensitive transition  $S_{1/2}, F = 4, m_F = 4 \rightarrow D_{5/2}, F = 4, m_F = 3.$  of  $^{43}\text{Ca}^+$  (see figure 4.8(a) inset). From the Gaussian fit to the data we determine a FWHM decay time  $\tau_{1/2}$  of the Ramsey contrast of 8.1 ms. This decay time can be directly transferred into an

## 4.7 Computer control and RF generation

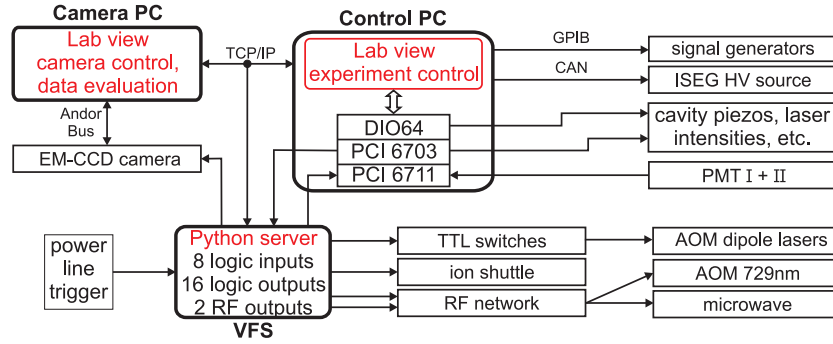


**Figure 4.9.:** Sketch showing the interconnection of different hardware components. The experiment is controlled by a LabView program running on a windows computer (main PC). Additionally a computer controlling the camera and performing automatized data evaluation is connect via a TCP/IP connection. The main computer controls the remaining hardware, reads out the counter data of the PMT and programs the versatile frequency source (VFS). The VFS is triggered by the AC power line and provides TTL signals and all phase-synchronous radio frequency signals.

effective laser line width with [122]

$$\Delta\nu = \frac{2 \ln 2}{\pi} \frac{1}{\tau_{1/2}}. \quad (4.3)$$

From this formula we can infer a laser line width on the ions of 55 Hz for a measurement time of 10 Minutes.

The output of the laser is intensity stabilized by monitoring a small portion of the light by a photodiode<sup>30</sup> (PD1), comparing it with a stable voltage reference and feeding back the error signal onto the RF power driving AO1. The frequency and intensity of the light sent to the ions is controlled by AO2. We can choose between three different fiber ports which are switched on and off by AO3 to 5. AO3 can be driven simultaneously by two frequencies to create a bichromatic light field. Typically the frequency difference between the two beams is 2.4 MHz which leads to a diffraction into slightly different directions with an angular separation as small as 0.025° such that the coupling efficiency to the single mode fiber is reduced by about 15% compared with a single frequency beam.

## 4.7. Computer control and RF generation

Qubits in ion trap quantum information experiments are manipulated by laser pulses whose power and length have to be controlled. Furthermore phase coherence has to be ensured for all pulses. This can be achieved by using AOMs which directly transfer the frequency, power and phase information from the radio frequency onto the light. In this way, the problem is reduced to generating precisely timed digital signals and phase-coherent radio frequency pulses with adjustable length and amplitude. For this purpose a versatile frequency source [105, 123] (VFS) was developed. It is based on a field programmable gate array (FPGA) which controls a direct digital synthesis (DDS) board. This DDS board can generate pulses with 16 different frequencies in the range of

<sup>30</sup>Thorlabs PDA 100A-EC

0-300 MHz and allows for phase coherent switching between them. The pulses have a minimal duration of 10 ns but are typically in the range of 1  $\mu$ s to 1 ms. The amplitude and shape of the pulses are controlled by a variable gain amplifier. The frequency range of the DDS board is limited by filters to 300 MHz. Higher frequencies like the 3.2 GHz for driving the hyperfine qubit are created by appropriate mixing and filtering of the signals. The frequency resolution is about 0.1 Hz. Additionally up to 16 logic channels (TTL) can be used which are also set by the FPGA controller. These TTLs are used to control all fast and precisely timed switching required during an experimental cycle. Logic signals can be sent to the FPGA via 8 input channels.

The FPGA is connected to a PC (main PC) by an ethernet connection and is programmed via a python<sup>31</sup> server. Figure 4.9 shows a sketch of the interconnections between the different hardware components. The software running on the main PC controlling the experiment is written in LabView. This program is used to send command sequences to the FPGA board which are executed as soon as it receives a trigger on one of its input channels. Sequences run synchronously with the 50 Hz power line cycle to avoid varying magnetic fields from one execution to the next. This is again insured by a trigger to one of the input channels. The LabView program also controls several National instrument cards<sup>32</sup>. They are used to generate analog signals for controlling the power and frequency of the dipole lasers. TTL outputs of these cards are used to switch time-noncritical signals.

The PMT signals acquired by the counter card during an experiment are read out, processed and displayed by the LabView program. The program can be used to run automatized sequences. The data acquired during such sequences can be sent to the camera PC for data evaluation and model fitting. The values determined by these procedures are then fed back into the LabView program. A typical application consists in calibrating the duration of all pulses required in a sequence.

Another LabView program running on the camera PC controls the camera hardware and is responsible for read-out and evaluation of the camera pictures. The programs on both computers are communicating via ethernet.

Signal generators are computer controlled by a GPIB-Bus<sup>33</sup>. The ISEG high voltage source providing the tip voltage is connected by a CAN-bus<sup>34</sup> to the control PC.

To ensure phase-coherence between all RF-signals the signal generators as well as the VFS-box are referenced to a 10 MHz GPS assisted quartz oscillator<sup>35</sup>.

---

<sup>31</sup>High-level programming language

<sup>32</sup>National Instruments PCI 6711, PCI 6703, DIO 64

<sup>33</sup>IEEE-488

<sup>34</sup>Controller area network, serial bus standard

<sup>35</sup>Menlo Systems GPS 6-12

---

## 5. Experimental techniques

This chapter will outline techniques used on a daily basis in the laboratory. It will explain how to load ions into the trap and detail the structure of a typical experimental sequence. An important point is the referencing of the 729 nm laser to the ions, which is one of the key elements for doing high precision spectroscopy and QIP experiments. Then implementation of arbitrary qubit operations will be demonstrated with the help of ion shuttling and the capability of single ion addressing. How to analyze the state of an ion by state tomography will be presented at the end of this chapter.

### 5.1. Loading ions by photoionization

Typically, ions are loaded by photoionization of an atomic beam produced by an oven. The oven consists of a stainless steel tube which is heated by an electric current. The tube is about 8 cm long to ensure a proper collimation of the beam through the trap center, thus avoiding excessive deposition of calcium on the trap electrodes. The photoionization beam is sent through the trap center at a slightly different angle. The ions are directly ionized inside the trap volume. Compared to loading by electron impact it has several advantages. Electron bombardment creates patch charges on the trap which have to be compensated in order to avoid micromotion. It requires a higher atomic flux to get a decent loading rate because this ionization process is five orders of magnitude smaller as compared to photoionization. This leads to bigger calcium layers on the trap surfaces which increases the patch charge problem. Furthermore, electron bombardment is not isotope selective and even atoms from the background gas can be ionized. Especially this point is of importance as we want to load  $^{40}\text{Ca}^+$  and  $^{43}\text{Ca}^+$  deterministically.

Calcium is photoionized by a two step process (see figure 5.1(a)). A laser in Littrow configuration at 423 nm resonantly excites the atom from the  $4s^1S_1$  to the  $4p^1P_1$  state. From there it can be ionized by a second step using light with a wavelength smaller than 390 nm. In the experiment we use a free-running laser diode at 375 nm. Both beams are superimposed on a beamsplitter cube and sent through a single-mode fiber towards the ion trap via the SE-viewport of the vacuum chamber (see figure 4.3). Typically 50 to 100  $\mu\text{W}$  for the 423 nm laser and about 500  $\mu\text{W}$  for the 375 nm laser are used for efficient loading.

Isotope selective loading can be achieved by tuning the 423 nm laser to the  $4s^1S_0 \leftrightarrow 4p^1P_1$  resonance (see figure 5.1(b)) of the respective isotope. The frequency of the 423 nm laser can be determined either on the wavemeter or by saturation spectroscopy on a calcium vapor cell. The spectroscopy clearly shows the Doppler-free resonance for the most abundant calcium isotope  $^{40}\text{Ca}$ . By detuning the laser by 612 MHz to the blue it becomes resonant with the  $^{43}\text{Ca}$  resonance. Due to the finite Lorentzian line shape and the natural abundance of calcium the relative loading rate of

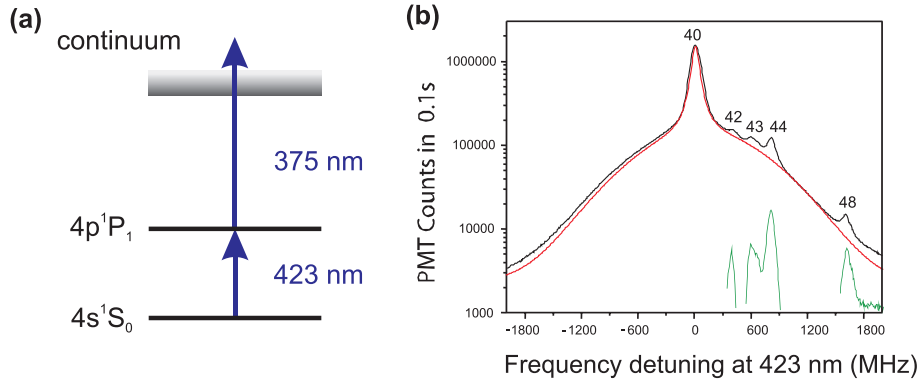


**Figure 5.1.:** (a) Two step photoionization of calcium. The 423 nm laser can be used to make the process isotope selective. (b) Excitation spectrum of calcium at 423 nm. Figure is taken from [124]. The numbers above the curve show the resonances of the respective calcium isotopes.  $^{43}\text{Ca}^+$  has an isotope shift of 612 MHz with respect to the  $^{40}\text{Ca}^+$  resonance. The red line is fit to the measured data taking into account a single resonance for  $^{40}\text{Ca}^+$ . The residuals between the red and the black curve are shown in green and indicate the resonances of other isotopes.

$^{43}\text{Ca}^+$  compared to other isotopes is only 50%. To further increase the isotope selectivity there are two ovens in the apparatus. One is filled with calcium granules with a natural isotope abundance of 97%  $^{40}\text{Ca}$  and the other is filled with an enriched source consisting of 81%  $^{43}\text{Ca}$ , 13%  $^{40}\text{Ca}$  and 5%  $^{44}\text{Ca}$ .

For loading calcium ions the Doppler cooling laser at 397 nm, the repumper at 866 nm and both photo-ionization lasers are continuously on. The current in the oven is set such that about two ions are loaded per minute. By monitoring the fluorescence signal with the PMT and/or camera, ions appearing in the trap can be detected. Larger crystals are loaded by waiting for longer times. In case that too many ions are in the trap all of them have to be discarded by switching off the RF drive. Then the loading procedure is started again.

After the intended number of ions has been loaded, the Doppler cooling lasers are adjusted for optimum detuning and power [92]. Two different power settings for the 397 nm laser have to be optimized: One for proper Doppler cooling, to get as close as possible to the Doppler-limit and the other for a maximum fluorescence to get a good state detection. The parameters for the two settings will be given in the following section. When all dipole lasers are properly set we can start running experimental sequences manipulating the qubit.

## 5.2. Experimental sequence

All experiments are executed in a pulsed fashion. Such a sequence typically consists of six building blocks (see figure 5.2) which are described in the following. A single experiment is typically repeated 50-200 times.

## 5.2 Experimental sequence

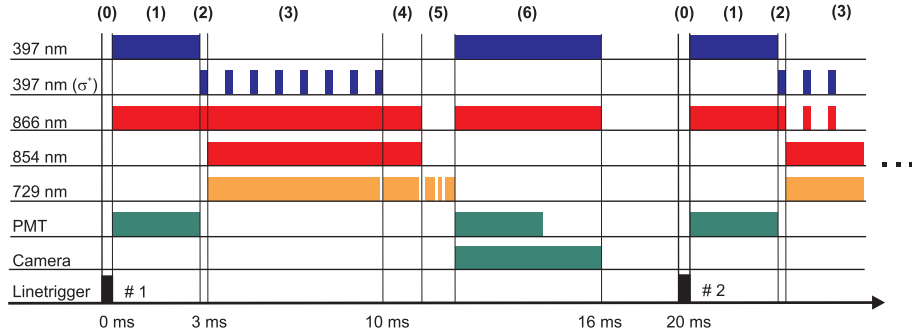


**Figure 5.2.:** Typical sequence of laser pulses executed in an experimental cycle. (1) Doppler cooling, (2) optical pumping, (3) sideband cooling, (4) frequency resolved optical pumping, (5) quantum state engineering, (6) state detection. Each sequence is triggered by a TTL pulse (0) synchronized with the line cycle and is typically repeated 50, 100 or 200 times.

### (1) Doppler cooling

For  $^{40}\text{Ca}^+$ , it is sufficient for efficient Doppler cooling to use a single 397 nm beam coupling  $S_{1/2} \rightarrow P_{1/2}$  and a single 866 nm laser repumping the transition  $D_{3/2} \rightarrow P_{1/2}$ . To cool all three normal modes of motion of the ion in the trap, care has to be taken that the Doppler-cooling beam has sufficient overlap with all modes. The power of the 397 nm laser is set such, that its Rabi frequency is half the saturation intensity [92] of the dipole transition. It is red detuned with respect to the resonance by half the linewidth of the transition. The 866 nm laser power is set such that the fluorescence is just below saturation to avoid additional line broadening. It is slightly blue detuned to avoid coherent population trapping. The degeneracy of the Zeeman sublevels is lifted by a magnetic field.

For  $^{43}\text{Ca}^+$  Doppler cooling is a little bit more complicated. Here three light fields for the 397 nm laser are necessary. Two of the light fields are  $\sigma^\pm$ - polarized, where one is coupling the  $S_{1/2}, F = 4 \rightarrow P_{1/2}, F = 4$  transition and the other one, detuned by 3.2 GHz, is coupling the  $S_{1/2}, F = 3 \rightarrow P_{1/2}, F = 4$  transition. The 3.2 GHz component is created by modulating sidebands on the light field with an EOM (see figure 4.6). The third light field is a  $\pi$  polarized beam which is needed to avoid pumping into the dark state  $S_{1/2}, F = 4, m_F = 4$ .

In the experiment it turned out that the  $\pi$  and the  $\sigma^+$  beam should not have the same frequency. If they do, Doppler cooling is not working properly which might be due to dark states that are inefficiently cooled. A detuning of 5 MHz to the red for the  $\pi$  beam, with respect to the  $\sigma^+$  light field, turned out to yield the best Doppler cooling results. The 866 nm laser is tuned close to the  $D_{3/2}, F = 3 \rightarrow P_{1/2}, F = 3$  transition. For efficient repumping additional light fields shifted by -145 MHz and -395 MHz are provided (see figure 4.6). In this way all  $D_{3/2}$  hyperfine levels are coupled to one of the  $P_{1/2}$  states. Power and detuning from the resonances for both lasers are set the same way as for  $^{40}\text{Ca}^+$ . A magnetic field lifts again the degeneracy of the Zeeman states.

The fluorescence collected during Doppler cooling is used to check if the ions are in a crystal-like structure. If the fluorescence collected for a single sequence falls below a certain threshold the whole experiment is discarded and executed again.

## (2) Optical pumping

A weak short pulse with a  $\sigma^+$  polarized 397 nm laser together with an 866 nm laser pulse is used for optically pumping the ions into either  $S_{1/2}, m_j = 1/2$  for  $^{40}\text{Ca}^+$  or  $S_{1/2}, F = 4, m_F = 4$  for  $^{43}\text{Ca}^+$ . As for Doppler cooling, more light fields have to be used for pumping  $^{43}\text{Ca}^+$ . After this step we achieve a pumping fidelity of 99% into the desired state within 70  $\mu\text{s}$  for  $^{40}\text{Ca}^+$  and about 98% for  $^{43}\text{Ca}^+$  ions. The pumping fidelities are limited by beam polarization and overlap of the  $\mathbf{k}$  vector of the light field with the magnetic field axis.

## (3) Sideband cooling

Sideband cooling to the motional ground state is done in the same way for both isotopes. The 729 nm laser is tuned to the red sideband of the stretched state  $S_{1/2}, m_j = 1/2 \rightarrow D_{5/2}, m_j = 5/2$  for  $^{40}\text{Ca}^+$  and  $S_{1/2}, F = 4, m_F = 4 \rightarrow D_{5/2}, F = 6, m_F = 6$  for  $^{43}\text{Ca}^+$ . Every state transfer from  $S_{1/2}$  to  $D_{5/2}$  reduces the mean phonon number by one quantum. To reduce the lifetime of the  $D_{5/2}$  level a 854 nm laser is switched on at the same time. The population is transferred from the  $D_{5/2}$  state to the  $P_{3/2}$  state from where it decays back to the ground state. To avoid population leaking from the cooling cycle due to a decay into  $D_{3/2}$ , an 866 nm laser is continuously on. This repumping via the  $P_{1/2}$  state does not guarantee a decay into the desired  $S_{1/2}$  state. Additional optical pumping with the 397 nm laser brings the population back into the cooling cycle. After about 7 ms a mean phonon number of  $\langle n \rangle = 0.05(5)$  is reached.

## (4) Frequency resolved optical pumping

To further increase the optical pumping efficiency we make use of the 729 nm laser. The scheme for  $^{40}\text{Ca}^+$  is similar to sideband cooling. For a duration of 500  $\mu\text{s}$  the 729 nm laser is switched on together with the 866 nm and 854 nm laser. The quadrupole laser couples the states  $S_{1/2}, m_j = -1/2 \rightarrow D_{5/2}, m_j = 3/2$  depleting the undesired Zeeman state. Due to the repumping the population piles up in the  $S_{1/2}, m_j = 1/2$  and we get pumping efficiencies exceeding 99.8% for a single ion.

In  $^{43}\text{Ca}^+$  we transfer the population in  $S_{1/2}, F = 4, m_F = 4$  to the  $D_{5/2}, F = 6, m_F = 6$  state. Then we again apply an optical pumping step with the 397 nm laser. This redistributes the population remaining in the ground state. Another  $\pi$  pulse exchanges the populations in  $S_{1/2}, F = 4, m_F = 4$  and  $D_{5/2}, F = 6, m_F = 6$ . After this step 98% of the population should be in  $S_{1/2}, F = 4, m_F = 4$  and the rest in  $D_{5/2}, F = 6, m_F = 6$ . A light pulse with 854 nm laser clears out the  $D_{5/2}$  state via the  $P_{3/2}, F = 5, m_F = 5$  from where it can only decay into  $S_{1/2}, F = 4, m_F = 4$ . With this procedure we achieve pumping fidelities for a single  $^{43}\text{Ca}^+$  ion of more than 99.4%.

## (5) Quantum state manipulation

After the ions are prepared in the motional ground state and the desired electronic state, the qubit in  $^{40}\text{Ca}^+$  and  $^{43}\text{Ca}^+$  can be manipulated by 729 nm laser pulses. If the qubit is encoded in the hyperfine states of  $^{43}\text{Ca}^+$  it can also be manipulated by microwave pulses.

### 5.3 Referencing the 729 nm laser to the ions

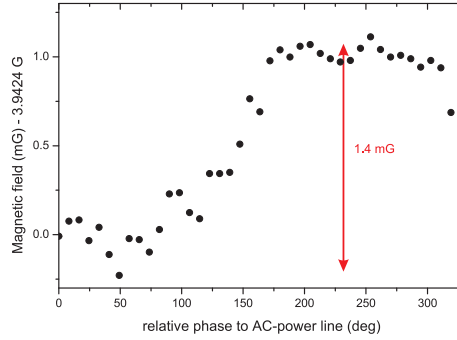


**Figure 5.3.:** Variation of the magnetic field over the line cycle. The data points were measured by delaying the start of a Ramsey experiment with respect to the line trigger. The strong 50 Hz component is most likely caused by transformers and other electronics of the setup.

#### (6) State discrimination

By detecting the fluorescence of the ion on either the camera or the PMT one can distinguish between the  $S_{1/2}$  level and the  $D_{5/2}$  level. The power of the 397 nm laser is increased for a high fluorescence rate to get a good state discrimination within a few milliseconds. To discriminate between the states of the hyperfine qubit  $S_{1/2}, F = 4, m_F = 0$  and  $S_{1/2}, F = 3, m_F = 0$ , additional transfer pulses are used to hide the  $S_{1/2}, F = 4, m_F = 0$  population in the  $D_{5/2}$  manifold. Two transfer pulses to different  $D_{5/2}$  Zeeman states ensure that the detection efficiency is above 99%.

### 5.3. Referencing the 729 nm laser to the ions

In order to make use of the 729 nm laser for QIP experiments an exact knowledge of the magnetic field and the laser frequency is necessary. Therefore the laser is referenced to the ions in the trap. The referencing is done by probing two different transitions  $(a, b)$  in either  $^{40}\text{Ca}^+$  or  $^{43}\text{Ca}^+$ . From the exact knowledge of the Zeeman splitting of the transitions one can then infer the relative laser frequency and the magnetic field. By recording the transitions for several minutes it is possible to determine the drift of the reference cavity and, by active feed forward, to stabilize the output frequency of the laser up to some small fluctuations caused by magnetic field variations.

The ions are Doppler-cooled and initialized by optical pumping. Then a Ramsey type scheme [125] is employed to determine the transition frequency. A  $\pi/2$  pulse creates a superposition of the two levels to be probed. Then after a Ramsey waiting time  $\tau_R$ , a second  $\pi/2$  pulse is applied. One transition is probed twice in this way. The first time the second pulse has a relative phase of  $\phi_1 = \pi/2$  and the second time it has a phase of  $\phi_2 = 3\pi/2$ . After each measurement the population of the levels is measured as described in chapter 4.5. By repeating this sequence a hundred times one can infer the probabilities of finding the ion in the excited state  $p_{\phi_1}$  and  $p_{\phi_2}$  for the respective phases. From this one can determine the frequency difference between the laser and the probed transition as [94]

$$\Delta\nu/(2\pi) = \frac{1}{2\pi(\tau_R + 2\tau_\pi/\pi)} \arcsin \frac{p_{\phi_1} - p_{\phi_2}}{p_{\phi_1} + p_{\phi_2}}. \quad (5.1)$$

Where  $\tau_\pi$  denotes the pulse length to drive a  $\pi$ -pulse on this transition with the chosen laser

power. Typical values for  $\tau_\pi$  are between 5 and 20  $\mu\text{s}$  whereas  $\tau_R$  is typically 10 times longer, that is 0.1-1 ms.

From the deviation of the transition frequencies  $\Delta\nu_a$  and  $\Delta\nu_b$  we first determine the magnetic field. From this knowledge and the frequency of one transition we then determine the transition frequency at zero magnetic field. This serves as a reference from where all other transitions frequencies can be calculated for a given magnetic field.

The referencing measurements and the analysis are fully automatized and run about every minute. The measurements are recorded over time and a polynomial fit to the frequency data reveals the drift of the cavity. Usually a first order fit is employed and an extrapolation is used to feedback on the signal generator producing the frequency for the AOM set up between laser and cavity (see figure 4.7 AO6). With this feedback scheme the laser frequency deviates by less than 200 Hz (rms-deviation) from the transition frequency. The exact value depends on  $\tau_R$  which is limited by the coherence time of the ions, the linearity of the cavity drift and the line width of the probe laser.

The magnetic field data are averaged over time where data older than 5 min are not taken into account. The average is used as a best guess for the magnitude of the magnetic-field during the next minute. The limiting factor in determining the exact magnetic field is given by erratic jumps in the magnetic-field by 100-250  $\mu\text{G}$  due to external magnetic fields (elevator etc.). Without these jumps the magnetic field is stable and can be predicted within about 50  $\mu\text{G}$  over several hours if the experiments are triggered to the line cycle.

If the time between the start of an experiment and the line trigger is varied, changes of the magnetic-field by about 1.4 mG are visible (see figure 5.3). To avoid this variation from shot to shot, experiments are always started at a fixed phase of the power line cycle. Nevertheless, since some of the transitions used exhibit a magnetic field sensitivity of 2.8 MHz/G frequency corrections of up to 4.5 kHz have to be taken into account over the course of a sequence that lasts several milliseconds. To avoid these corrections for short sequences the experiments are triggered to the maximum in the line cycle (around  $250^\circ$ ) such that the magnetic field does not change in first order. Ways to get rid of this limitation are either technical, by active or passive magnetic field stabilization, or by choosing a qubit which is insensitive to magnetic field changes [102, 126]. Such a magnetic field insensitive qubit was used in chapter 6 to store entangled states for tens of milliseconds.

## 5.4. Implementation of arbitrary qubit operations and ion shuttling

There are different approaches to carry out single-qubit rotations. A requirement that is always present is the capability to limit interactions to individual qubits. In the ion trap case this is equivalent to shining in the laser on one ion at a time. One possibility to achieve this is to use micro-fabricated segmented traps to manipulate the ion motion [127]. With the help of different trap electrodes a large ion string can be split into smaller ones and brought to trap zones where the selected ions interact with laser fields [127]. This approach requires a high degree of control and stability on the voltages applied to the trap electrodes. Some experiments have demonstrated

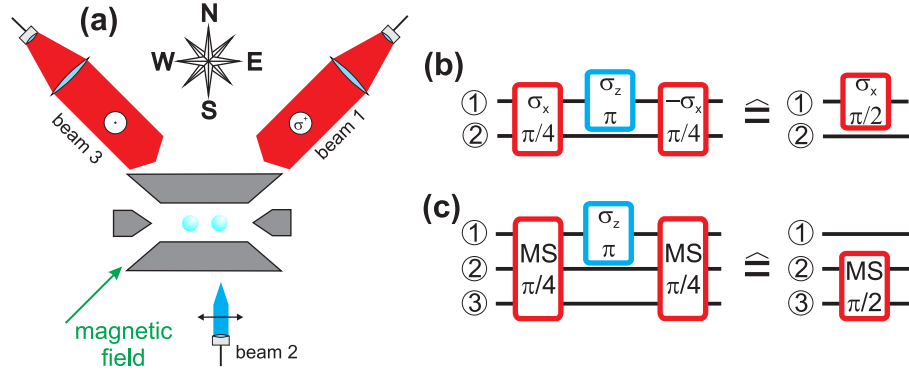


**Figure 5.4.:** (a) Laser beam setup for the 729 nm laser. The tightly focused beam 2 is used for addressed  $\sigma_z$  rotations. The beams 1 and 3 are for simultaneous operations on up to three ions. These beams are either bichromatic light fields for implementing a MS-interaction or single frequency for carrier rotations on all ions. The NE beam is  $\sigma^+$  polarized for driving  $\Delta m = \pm 1$  transitions with maximal efficiency. The NW beam is linearly polarized for driving  $\Delta m = \pm 2$  transitions with maximal efficiency. (b) Pulse scheme to perform a  $\pi/2$  carrier rotation on ion 1 and no rotation on ion 2. Both ions are first rotated by  $\pi/4$ , then ion 1 gets a  $\pi$  phase shift with the AC-stark pulse. The second  $\pi/4$  pulse on both ions rotates ion 2 to the initial state and completes the  $\pi/2$  rotation on ion 1. (c) Pulse scheme to perform a MS-gate on two out of three ions. The first  $\pi/4$  MS-gate partially entangles all three ions. A stark shift pulse on ion 1 changes the phase of this ion by  $\pi$ . The final  $\pi/4$  MS-gate entangles ions 2 and 3 and reverts ion 1 to its initial state.

the ability to deterministically split [128, 129] and reorder an ion string [130]. To do this splitting fast the traps have to be small as the trap frequencies scale as  $d^{-9/10}$  with  $d$  the distance of the ions to the trap electrodes [131]. A problem all traps face is that the heating rate scales as the  $d^{-4}$  [132, 133] which is especially bad for micro-fabricated traps. Although experiments showed that cooling the traps [134] reduces the anomalous heating a considerable technical overhead is required to do QIP with these traps.

Another way to single out ions from a larger crystal is to use strongly focused light beams. Ideally the focus should be much smaller than the separation of two ions which is typically a few  $\mu\text{m}$ . However, even for perfect optics the Gaussian beam profile will lead to some light on the neighboring ion and thus some residual coupling  $\Omega_{res}$ . With our addressing optics for the 729 nm beam (see figure 4.4) we are able to get the ratio  $\epsilon = \Omega_{res}/\Omega$  for carrier pulses down to about 5%. This ratio can be further improved by using Stark shift pulses. As the interaction strength for these scales with the intensity instead of the field strength the addressing error scales now with  $\epsilon^2$ . Addressing errors are thus reduced to below 0.3%. One pays for this increased addressing capability by an increased sensitivity to intensity fluctuations.

Single-qubit light-shift gates  $U_z^{(i)}(\theta) = e^{-i\frac{\theta}{2}\sigma_z^{(i)}}$  are realized by an off-resonant strongly focused beam impinging (see beam 2 in figure 5.4(a)) on ion  $i$  at a  $90^\circ$  angle relative to the trap axis. As the k-vector of this beam is perpendicular to the trap axis this configuration does not allow to couple to the axial center of mass motion of the ions and can thus not be used to do two-qubit gate operations. A second beam at a  $45^\circ$  angle relative to the trap axis (see beam 1 or beam 3 in figure 5.4(a)), illuminating all ions with equal strength serves to carry out gate operations that are symmetric under qubit exchange. Collective single-qubit gates  $U(\theta, \phi) = e^{-i\frac{\theta}{2}(\sigma_\phi^{(1)} + \sigma_\phi^{(2)})}$ , are

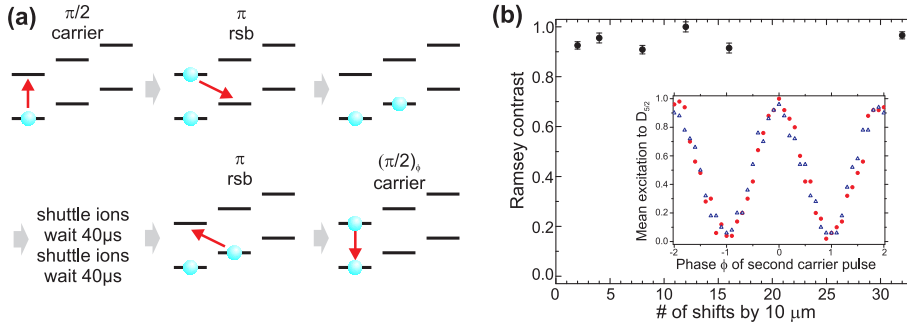


**Figure 5.5.:** (a) Pulse sequence describing a Ramsey experiment on the motional states of the ion. (b) Ramsey contrast of the experiment versus number of events shuttling the ion by  $10 \mu\text{m}$ . The inset shows the contrast of a Ramsey phase experiment on the motion without ( $\bullet$ ) and with ( $\blacktriangle$ ) a single ion shuttle.

realized by resonantly exciting the qubit transition and controlling the phase  $\phi$  of the laser light. If instead a bichromatic light field is used for implementing a Mølmer-Sørensen interaction, the propagator  $U_{MS}(\theta, \phi) = e^{-i\frac{\theta}{2}\sigma_{\phi}^{(1)} \otimes \sigma_{\phi}^{(2)}}$  is realized. This interaction is used for entangling ions.

As the tightly focused beam is static we still have to move the ion string to address different ions. The shuttling of the ions is done in such a way, that the population of the harmonic oscillator mode does not change during the transport. The curvature of the trapping potential is kept constant during the movement of the ions. The movement of the ions is achieved by changing the tip voltage with the circuit presented in chapter 4.1. To avoid energy transfer the ions are accelerated adiabatically with respect to the trapping frequencies. Typical shuttling times for  $10 \mu\text{m}$  of  $40 \mu\text{s}$  corresponding to about 50 axial oscillations were achieved without affecting the population of the COM mode. This was confirmed by performing a Ramsey experiment on the two lowest motional states in the following way: A single ion was cooled to the motional ground state by sideband cooling. A  $\pi/2$  pulse on the carrier followed by a  $\pi$  pulse on the red sideband creates the superposition state  $|\downarrow, 0\rangle + |\downarrow, 1\rangle$ . Then the ions were shuttled over a distance of  $10 \mu\text{m}$  along the trap axis. After a waiting time of  $40 \mu\text{s}$  the ions were shuttled back to the original position. Again a waiting time of  $40 \mu\text{s}$  ensured that the voltage on the electrodes was settled. The sequence applied to the ion is shown in figure 5.5(a). The first two pulses were then applied in reverse order and the phase of the carrier pulse was scanned to record Ramsey fringes (see figure 5.5(b) inset). The contrast of these fringes was then compared to the case where the ion was not transported. If the ion was heated during the transport, i.e. the occupation of the motional mode was incoherently changed, the contrast of the Ramsey fringes decreases with respect to the stationary case. No such effect could be observed even for moving the ion 32 times (see figure 5.5(b)).

It can be shown [135] that combining this set of elementary gates  $\{U_z^{(i)}(\theta), U(\theta, \phi), U_{MS}(\theta, \phi)\}$  arbitrary multi-qubit operations and mapping of observables  $A_{ij}$  to  $\sigma_z^{(k)}$  for read-out can be implemented. This is similar to NMR techniques [15] where the spin-spin interaction that is always present can be switched off by refocusing techniques. The dynamics of the system is thus controlled by single qubit operations. In the ion trap case, the spin-spin interaction is replaced by the MS-gate and the refocusing pulses are implemented with the addressed beam. Two simple examples for such a pulse sequence with ions and their effective circuit diagram are shown in figure 5.4 b

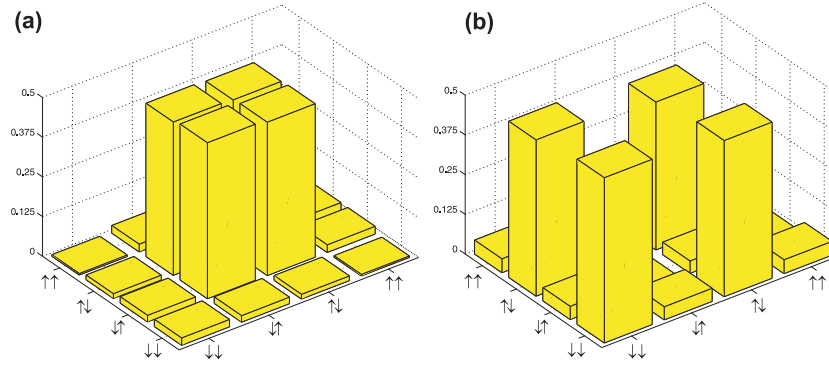


**Figure 5.6.:** Absolute values of the density matrices for the states (a)  $|\uparrow\downarrow\rangle + |\downarrow\uparrow\rangle$  and (b)  $|\downarrow\downarrow\rangle + |\uparrow\uparrow\rangle$  reconstructed by a maximum likelihood method.

and c.

The sequence in figure 5.4 b shows how to do a  $\frac{\pi}{2}$  pulse on only one of two ions. Both ions are first rotated by  $U(\frac{\pi}{4}, 0)$ , then ion 1 gets a phase shift with the AC-stark pulse  $U_z^{(1)}(\pi)$ . The second  $U(\frac{\pi}{4}, \pi)$  pulse on both ions rotates ion 2 to the initial state and completes the  $\pi/2$  rotation on ion 1. Example c is similar to the NMR case and is used to entangle two out of three ions. The first  $U_{MS}(\frac{\pi}{4}, 0)$  MS-gate partially entangles all three ions. A stark shift pulse on ion 1  $U_z^{(1)}(\pi)$  changes the phase of this ion by  $\pi$ . The final  $U_{MS}(\frac{\pi}{4}, 0)$  MS-gate entangles ions 2 and 3 and reverts ion 1 to its initial state. So by flipping the phase of one of the ions the interaction is switched off.

## 5.5. State tomography

State tomography is used to determine the density matrix of a quantum state by measurements on an ensemble of identically prepared quantum states. As described in chapter 2.1.5, a measurement of the expectation values  $\lambda_i$  of the Pauli operators  $\sigma_x, \sigma_y, \sigma_z$  is sufficient to directly reconstruct a density matrix describing a qubit state. For a qubit encoded in the electronic state of a trapped ion,  $\sigma_z$  can be directly measured by detecting the fluorescence of the ion (see chapter 4.5). The other two observables are measured by applying a unitary transformation prior to measuring  $\sigma_z$  on the transformed state. This transformation maps the eigenvectors corresponding to the eigenvalues of  $\sigma_x$  or  $\sigma_y$  onto the eigenvalues of  $\sigma_z$  (see chapter 2.1.3).

For multi-qubit systems it is necessary to measure observables which are tensor products of Pauli matrices. The measurement procedure requires single-ion addressing and single-ion detection capabilities. For two ions, observables like  $\sigma_z^1 \otimes \sigma_y^2$  are determined by applying an addressed rotation on qubit 2 prior to measuring  $\sigma_z^1, \sigma_z^2$  (each  $(\pm 1)$ ) with the CCD-camera. By correlating the results the expectation value for  $\sigma_z^1 \otimes \sigma_y^2$  can be measured by multiplying the  $\pm 1$  outcomes and averaging over all realizations. To reconstruct the density matrix of two qubits nine measurements have to be carried out to determine the 16 expectation values of all products of  $\sigma_i \otimes \sigma_i$  with  $\sigma_i = \{\hat{I}, \sigma_x, \sigma_y, \sigma_z\}$ .

The unitary transformations we apply to the ions are implemented as shown in the preceding chapter. A unitary transformation to measure e.g.  $\sigma_z^1 \otimes \sigma_y^2$  would exactly look like the sequence of pulses shown in figure 5.4(b)

$$U_x\left(\frac{\pi}{4}\right)U_z^1(\pi)U_x\left(\frac{\pi}{4}\right). \quad (5.2)$$

A problem one faces is that in an experiment one can never determine the observables exactly, as an infinite number of measurements is necessary to eliminate the statistical error. Thus a measurement of an expectation value  $\bar{\lambda}_i$  is only a best estimate for the actual expectation value. This seemingly small difference has important consequences as real physical Bloch vectors have to lie inside the Bloch sphere. When a state is reconstructed that is close to the boundary the statistical fluctuations might lead to a single-ion Bloch vector lying outside the unitsphere. In this case the corresponding density matrix has one eigenvalue  $> 1$  and one eigenvalue  $< 1$ . As this matrix is no longer positive semidefinite it does not describe a physical state. This problem gets more severe the higher the dimension of the Hilbert-space becomes as more and more density matrix entries will be close to zero and can easily get negative if not enough data are taken.

This problem can be overcome by making use of the measurement results in another way. The strategy we use to determine the density matrix is based on a maximum likelihood method [136]. This method searches among all physically possible density matrices the one that is most likely to reproduce the observed measurement results. The measurements described above project the quantum state  $\rho_{ex}$  onto a set of different bases. For each of these bases,  $N$  copies of  $\rho_{ex}$  were used, and in  $Nf_i$  experiments  $\rho_{ex}$  was projected onto the state  $|\Psi_i\rangle$ . The probability of finding exactly these results for an arbitrary density matrix  $\rho$  is given by the likelihood function

$$L(\rho) = \prod_j \langle \Psi_j | \rho | \Psi_j \rangle^{Nf_j}. \quad (5.3)$$

The maximum likelihood estimation for an experimentally obtained density matrix is given by the state  $\rho$  that maximizes the log-likelihood function

$$\mathcal{L}(\rho) = N \sum_j f_j \log \langle \Psi_j | \rho | \Psi_j \rangle. \quad (5.4)$$

As  $\mathcal{L}(\rho)$  is a convex function on a convex set, it has no local maxima which simplifies the task of maximizing  $\mathcal{L}(\rho)$ . If a directly reconstructed density matrix is valid it will also maximize the likelihood function, thus both methods reconstruct the same density matrix. Different numerical methods can be used to maximize the log-likelihood function. The method used to reconstruct all density matrices in this thesis relies on an iterative procedure [137] solving a nonlinear operator equation.

Figure 5.6 shows the absolute values of the density matrices for the states  $|\uparrow\downarrow\rangle+|\downarrow\uparrow\rangle$  and  $|\downarrow\downarrow\rangle+|\uparrow\uparrow\rangle$  created in the experiment.

---

## 6. Entangling calcium ions

The most complicated operations needed for QIP in ion traps are universal multi-qubit operations. Most implementations so far lack the performance to carry out gate operations in series without producing too high errors. This chapter will describe experiments on entangling either a pair of  $^{40}\text{Ca}^+$  ions or a pair of  $^{43}\text{Ca}^+$  ions. The first section will focus on a high-fidelity entanglement of  $^{40}\text{Ca}^+$  ions cooled to the ground state and to thermal states of motion with  $\langle n \rangle \neq 0$ . The entanglement of three  $^{40}\text{Ca}^+$  ions by means of a MS interaction and the implementation of the first steps to do arbitrary quantum circuits on three ions will be discussed in the next section. The chapter will be concluded by the description of an experiment where the knowledge gained with  $^{40}\text{Ca}^+$  ions was transferred to the more complicated level structure of  $^{43}\text{Ca}^+$  and used to entangle a pair of  $^{43}\text{Ca}^+$  ions. Especially interesting is the mapping of the entanglement from the optical onto the hyperfine qubit.

### 6.1. High fidelity two ion Bell states

Recently the first application of a Mølmer-Sørensen gate operation to an optical qubit was demonstrated [40]. In this experiment Bell states with a so far unmatched fidelity of 0.993(1) were deterministically created. Here, a further investigation of this universal gate operation acting on optical qubits with an extended experimental analysis is presented. Particular emphasis is put on the compensation of AC-Stark shifts and amplitude pulse shaping to reach high fidelities without compromising the gate speed substantially. The gate characterization is extended further by investigating the fidelity decay for different input states after up to 21 individual operations. Possible error sources for the gate operation will be listed at the end.

Moreover, the first experiments demonstrating a universal entangling gate operating on Doppler-cooled ions are presented. For ions in a thermal state with  $\bar{n} = 18(2)$ , Bell states with a fidelity of 0.984(2) were obtained.

The ability to implement high fidelity multi-qubit operations on Doppler-cooled ions is of practical interest in ion trap quantum information processing as the implementation of quantum algorithms demands several techniques that do not conserve the ions' vibrational quantum state: (i) State detection of ancilla qubits as required by quantum error correction schemes [138] can excite the ion string to a thermal motional state close to the Doppler limit because of the interaction with the laser inducing the ions to fluoresce. (ii) Experiments with segmented trap structures where ion strings are split into smaller strings also tend to heat up the ions slightly [139]. Here, the availability of high-fidelity gate operations even for thermal states may provide a viable alternative to the technically involved re-cooling techniques using a different ion species [140, 141].

Note that all experiments, except the measurements shown in figure 6.4 demonstrating the high

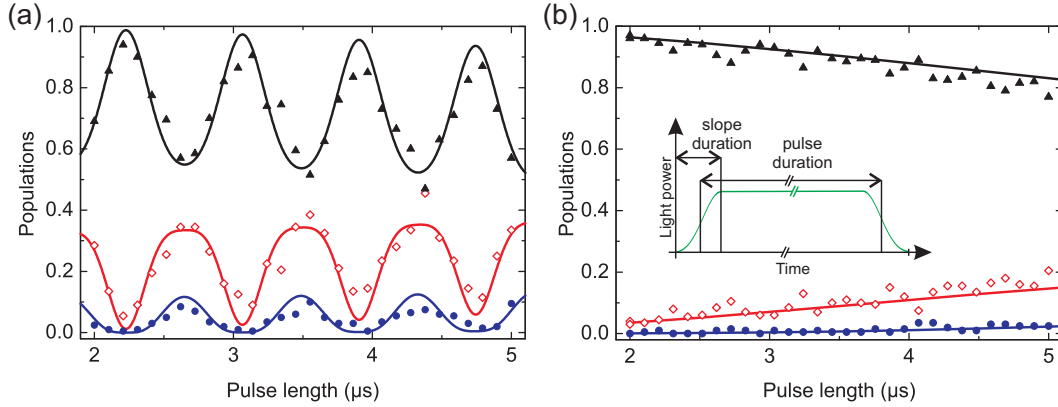


**Figure 6.1.:** Effect of amplitude pulse shaping on non-resonant population transfer caused by a bichromatic light field non-resonantly exciting the carrier transition. Experimental results are presented for a gate duration of  $t_{\text{gate}}=25 \mu\text{s}$ . A comparison of the evolution of the populations  $p_2$  ( $\blacktriangle$ ),  $p_1$  ( $\diamond$ ),  $p_0$  ( $\bullet$ ) for a square-shaped pulse (a) with an amplitude-shaped pulse (b) shows a suppression of the strong non-resonant oscillations for the latter case. The slopes are shaped as a Blackman window with a duration of  $2.5 \mu\text{s}$ , the figure inset showing the definitions of pulse and slope duration. Numerical simulations suggest that the actual pulse shape is not so important as long as the switching occurs sufficiently slowly. The solid lines are calculated from (3.34) and (3.29). To match experimental data and simulations, we allowed for a time offset  $\Delta t = 0.5 \mu\text{s}$  that accounts for the finite switching time of the AOM controlling the laser power.

fidelity gate on thermal ions, use the  $S_{1/2}, m_j = 1/2$  level together with the  $D_{5/2}, m_j = 5/2$  as a qubit instead of  $D_{5/2}, m_j = 3/2$ . The choice of the qubits was given by the beam geometry and the requirement of a high coupling strength (see chapter 3.3.1). The center of mass trap frequency for all experiments, except the measurements shown in figure 6.4 (c) (d), was set to  $\omega_{ax}/(2\pi) = 1.232 \text{ MHz}$  which corresponds to a Lamb-Dicke parameter  $\eta = 0.044$ . For the mentioned exception the trap frequency was slightly increased to  $\omega_{ax}/(2\pi) = 1.465 \text{ MHz}$  which corresponds to a Lamb-Dicke  $\eta = 0.04$ . The main findings of this chapter were also published in [76].

Two  $^{40}\text{Ca}^+$  ions were used to perform the experiments in this section. Doppler cooling and frequency-resolved optical pumping was applied to initialize the ions to  $|\downarrow\downarrow\rangle$ . Then the MS interaction is switched on and the appropriate parameters are varied to do the measurements.

### 6.1.1. Amplitude pulse shaping

The merits of amplitude pulse shaping were studied by observing the time evolution of the populations  $p_k$  at the beginning of the gate operation when the population transfer is dominated by fast non-resonant coupling to the carrier. For a better visibility of the effect the ions were cooled to the ground state. Figure 6.1 (a) shows the population evolution for the first  $5 \mu\text{s}$  of a  $25 \mu\text{s}$  gate operation based on a rectangular pulse shape. Averaging over a randomly varying phase  $\zeta^1$ , strong oscillations with a period of  $2\pi/\delta=0.84 \mu\text{s}$  were observed. The phase  $\zeta$ , defined in chapter 3.5, determines whether the gate operation starts in a maximum or a minimum of the intensity of

<sup>1</sup> $\zeta$  determines whether the gate operation starts in a maximum ( $\zeta = 0$ ) or a minimum ( $\zeta = \pi/2$ ) of the intensity of the amplitude-modulated beam (see chapter 3.5).

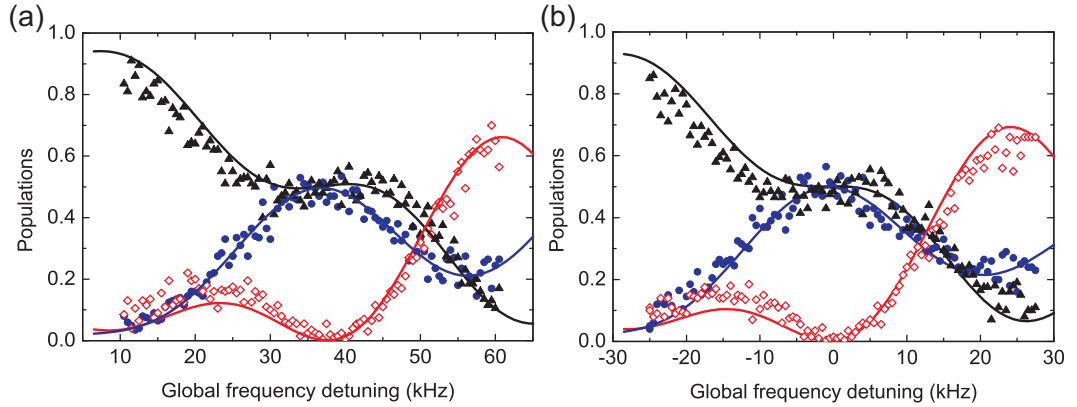


**Figure 6.2.:** (a) Populations  $p_0$  ( $\blacktriangle$ ),  $p_1$  ( $\diamond$ ),  $p_2$  ( $\bullet$ ) after a single gate operation ( $t_{\text{gate}}=25 \mu\text{s}$ ) where the global frequency detuning of the bichromatic entangling pulse is varied by scanning AO 2. A maximally entangled state is achieved for a global frequency detuning of  $(2\pi)$  37 kHz relative to the qubit transition frequency due to AC-Stark shifts. (b) Introduction of a beam imbalance  $\xi = 0.08$  shifts the pattern of the populations by the required amount to fully compensate for the AC-Stark-shift (note the different x-axis offsets in (a) and (b)). The solid lines are calculated by solving the Schrödinger equation for the Hamiltonian given in (3.27) amended by a term accounting for the measured AC-Stark shift.

the amplitude modulated beam. Panel (b) shows that the non-resonant excitations vanish completely after application of amplitude pulse shaping with a slope duration of  $2.5 \mu\text{s}$  corresponding to three vibrational periods of the center-of-mass mode. The slopes were shaped as a Blackman window [142], where the form of the shape is chosen such that a shaped and a rectangular pulse of the same duration have the same pulse area (see inset of panel (b)). Different pulse lengths are achieved by varying the duration of the central time interval during which the laser power is constant. The solid lines in the figure are calculated from (3.34) and (3.29).

### 6.1.2. AC-Stark shift compensation

The AC-Stark shift caused by bichromatic light with spectral components each having a Rabi frequency of  $\Omega/(2\pi)=220 \text{ kHz}$  (for  $t_{\text{gate}}=25\mu\text{s}$ ) is measured by scanning the global laser frequency using AO 2 (see figure 4.7). The resulting populations after a gate operation, again for ground state cooled ions, are depicted in figure 6.2 (a). We observe a drop of the population  $p_1$  to zero at a detuning of  $(2\pi)$  37 kHz from the carrier transition. At this setting the ions are maximally entangled. By changing the relative power of the bichromatic field's frequency components such that  $\xi = 0.08$  (see chapter 3.5.1) the AC-Stark shift is compensated. This translates the whole excitation pattern in frequency space as can be seen in figure 6.2 (b).

A more sensitive method to infer the remaining AC-Stark shift  $\delta_{AC}$  after a coarse pre-compensation consists in concatenating two gates separated by a waiting time  $\tau_w$  in a pulse sequence akin to a Ramsey-type experiment [143] and scanning  $\tau_w$ . This procedure maps  $\delta_{AC}$  to a phase  $\phi = \delta_{AC}\tau_w$  which is converted into a population change  $p_2 = \cos^2(\phi)$ ,  $p_0 = \sin^2(\phi)$  by the second gate pulse. For two ions, the corresponding Ramsey pattern displayed in figure 6.3 shows oscillations of the populations  $p_0$  and  $p_2$  with a frequency of two times the remaining AC-Stark shift.

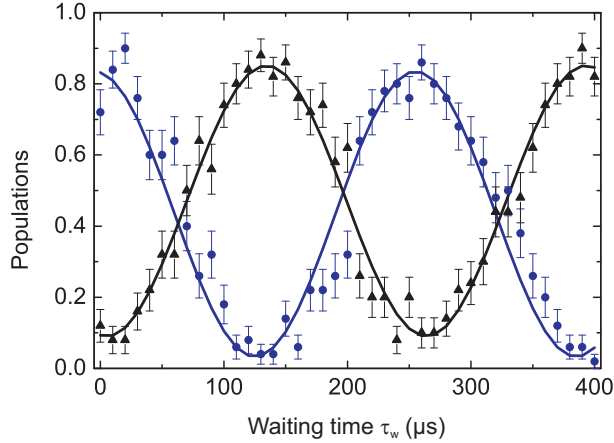


**Figure 6.3.:** Population evolution of  $|\uparrow\uparrow\rangle$  (●) and  $|\downarrow\downarrow\rangle$  (▲) when scanning the waiting time between two  $25 \mu\text{s}$  gate pulses in a Ramsey-like experiment. For this scan the detuning  $\epsilon$  was set to  $(2\pi) 40 \text{ kHz}$ . In this set of data, the AC-Stark shift was only partially compensated by imbalancing the power of the two frequency components. From the sinusoidal fits shown as solid lines, we infer an oscillation period of  $258(4) \mu\text{s}$  corresponding to a residual AC-Stark shift of  $(2\pi) 1.94(3) \text{ kHz}$ .

### 6.1.3. Gate analysis

A full characterization of the gate operation could be achieved by quantum process tomography [50]. At present, however, the errors introduced by the tomography pulse and individual qubit detection are on the few percent level in our experimental setup which renders the detection of small errors difficult in the entangling operation. Instead, the quality of the gate operation was characterized by using it for creating different Bell states and determining their fidelities.

For the Bell state  $\Psi_1 = |\downarrow\downarrow\rangle + i|\uparrow\uparrow\rangle$ , the fidelity is given by  $F = \langle \Psi_1 | \rho^{\text{exp}} | \Psi_1 \rangle = (\rho_{\uparrow\uparrow, \uparrow\uparrow}^{\text{exp}} + \rho_{\downarrow\downarrow, \downarrow\downarrow}^{\text{exp}})/2 + \text{Im}\rho_{\downarrow\downarrow, \uparrow\uparrow}^{\text{exp}}$ , with the density matrix  $\rho^{\text{exp}}$  describing the experimentally produced state. To determine  $F$ , the populations  $p_2 + p_0$  need to be measured at the end of the gate operation as well as the off-diagonal matrix-element  $\rho_{\downarrow\downarrow, \uparrow\uparrow}^{\text{exp}}$ . To determine the latter, a  $\pi/2$  pulse was applied to both ions with an optical phase  $\phi$  to measure  $\langle \sigma_z^{(1)} \sigma_z^{(2)} \rangle$  for the resulting state as a function of  $\phi$ . This procedure is equivalent to measuring oscillations of the expectation value  $\text{Tr}(P(\phi)\rho^{\text{exp}})$  of the parity operator  $P(\phi) = \sigma_\phi^{(1)} \sigma_\phi^{(2)}$  where  $\sigma_\phi = \sigma_x \cos \phi + \sigma_y \sin \phi$  (see figure 6.4 (b) and (d)). The amplitude  $A$  of these oscillations equals  $2|\rho_{\downarrow\downarrow, \uparrow\uparrow}^{\text{exp}}|$  and is obtained by fitting them with the function  $P_{\text{fit}}(\phi) = A \sin(2\phi + \phi_0)$ .

Measurements [40] using  $|\downarrow\downarrow\rangle$  as input state have demonstrated Bell state fidelities as high as  $0.993(1)$  (see figure 6.4 (a) and (b)) for gate times of  $50 \mu\text{s}$  or 61 trap oscillation periods. Figure 6.4 (a) illustrates the population evolution induced by the gate pulse for ground-state cooled ions initially prepared in the qubit states  $|\downarrow\downarrow\rangle$ . Figure 6.4 (b) displays parity oscillations for the produced Bell state. By doubling the detuning to  $\epsilon/(2\pi)=40 \text{ kHz}$  the gate duration is reduced to only 31 trap oscillation periods and Bell states with a fidelity of  $0.971(2)$  were observed which is remarkable considering the small Lamb-Dicke parameter of  $\eta = 0.044$ . The detrimental effects illustrated in figure 6.1 (a) are sufficiently suppressed by amplitude pulse shaping. While many theoretical papers discussing Mølmer-Sørensen and conditional phase gates put much emphasis on

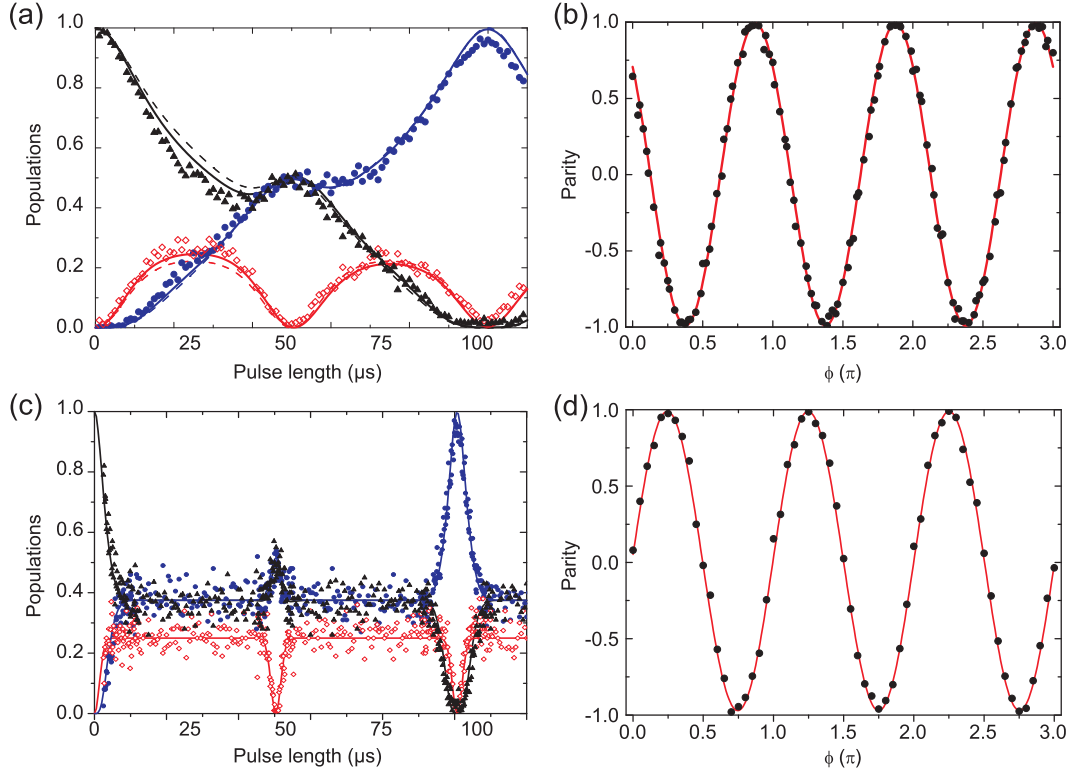


**Figure 6.4.:** Measured population evolution for  $p_0$  ( $\bullet$ ),  $p_1$  ( $\diamond$ ),  $p_2$  ( $\blacktriangle$ ) and parity oscillations with (a,b) and without (c,d) ground state cooling. In the latter case, population is transferred faster into  $|\uparrow\downarrow, n\rangle$ ,  $|\downarrow\uparrow, n\rangle$  as compared to sideband cooled ions due to the higher coupling strength to the sidebands. In (c), the solid lines are a fit to the data points using (3.36) with the mean phonon number  $\bar{n}$  as a free parameter giving  $\bar{n} = 18(2)$ . The parity oscillations for the ions in a thermal state of motion have an amplitude of  $0.980(2)$ . Combining this measurement with the independently determined populations  $p_2 + p_0 = 0.988(1)$  results in a Bell state fidelity of  $0.984(2)$ . The data appearing in (a) and (b) are taken from [40]. Here the deviation of the dashed lines from the data is caused by the AC-Stark shift compensation using  $\xi = 0.08$ . The dashed lines are calculated for  $\bar{n}_{\text{com}} = 0.05$  from the propagator (3.29), neglecting pulse shaping and non-resonant carrier excitation. The solid lines are obtained from numerically solving the Schrödinger equation for time-dependent  $\Omega(t)$  and imbalanced Rabi frequencies  $\xi = 0.08$ . The parity oscillations for the ground state cooled ions have an amplitude of  $0.990(1)$  which leads to a fidelity of  $0.993(1)$ . The amplitude of the parity oscillations was obtained by a fit with the function  $P(\phi) = A \cdot \sin(2\phi + \phi_0)$ . The value of the phase  $\phi_0$  is without significance. It arises from phase locking the frequencies  $\nu, \nu_+, \nu_-$  and could have been adjusted to zero.

the possibility of entangling ions irrespective of their motional state by using these gates, there has not been any experimental demonstration of this gate property up to now. The reason for this is that independence of the motional state, as predicted by (3.29), is achieved only deep within the Lamb-Dicke regime whereas experiments demonstrating entangling gates on hyperfine qubits usually have Lamb-Dicke factors on the order of  $\eta = 0.1-0.2$  [34, 109, 144]. Therefore, all previous experimental gate realizations used laser cooling to prepare at least the motional mode mediating the gate in its ground state with  $n = 0$ .

The corresponding time evolution and parity oscillations for ions that are merely Doppler-cooled to a thermal state are shown in figure 6.4 (c) and (d) respectively. As the coupling strengths on the upper and lower motional sidebands scale as  $\propto \sqrt{n+1}$  and  $\propto \sqrt{n}$ , non-resonant sideband excitation transfers population much faster from  $|\downarrow\downarrow, n\rangle$  into  $|\downarrow\uparrow, n \pm 1\rangle$ ,  $|\uparrow\downarrow, n \pm 1\rangle$  as compared to the case of ions prepared in the ground state with  $\bar{n} = 0$ . After the gate time  $t_{\text{gate}}=50 \mu\text{s}$ , however, the undesired population  $p_1$  nearly vanishes as in the case of ground-state cooled ions and the Bell state  $\Psi_1$  is again created. In the experiment, we find a population  $p_1 = 0.012(1)$  in the undesired energy eigenstates. The parity oscillations have an amplitude of  $0.980(2)$ , resulting in a Bell state fidelity of  $0.984(2)$ . The reasons for the somewhat reduced fidelity as compared to ground-state cooled ions are only partially understood. In part, the fidelity loss arises from a variation of the coupling strength on the vibrational sidebands as a function of  $n$  caused by higher-order terms in  $\eta$ . Fitting equations (3.36) to the population evolution data allows us to determine the mean vibrational quantum number as  $\bar{n} = 18(2)$ . This value is consistent with independent measurements obtained by comparing the time evolution of the ions when exciting them on the carrier and on the blue motional sideband. For a thermal state with  $\bar{n} = 18$  and  $\eta = 0.04$  calculations show that this effect amounts to additional errors of  $5.5 \times 10^{-3}$ , which makes up for most of the difference.<sup>2</sup>

The amplitude of the parity oscillations was obtained by a fit with the function  $P(\phi) = A \cdot \sin(2\phi + \phi_0)$ . The value of the phase  $\phi_0$  is without significance. It arises from phase locking the frequencies  $\nu, \nu_+, \nu_-$  and could have been adjusted to zero by changing the phase of the signal generators producing  $\nu_+$  and  $\nu_-$ .

As mentioned in Section 3.5.1, the AC-Stark compensation by unbalancing the power of the red and blue frequency component is not applicable to ions in a thermal state. Instead, the laser frequency needs to be adjusted to account for AC-Stark shifts  $\delta_{\text{AC}}$ , a technique that works well as long as the AC-Stark shifts are smaller than the coupling strength  $\lambda$  of the gate interaction appearing in (3.30) (otherwise, in the case  $\delta_{\text{AC}} \gg \lambda$ , small laser power fluctuations give rise to large phase shifts). Therefore, care must be taken to choose the direction and polarization of the gate laser such that a favorable ratio  $\lambda/\delta_{\text{AC}}$  is obtained. In experiments with a gate duration of  $t_{\text{gate}}=50 \mu\text{s}$  on the transition  $S_{1/2}, m_j = 1/2 \rightarrow D_{5/2}, m_j = 5/2$ , we achieved  $\lambda/\delta_{\text{AC}} \approx 3$  and needed to shift the laser frequency by about 7.5 kHz for optimal Bell state fidelity. In the experiments shown in figure 6.4, a further reduction of the AC-Stark shift could be obtained by using a  $\sigma^+$ -polarized laser beam incident on the ions along the direction of the magnetic field. In this geometry the AC-Stark shift is predominantly caused by the  $S_{1/2} \leftrightarrow P_{3/2}$  dipole transition

<sup>2</sup>The loss of fidelity due to coupling strength fluctuations is given by  $1 - F = (\pi/2)^2(\delta\Omega/\Omega)^2$ . The expectation value for  $\delta\Omega/\Omega$  can be estimated by assuming a thermal state distribution and a coupling strength that depends on  $n$  in first order as  $\Omega = 1 - \eta^2 n$ .

## 6.1 High fidelity two ion Bell states

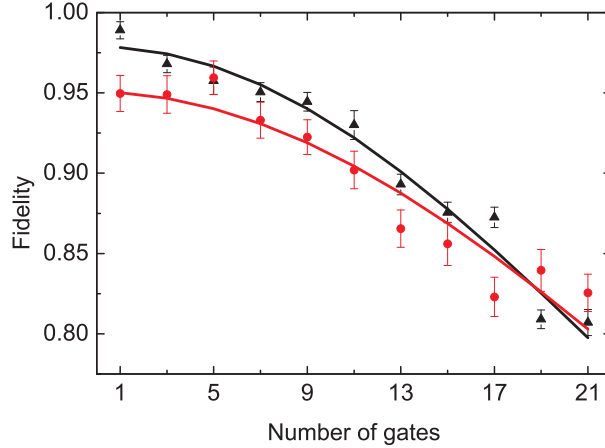


**Figure 6.5.:** Bell state fidelities after  $n$  gate operations applied to the input states  $|\downarrow\downarrow\rangle$ (▲) and  $|\downarrow\uparrow\rangle$ (●) for  $t_{\text{gate}} = 50\mu\text{s}$ . Taking into account the error for state preparation of the input states  $|\downarrow\uparrow\rangle$  and a similar error to measure the parity signal, we conclude that the gate operation works on all tested input states similarly well. The solid lines reflect a Gaussian decay of the parity fringe amplitudes as a function of the number of gates and a linear decay in the desired populations caused by the spectral impurity of the laser. For both input states the gate operation implies errors of less than 0.2 after 21 consecutive applications.

since the  $D_{5/2}, m_j = +3/2$  state does not couple to any of the 4p Zeeman states. Measurements show that the shift is reduced to about 1.8 kHz without compromising the gate speed.

### 6.1.4. Different input states and multiple gate operations

For a gate time of 50  $\mu\text{s}$  the analysis was extended by applying the gate to the state  $|\downarrow\uparrow\rangle$  which is prepared by a  $\pi/2$  rotation (beam 2) of both ions, followed by a  $\pi$  phase-shift pulse on a single ion performed with the far-detuned focused beam (as explained in chapter 5.4), and another  $\pi/2$  rotation applied to both ions. This pulse sequence realizes the mapping

$$|\downarrow\downarrow\rangle \longrightarrow |\downarrow + \uparrow\rangle|\downarrow + \uparrow\rangle \longrightarrow |\downarrow - \uparrow\rangle|\downarrow + \uparrow\rangle \longrightarrow |\downarrow\uparrow\rangle \quad (6.1)$$

to the desired input state for the gate. Imperfections of single-ion addressing led to an error in state preparation of 0.036(3) (Addressing was improved after these experiments had been performed to the values stated in chapter 5.4). For the Bell state analysis, the population  $p_1$  was measured to infer  $\rho_{\uparrow\downarrow,\uparrow\downarrow}^{\text{exp}} + \rho_{\downarrow\uparrow,\downarrow\uparrow}^{\text{exp}}$ . Unfortunately parity oscillations cannot be introduced by a collective  $\pi/2$  pulse acting on the state  $|\uparrow\downarrow\rangle + i|\downarrow\uparrow\rangle$ . Instead, this state was transferred into  $|\uparrow\uparrow\rangle + i|\downarrow\downarrow\rangle$  by repeating the steps of sequence (6.1) as for the state preparation. The coherence was measured again by performing parity oscillations.

Figure 6.5 shows a comparison of the fidelity of the gate starting either in  $|\downarrow\downarrow\rangle$  or  $|\downarrow\uparrow\rangle$ . The fidelity of a Bell state created by a single gate starting in  $|\downarrow\uparrow\rangle$  is 0.95(1). Taking into account the errors for state preparation and the Bell state analysis we conclude that the entangling operation works equally well for  $|\downarrow\uparrow\rangle$  as an input state. This hypothesis is supported by the observation that for both states we obtain a similar decay of Bell state fidelities with increasing gate number. The

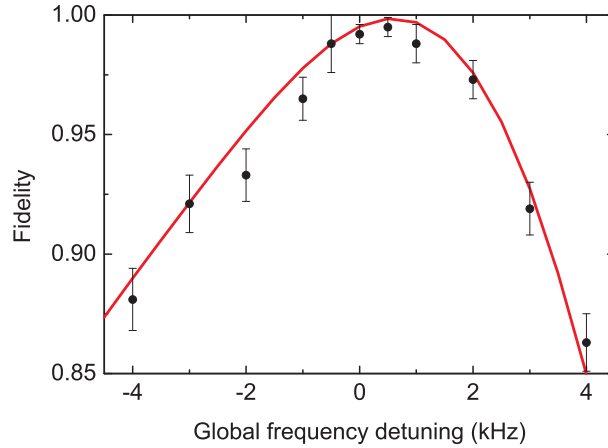


**Figure 6.6.:** Fidelity as a function of the global frequency detuning of the bichromatic light pulse from the carrier transition (here, the sideband detuning was set to  $\epsilon/(2\pi)=20$  kHz). A maximum fidelity of 0.995(4) was found for a detuning of 500 Hz from the transition center due to a residual AC-Stark shift. The solid line is obtained by numerically solving equation (3.27) and taking into account the AC-Stark shift compensation by different powers of the blue and the red laser frequency component. At the maximum the solid line experiences a second order frequency dependence of  $-9.6(3) \times 10^{-9} \text{ Hz}^2$ .

application of  $N$  gate operations maps the input state  $|\downarrow\downarrow\rangle$  to

$$|\downarrow\downarrow\rangle \longrightarrow |\downarrow\downarrow\rangle + i|\uparrow\uparrow\rangle \longrightarrow |\uparrow\uparrow\rangle \longrightarrow |\downarrow\downarrow\rangle + i|\uparrow\uparrow\rangle \longrightarrow |\uparrow\uparrow\rangle \longrightarrow \dots$$

and the state  $|\downarrow\uparrow\rangle$  to

$$|\downarrow\uparrow\rangle \longrightarrow |\downarrow\uparrow\rangle - i|\uparrow\downarrow\rangle \longrightarrow |\uparrow\downarrow\rangle \longrightarrow |\downarrow\uparrow\rangle - i|\uparrow\downarrow\rangle \longrightarrow |\downarrow\uparrow\rangle \longrightarrow \dots$$

Compared with earlier results [40] where multiple gate operations were induced by varying the duration of a single bichromatic pulse, here up to 21 individual amplitude-shaped pulses were applied. Splitting up a long pulse into many shorter gate pulses has no detectable effect on the fidelity of the Bell states produced, and in both cases we obtain a Bell state fidelity larger than 0.80 after 21 gates.

### 6.1.5. Gate errors

From the preceding measurements the following error sources can be determined and quantified (see also [40, 76]).

- A bichromatic force with time-dependent  $\Omega(t)$  acting on ions prepared in an eigenstate of  $S_y$  creates coherent states  $\alpha(t)$  following trajectories in phase space that generally do not close [145, 146]. For the short rise times used in our experiments, this effect can be made negligibly ( $< 10^{-4}$ ) small by slightly increasing the gate time.
- Spin flips induced by incoherent off-resonant light of the bichromatic laser field reduce the gate fidelity. The spectrum of the laser determined by a beat measurement (see figure 4.8(b))

## 6.1 High fidelity two ion Bell states

---

shows that a fraction  $\gamma$  of about  $2 \cdot 10^{-7}$  of the total laser power is contained in a 20 kHz bandwidth  $B$  around the carrier transition when the laser is tuned close to a motional sideband. A simple model predicts spin flips to cause a gate error with probability  $p_{flip} = (\pi\gamma|\epsilon|)/(2\eta^2 B)$ . This would correspond to a probability  $p_{flip} = 8 \cdot 10^{-4}$  whereas the state populations measured for figure 6.5 are consistent with  $p_{flip} = 2 \cdot 10^{-3}$ . Spin flip errors could be further reduced by two orders of magnitude by spectrally filtering the laser light and increasing the trap frequency  $\omega/(2\pi)$  to above 2 MHz where noise caused by the laser frequency stabilization is much reduced.

- Imperfections due to low frequency noise randomly shifting the laser frequency  $\nu_L$  with respect to the atomic transition frequency  $\nu$  were estimated from Ramsey measurements on a single ion showing that an average frequency deviation  $\Delta_{(\nu_L-\nu)}/(2\pi) = 160$  Hz occurred. From numerical simulations, one can infer that for a single gate operation this frequency uncertainty gives rise to a fidelity loss of 0.25% (an infidelity of  $10^{-4}$  would require  $\Delta_{(\nu_L-\nu)}/(2\pi) = 30$  Hz). In the parity oscillation experiments shown in figures 6.4 and 6.5, however, this loss is not directly observable since a small error in the frequency of the bichromatic laser beam carrying out the gate operation is correlated with a similar frequency error of the carrier  $(\frac{\pi}{2})_\phi$  pulse probing the entanglement produced by the gate so that the phase  $\phi$  of the analysing pulse with respect to the qubit state remains well defined.
- Variations in the coupling strength  $\delta\Omega$  induced by low-frequency laser intensity noise and thermally occupied radial modes were inferred from an independent measurement by recording the amplitude decay of carrier oscillations. Assuming a Gaussian decay, a relative variation of  $\delta\Omega/\Omega = 1.4(1) \cdot 10^{-2}$  is found. For  $m$  entangling gate operations, the loss of fidelity is approximately given by  $1 - F = (\frac{\pi m}{2})^2 (\delta\Omega/\Omega)^2$  and contributes with  $5 \cdot 10^{-4}$  to the error of a single gate operation. For the multiple gate operations shown in figure (6.5), this source of noise explains the Gaussian decay of fidelity whereas laser frequency noise reduces the fringe amplitude by less than 1% even for 21 gate operations. In combination with error estimates for state preparation, detection and laser noise, the analysis of multiple gates provides us with a good understanding of the most important sources of gate infidelity.
- An error that was not investigated in [40] is the dependence of the Bell state fidelity on the global laser frequency detuning from the qubit transition frequency. Experimental results are shown in figure 6.6. The solid line fitting the data is calculated by numerically solving the full Schrödinger equation for different global frequency detunings and evaluating the fidelity. A second order frequency dependence of  $-9.6(3) \times 10^{-9} Hz^2$  is found from calculations at the maximum point. This suggests that our laser's typical mean frequency deviation of 160 Hz contributes with  $3 \times 10^{-4}$  to the error budget.
- A further error source arises when the bichromatic beam couples to both ions with different strengths. By recording Rabi oscillations simultaneously on the two ions we conclude that both ions experience the same coupling strength  $\Omega$  to within 4%. From numerical calculations we infer an additional error in the measured Bell state fidelity of less than  $1 \times 10^{-4}$ .
- Another possible error source is heating of the COM-mode during the gate operation since

the gate is not insensitive to motional heating in the parameter regime of our implementation. Using the calculation performed in [81], we find a fidelity reduction of  $\Delta F = \Gamma_h t_{\text{gate}}/2$  where  $\Gamma_h$  is the heating rate of the COM-mode. As in our experiments  $\Gamma_h = 3s^{-1}$ , the fidelity is reduced by  $\Delta F \approx 10^{-4}$  for  $t_{\text{gate}}=50 \mu\text{s}$ .

### 6.1.6. Conclusion

Until recently, entangling gates for optical qubits were exclusively of the Cirac-Zoller type which require individual addressing of the ions. Compared to this type of gate the Mølmer-Sørensen gate gives an improvement in fidelity and speed of nearly an order of magnitude. The achieved fidelity sets a record for creating two-qubit entanglement on demand irrespective of the physical realization considered so far. The results with concatenations of 21 of these operations bring the realization of more complex algorithms a step closer to reality. The implementation of a gate without the need for ground state cooling is of particular interest in view of quantum algorithms that require entangling gates conditioned on quantum state measurements that do not preserve the ions' motional quantum state.

When considering gate imperfections, two regimes are of interest: On the one hand, in view of a future implementation of fault-tolerant gate operations, it is important to investigate whether the gate operation allows in principle for gate errors on the order of  $10^{-4}$  or below. On the other hand, for current experiments aiming at demonstrating certain aspects of quantum information processing, errors on the order of  $10^{-2}$  are not forbiddingly high. For these experiments, the prospect of carrying out a gate operation using ions that are not in the vibrational ground state of the mode mediating the internal-state entanglement, is appealing as it might allow to perform entangling gates after having split a long ion string into shorter segments (the splitting process has been demonstrated to heat up the ions by no more than a single quantum of motion [42]). Similarly, quantum state detection by light scattering on a cycling transition heats up the vibrational mode. However, if done properly, the final mean quantum number stays well below the average of 20 quanta for which we demonstrated entanglement generation. Therefore, experiments involving gates after splitting and detection operations might profit from a quantum gate as demonstrated in chapter 6.1.

For future ion trap experiments in the fault-tolerant domain, the needs are going to be different. Here, ground state laser cooling will most likely be indispensable to achieve the highest fidelity possible. Also AC-Stark compensation based on imbalanced bichromatic beam intensities should be avoided as the technique tends to complicate the gate Hamiltonian and to introduce small additional errors. Even though the current experiments are still limited by technical imperfections, simulations predict that in principle it should be possible to achieve gate errors of  $10^{-4}$  or below with a Mølmer-Sørensen gate on a quadrupole transition. Gates with ions in motional states are important in this context as no experiment will cool the ions to the ground state  $n = 0$  perfectly (in current experiments, the ground state is typically occupied with a success rate of 90 to 99%). Our simulations indicate that for ions in  $n = 1$ , gate errors could still be as small as  $2 \cdot 10^{-4}$  so that gate errors of  $10^{-4}$  or below seem feasible even without perfect initialization of the motional mode.

The optical qubit as used here is certainly not the best solution for long time storage of quantum

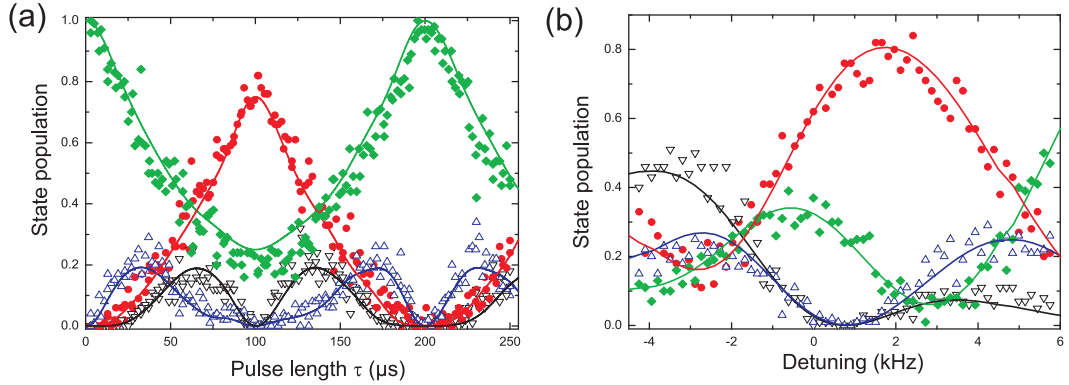


**Figure 6.7.:** (a) Evolution of the populations of three ions  $p_0(\nabla)$ ,  $p_1(\bullet)$ ,  $p_2(\triangle)$  and  $p_3(\blacklozenge)$  induced by a Mølmer-Sørensen interaction of pulse length  $\tau$ . Pulse shaping is used to suppress off-resonant excitations. At  $100 \mu\text{s}$  the maximally entangled state  $|\downarrow\downarrow\downarrow\rangle - |\downarrow\uparrow\uparrow\rangle - |\uparrow\downarrow\uparrow\rangle - |\uparrow\uparrow\downarrow\rangle$  is created. The solid lines are calculated from the propagator (3.29). (b) Populations  $p_0(\nabla)$ ,  $p_1(\bullet)$ ,  $p_2(\triangle)$  and  $p_3(\blacklozenge)$  after a single gate operation ( $t_{\text{gate}}=100 \mu\text{s}$ ) where the global frequency detuning of the bichromatic entangling pulse is varied by scanning AO 2. A maximally entangled state is achieved at a detuning of 700 Hz relative to the qubit transition frequency due to uncompensated AC-Stark shifts. The solid lines are calculated by solving the Schrödinger equation for the Hamiltonian given in (3.27) amended by a term accounting for the measured AC-Stark shift.

information. Instead, qubits encoded in two hyperfine ground states whose frequency difference is insensitive to changes in magnetic field are preferable. These magnetic-field insensitive hyperfine qubits can store quantum information for times exceeding the duration of the gate operation presented here by more than four orders of magnitude [102, 147, 148]. However, on such qubit states no high-fidelity universal gates have been demonstrated so far. By mapping between the hyperfine qubit encoded in the ion's ground states and the optical qubit we will benefit from both of their advantages (see chapter 6.3).

## 6.2. Three ion entangled states and arbitrary operations on three qubits

After entangling two ions with a MS interaction the next obvious step is to entangle more ions. Unfortunately in the current setup we are not able to reliably trap more than three ions in a crystal-like structure with reasonable trapping parameters. The issue is not yet clear, but most likely this is due to a high collision rate of the ions with background gas particles. An indication for this is, that on average every 4 h an ion in a crystal becomes dark due to a chemical reaction with the background gas. Measurements of the axial oscillation frequency of a two ion crystal with one dark ion indicated that an OH group attached itself to a dark ion. As we are not able to trap more than four or more ions the experiments presented in this chapter only deal with entangling three ions. The results are very similar to the ones recently published by Chris Monroe's group [149]. The difference is that in this thesis the qubit is an optical one and a single axial oscillator mode is used for mediating the coupling.

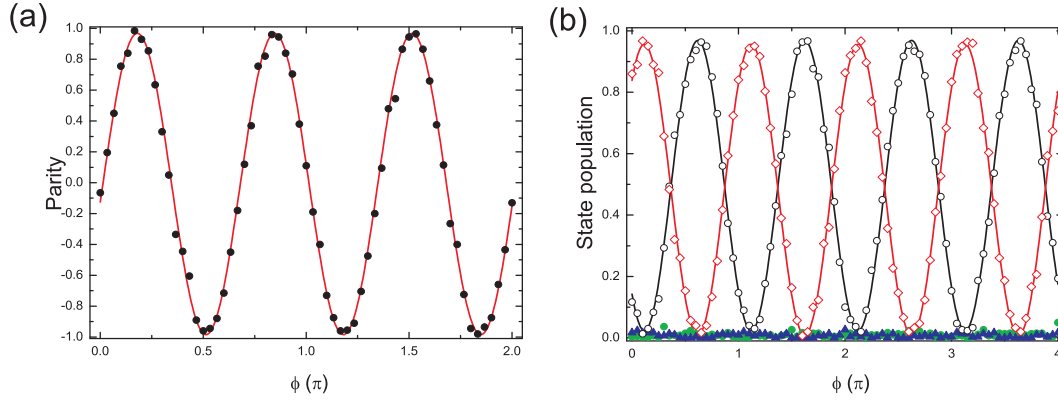


**Figure 6.8.:** (a) A  $(\frac{\pi}{2})_{(-y)}$  pulse applied to all ions maps the three ion entangled state  $|\downarrow\downarrow\downarrow\rangle - |\downarrow\uparrow\uparrow\rangle - |\uparrow\downarrow\uparrow\rangle - |\uparrow\uparrow\downarrow\rangle$  onto the GHZ state  $|\downarrow\downarrow\downarrow\rangle + i|\uparrow\uparrow\uparrow\rangle$ . A second  $(\frac{\pi}{2})_{\phi}$  analysis pulse again applied to all ions gives rise to parity oscillations  $P(\phi) = A \cdot \sin(3\phi)$  as a function of  $\phi$ . The obvious difference to parity flops with two ions is the different period, three oscillations occurring for  $\phi$  changing from 0 to  $2\pi$ . A fit with the function  $P(\phi) = A \cdot \sin(3\phi + \phi_0)$  yields the parity fringe amplitude  $A = 0.977(2)$ . The value of the phase  $\phi_0$  is without significance. Together with the independently measured populations  $p_1 + p_2 = 0.0189(1)$  this leads to a GHZ state fidelity of  $0.979(2)$ . (b) Parity like oscillations of the states  $(|\uparrow\uparrow\rangle_{1,2} + i|\downarrow\downarrow\rangle_{1,2}) \otimes |\downarrow\rangle_3$  (o) and  $(|\uparrow\downarrow\rangle_{1,2} + |\downarrow\uparrow\rangle_{1,2}) \otimes |\downarrow\rangle_3$  (◇) created by entangling two out of three ions. The analysis  $(\frac{\pi}{2})_{\phi}$  pulse was applied to two ions and the state evolution was analyzed with the camera. The addressing of all operations on two ions is clearly visible in the states  $|\uparrow\uparrow\rangle_{1,2} \otimes |\uparrow\rangle_3, i|\downarrow\downarrow\rangle_{1,2} \otimes |\uparrow\rangle_3$  (combined in ●) and  $|\uparrow\downarrow\rangle_{1,2} \otimes |\uparrow\rangle_3, |\downarrow\uparrow\rangle_{1,2} \otimes |\uparrow\rangle_3$  (combined in ▲) as they show no oscillatory behavior and are not populated. From these data one can infer a state fidelity of  $0.958(2)$  for entangling two ions and leaving the third one untouched.

### 6.2.1. A three ion Mølmer-Sørensen gate

Three  $^{40}\text{Ca}^+$  ions were loaded into the linear trap. After Doppler cooling and frequency-resolved optical pumping, the axial center of mass mode is cooled close to the motional ground state. The ions are now initialized to  $|\downarrow\downarrow\downarrow\rangle$ . Then, the gate operation is performed with beam 1 (see figure 5.4)(a) and the probabilities  $p_k$  of finding  $k$  ions in the state  $|\downarrow\rangle$  are measured for a varying pulse duration. A Rabi frequency of  $\Omega/(2\pi) \approx 70$  kHz is required for performing a gate operation with  $\epsilon/(2\pi) = 10$  kHz and a three-ion Lamb Dicke parameter of  $\eta = 0.036$ . To make the bichromatic laser pulses independent of the phase  $\zeta$ , the pulse is switched on and off by using pulse slopes of  $2 \mu\text{s}$  duration.

The time evolution of the three-ion state populations  $p_k$  are shown in figure 6.7 (a). After a gate time of  $t_{\text{gate}} = 100 \mu\text{s}$  the undesired populations  $p_0$  and  $p_2$  nearly vanish and the state  $|\downarrow\downarrow\downarrow\rangle - |\downarrow\uparrow\uparrow\rangle - |\uparrow\downarrow\uparrow\rangle - |\uparrow\uparrow\downarrow\rangle$  is created. In the experiment, we find a population  $p_0 + p_2 = 0.0189(1)$  in the undesired energy eigenstates. Contrary to the two ion case, an application of two times the gate does not flip the state of all qubits but rather returns all populations to the initial state.

The AC-Stark shift caused by the bichromatic light is not compensated. A scan of the global laser frequency reveals a vanishing of the undesired populations  $p_0 + p_2$  at 700 Hz detuning relative to the carrier transition. The resulting frequency dependence of the populations after a gate operation are depicted in figure 6.7 (b).

## 6.2 Three ion entangled states and arbitrary operations on three qubits

For the state  $\Psi_1 = |\downarrow\downarrow\downarrow\rangle - |\downarrow\uparrow\uparrow\rangle - |\uparrow\downarrow\uparrow\rangle - |\uparrow\uparrow\downarrow\rangle$ , the fidelity is not directly observable with parity oscillations. First a  $U_x(\frac{\pi}{2})$  pulse is applied to all ions mapping the entangled state  $|\downarrow\downarrow\downarrow\rangle - |\downarrow\uparrow\uparrow\rangle - |\uparrow\downarrow\uparrow\rangle - |\uparrow\uparrow\downarrow\rangle$  onto the GHZ state  $|\downarrow\downarrow\downarrow\rangle - i|\uparrow\uparrow\uparrow\rangle$ . A second  $U(\frac{\pi}{2}, \phi)$  analysis pulse again applied to all ions gives rise to parity oscillations  $P(\phi) = A \cdot \sin(3\phi)$  as a function of  $\phi$  (see figure 6.8 (a)). The obvious difference to parity flops with two ions is the different period, three oscillations occurring for  $\phi$  changing from 0 to  $2\pi$ . A fit with the function  $P(\phi) = A \cdot \sin(3\phi + \phi_0)$  yields the parity fringe amplitude  $A = 0.977(2)$ . Combining this measurement with the previously measured state populations a fidelity of 0.979(2) is obtained for  $\Psi_1$ .

### 6.2.2. Entangling two out of three ions

The goal for all QIP experiments is to implement arbitrary quantum circuits. Here a first step towards that direction is presented by combining a global MS-interaction with addressed  $\sigma_z$  rotations and global carrier pulses as described in chapter 5.4.

The most important operation is to implement the pulse sequence shown in figure 5.4(c). This pulses sequence effectively switches off the interaction between one ion and the other two. After the application of these pulses we end up in the state  $\Psi_2 = (|\uparrow\uparrow\rangle_{1,2} + i|\downarrow\downarrow\rangle_{1,2}) \otimes |\downarrow\rangle_3$  where the subscript denotes the ion. To analyze the fidelity of this state we again apply a  $(\frac{\pi}{2})_\phi$  pulse to the two entangled ions by using the same principle. All ions are first rotated by  $(\frac{\pi}{4})_\phi$ , then ion 1 experiences a  $\pi$  phase shift by an AC-stark pulse. The second  $(\frac{\pi}{4})_\phi$  pulse rotates ion 2 and 3 by the desired angle and returns ion 1 to the initial state. This pulse sequence induces parity-like oscillations between the states  $\Psi_2$  and  $(|\uparrow\downarrow\rangle_{1,2} + |\downarrow\uparrow\rangle_{1,2}) \otimes |\downarrow\rangle_3$ . The state of the ions was detected with the help of the camera and the recorded oscillations are shown in figure 6.8. The addressing of all operations on two ions is clearly visible in the evolution of the states  $|\uparrow\uparrow\rangle_{1,2} \otimes |\uparrow\rangle_3, |\downarrow\downarrow\rangle_{1,2} \otimes |\uparrow\rangle_3$  and  $|\uparrow\downarrow\rangle_{1,2} \otimes |\uparrow\rangle_3, |\downarrow\uparrow\rangle_{1,2} \otimes |\uparrow\rangle_3$ . These states are not populated, thus they effectively did not participate in any of the operations. From these data combined with the independently measured population one can infer a state fidelity of 0.958(2) for the state  $\Psi_2$ .

Realizing this pulse sequence opens up the possibility for more complicated sequences as all the necessary building blocks have been demonstrated. Recent experiments published by the group of David Wineland demonstrated a different approach to implement arbitrary quantum circuits [55, 56]. They “designed“ their interactions by moving the ions in a segmented trap and re-cooling them with a different ion species.

One particularly interesting algorithm is the one for correcting phase errors on a single qubit as shown in figure 6.9. The first MS gate encodes qubit 1 in a three ion state that is protected against phase errors. After the error occurred, the following pulses detect and correct for the error. After the operation only ion 1 is in the corrected state, ion 2 and 3 are in some arbitrary state. Ion 1 can be again protected by resetting ion 2 and 3 to  $|\downarrow\downarrow\rangle$  and applying another entangling pulse. The phase errors that can be corrected are either a phase flip on one ion or small phase errors on all of them, e.g. a  $\pi/10$  phase error on all of them is corrected in more than 99.8% of the cases assuming perfect operations. In this sequence one can identify a building block very similar to the one entangling two out of three ions. Meanwhile experiments have been performed implementing this algorithm and will be published soon. Similar algorithms using the same NMR-like techniques and building blocks were investigated by Volckmar Nebendahl in his thesis [150]. The sequence for

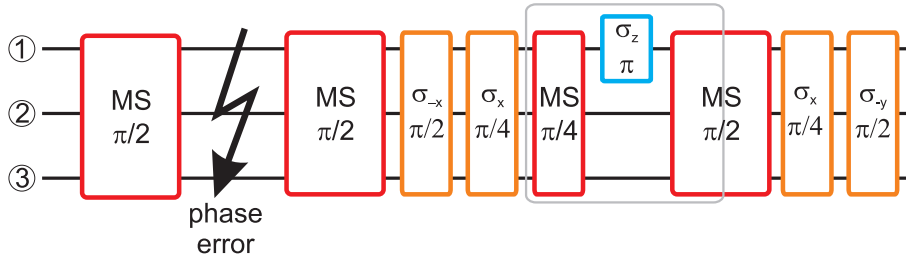


**Figure 6.9.:** Error correction sequence for three ions. The first MS gate encodes qubit 1 in a three ion state. After this encoding a phase error can occur and the subsequent pulses detect and correct for it. After the operation only ion 1 is in the corrected state, ion 2 and 3 are in some arbitrary state. Ion 1 can be again protected against phase errors by resetting ion 2 and 3 to  $|\downarrow\downarrow\rangle$  and applying another entangling pulse. The phase errors that can be corrected are either a phase flip on one ion or smaller phase errors on all of them. The grey box corresponds to the block already implemented, entangling two out of three ions.

the error correction code shown here and multi qubit gates like a Toffoli gate [151] can be found in his thesis.

### 6.3. High fidelity entanglement of $^{43}\text{Ca}^+$ hyperfine clock states

In experiments with trapped ions most of the elementary building blocks for quantum information processing have been demonstrated. State initialization, long quantum information storage times, entangling gates and readout have been realized with high fidelity [40, 109, 147, 148, 152, 153]. A major challenge in current experiments is to integrate these building blocks into a single setup and make them work for a given ion species and parameter range set by the trap frequencies, the magnetic field strength and further parameters. Quantum information encoded in ground state atomic levels whose energy difference only weakly depends on changes of the magnetic field (“clock” states) has been stored for more than a second [147, 148, 154, 155].

Most high fidelity entangling operations have been demonstrated on qubits with limited coherence times [102, 109]. One exception is the entanglement of hyperfine clock states in a  $\text{Yb}^+$  system demonstrated by Kim *et al.* [149].

An attractive way of combining high fidelity entangling gates with long storage times is to coherently map the quantum information from clock states to atomic states which are suitable for performing the entangling operation with high fidelity, and to map the information back at the end of the entangling operation [147]. In case this mapping operation is addressed at individual ions - for instance by using a strongly focused laser - the entanglement operation can be applied to the entire ion string.

The coherence time of the optical qubit used for entangling the ions is limited by magnetic field fluctuations, laser linewidth and ultimately the 1.2 s lifetime of the  $D_{5/2}$  state. For the most abundant isotope  $^{40}\text{Ca}^+$ , encoding the qubit in long-lived hyperfine clock states is impossible as this isotope has a nuclear spin  $I = 0$ . In the isotope  $^{43}\text{Ca}^+$  on the other hand where  $I = 7/2$ , coherence times of many seconds have been measured for qubits encoded in the  $S_{1/2}(F = 4, m_F = 0)$  and  $S_{1/2}(F = 3, m_F = 0)$  states [154, 155].

### 6.3 High fidelity entanglement of $^{43}\text{Ca}^+$ hyperfine clock states

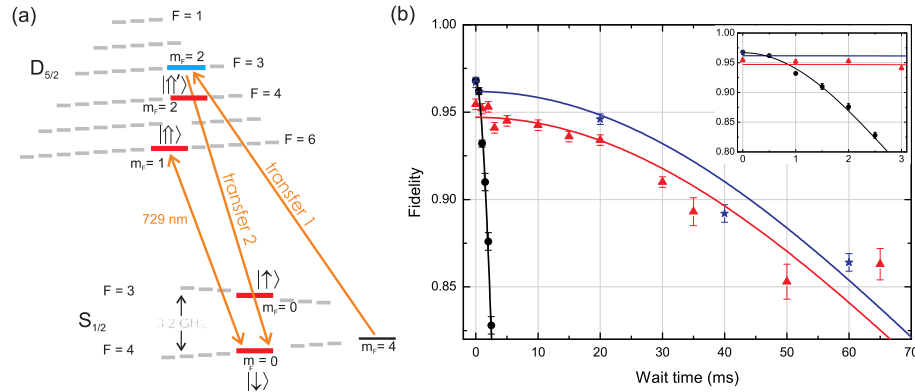


**Figure 6.10.:** (a) Energy levels of  $^{43}\text{Ca}^+$  showing the hyperfine splitting of the atomic states  $S_{1/2}$  and  $D_{5/2}$ . Microwave radiation applied to an electrode close to the ions drives the hyperfine qubit encoded in the states  $|↓\rangle$  and  $|↑\rangle$ . A laser at 729 nm excites the ions on the transition from the  $S_{1/2}(F=4)$  to the  $D_{5/2}(F=2, \dots, 6)$ -states. It is used for ground state cooling, state initialization, state discrimination and to excite the optical qubit comprised of the states  $|↓\rangle$  and  $|↑\rangle$  or  $|↑'\rangle$ . (b) Using a bichromatic laser beam, two  $^{43}\text{Ca}^+$  ions are entangled on an optical transition with a maximum target state fidelity of 96.9(3)% at a magnetic field of 6 G. By introducing a waiting time between the creation and the analysis of the Bell state we observe a Gaussian decay of the Bell state fidelity ( $\bullet$ ) (black solid line). Data for the first 3 ms are displayed as inset. When the optical qubit is mapped to the hyperfine qubit subsequent to the gate operation we obtain a maximum Bell state fidelity of 96.7(3)% and the lifetime of the entanglement increases to 96(3) ms ( $\star$ ). Measurements taken at a magnetic field of 3.4 G give similar results ( $\blacktriangle$ ) for the coherence time. Here, the optical qubit  $|↓\rangle \leftrightarrow D_{5/2}(F=4, m_F=2)$  in combination with the laser beam 3 was used for entangling the ions. Each data point represents 18.000 to 24.000 individual measurements.

In this chapter a combination of the long quantum information storage times observed for the hyperfine qubit of a single  $^{43}\text{Ca}^+$  ion with the high fidelity gate operation on optical qubits is investigated by mapping between these two qubits. The steps for state initialization and Bell state preparation in the optical qubit are discussed. Then the mapping to the hyperfine qubit is described and for both qubits the entanglement decay is measured. Remapping to the optical qubit after a 20 ms storage time and the application of further gate operations is demonstrated. Due to the nuclear spin of  $I = 7/2$ , the isotope  $^{43}\text{Ca}^+$  has a relatively complex energy level structure compared to other ions used for quantum information processing. Magnetic field and polarization settings are discussed to reduce errors due to close by Zeeman-levels, which are especially harmful for gate operation in the case when large coupling strengths are required in a relatively short time. The findings of this chapter were also published in reference [77]. Similar techniques were implemented in experiments conducted in David Wineland's group [55, 56].

#### 6.3.1. Qubit preparation and manipulation

An energy level scheme for  $^{43}\text{Ca}^+$  with all relevant hyperfine levels is shown in figure 6.10 (a). In the experiments reported here, the hyperfine qubit, comprised of the states  $|↑\rangle \equiv S_{1/2}(F=3, m_F=0)$  and  $|↓\rangle \equiv S_{1/2}(F=4, m_F=0)$ , is driven by applying a microwave field (3.2 GHz) to one of the electrodes which is also used to compensate for external electric stray fields (see figure 4.1

electrodes (C)).

Each experimental sequence starts by Doppler-cooling the ions for 3 ms followed by sideband cooling of both axial modes close to the ground state ( $\bar{n}_{\text{com}}, \bar{n}_{\text{st}} \approx 0.03(3), 0.4(1)$ ; 5 ms and 3 ms). Optical pumping (as described in chapter 5.4) initializes both ions in the energy level  $S_{1/2}(F = 4, m_F = 4)$  in more than 98.9% of the cases.

Subsequently the populations of both ions are transferred by a  $\pi$ -pulse to the energy level  $D_{5/2}(F = 3, m_F = 2)$  (transfer 1). By turning on the lasers at 397 nm and 866 nm for 500  $\mu\text{s}$  one can detect residual population remaining in the  $S_{1/2}$  state manifold (PMT check). All cases where more than 3 photons are detected are rejected ( $\sim 20$  photons/ms are received per ion in the  $S_{1/2}$ -state at a dark count rate of 0.2 photons per ms). The rejection rate is typically 2%. Initialization of the hyperfine qubit is completed by another  $\pi$ -pulse (transfer 2) on the transition  $D_{5/2}(F = 3, m_F = 2) \leftrightarrow S_{1/2}(F = 4, m_F = 0) \equiv |\downarrow\rangle$ . In total the initialization of internal and external degrees of freedom takes about 12 ms and the qubit state  $|\downarrow\downarrow\rangle$  is populated with a fidelity of more than 99.2%. The fidelity of state initialization to  $|\downarrow\downarrow\rangle$  is measured by transferring the population with two consecutive  $\pi$ -pulses from  $|\downarrow\downarrow\rangle$  to two different Zeeman-levels in the  $D_{5/2}$  manifold ( $D_{5/2}(F = 3, m_F = 2)$  and  $D_{5/2}(F = 5, m_F = 2)$ ) and determining the remaining population in the  $S_{1/2}$  by fluorescence detection. The fidelity of optical pumping is determined in a similar way.

The magnetic field is set to 6.0 G in order to achieve a sufficiently large frequency separation of the neighboring transition lines in the spectrum of the  $S_{1/2} \leftrightarrow D_{5/2}$  quadrupole transition [126]. The transition  $|\downarrow\rangle \leftrightarrow D_{5/2}(F = 6, m_F = 1) \equiv |\uparrow\rangle$  is chosen as optical qubit because of its small magnetic field sensitivity of 350 kHz/G (which is at least a factor of two lower than the sensitivity of any  $m_F = 0$  to  $m_F = 0$  transition for the chosen magnetic field) and in order to avoid having coinciding resonances with (micro)motional sidebands of other spectral components. Moreover, this choice of optical qubit has the advantage of a comparatively large Clebsch-Gordan coefficient which together with a carefully set laser polarization (for this qubit we use beam 1 as shown in figure 5.4(a)) suppresses neighboring Zeeman transitions with  $\Delta m \neq +1$ . The transitions  $\Delta m = 0$  and 2 are suppressed by factors of 38 or more in terms of their Rabi frequencies, the strongest being the  $|\downarrow\rangle \leftrightarrow D_{5/2}(F = 6, m_F = 0)$  transition, whose resonance is more than 4 MHz away from the  $|\downarrow\rangle \leftrightarrow |\uparrow\rangle$  transition. The two closest transitions are  $S_{1/2}(F = 4, m_F = \pm 1) \leftrightarrow |\uparrow\rangle$  ( $\gtrsim 2$  MHz away) which are suppressed by a factor of 270 in coupling strength. The high coupling strength on the gate transition reduces the required power for the gate operation and thus the AC-Stark shift caused by off-resonant coupling to dipole transitions.

After initialization to  $|\downarrow\downarrow\rangle$ , a Mølmer-Sørensen entangling operation (MS 1) consisting of a single bichromatic laser pulse is applied to the optical qubit transition to create a Bell state of  $|\downarrow\downarrow\rangle + i|\uparrow\uparrow\rangle$ . The gate time  $\tau_{\text{gate}} = 100 \mu\text{s}$  corresponds to a detuning of 10 kHz from the axial sideband. For the chosen beam geometry, these settings lead to an AC-Stark shift of 3.5 kHz which is fully compensated by using different coupling strengths  $\Omega_b, \Omega_r$  for the red and the blue detuned frequency component with  $\xi = 0.14$ .

### 6.3 High fidelity entanglement of $^{43}\text{Ca}^+$ hyperfine clock states

**Table 6.1.:** Duration and errors of each experimental step and the achieved state fidelities.

Experiment step	Duration ( $\mu\text{s}$ )	Error (%)	State fidelity (%)
Opt. pumping	600	< 1.1	> 98.9
Transfer 1	20	0.7	98.2
PMT check	500	0.7	99.3
Transfer 2	20	< 0.1	> 99.2
Total prep. $ \downarrow\rangle$	1140	< 0.8	> 99.2
MS 1	100	2.3	96.9
Map	120	0.2	96.7
Wait	$20 \times 10^3$	2.2	94.6
Map $^{-1}$	120	0.7	93.9
MS 2	100	3.7	90.4
MS 3	100	2.9	87.8

#### 6.3.2. Experimental results

The fidelity of the created Bell state is determined by measuring the populations  $p_0 + p_2$  in  $|\downarrow\downarrow\rangle$  and  $|\uparrow\uparrow\rangle$  and the coherence between the two states. The coherence is again inferred from the amplitude of parity oscillations. The maximum fidelity was determined to 96.9(3)%. The durations and errors of all experimental steps and the achieved state fidelities are given in table 6.1.

By introducing a waiting time before the Bell state analysis, a Gaussian decay of the parity fringe contrast is observed. From this model a Bell state fidelity of 75% after 3.43(5) ms is extrapolated (see inset of figure 6.10(b)) corresponding to a loss of 50% of the coherence since the state populations hardly change. The magnetic field sensitivity of this optical qubit is 350 kHz/G which is one cause of dephasing. However, in measurements where a single  $^{43}\text{Ca}^+$  ion is probed on the first order field insensitive transition ( $S_{1/2}(F = 4, m_F = 4) \leftrightarrow D_{5/2}(F = 4, m_F = 3)$  at 3.4 G) a single qubit coherence times of 8.1(3) ms is obtained (see figure 4.8(a) inset). This leads to the conclusion that the decoherence on the optical qubit is also caused by acoustical noise picked up by the 2 m fiber cord used and the finite linewidth ( $\sim 20$  Hz) of the laser.

Mapping the optical qubit to the hyperfine qubit is achieved by a microwave  $\pi$ -pulse on the hyperfine qubit transition followed by a  $\pi$ -pulse on the optical qubit (map) which results in an average error rate of 0.2%. Detection of the hyperfine qubit states is done by shelving the population of  $|\downarrow\rangle$  to the  $D_{5/2}$  manifold by two consecutive  $\pi$ -pulses to different Zeeman states ( $D_{5/2}(F = 5, m_F = 2)$  and  $D_{5/2}(F = 6, m_F = -2)$ ) followed by fluorescence detection. A Bell state fidelity measurement after the mapping yields a parity fringe contrast of 95.7% - induced by varying the phase of a microwave  $\pi/2$ -pulse - corresponding to a target state fidelity of still 96.7%. By delaying the state analysis a Gaussian decay of the parity fringe pattern is observed (figure 6.10) corresponding to a 50% loss of phase coherence on a time scale of 96(3) ms which means that a factor 28 in coherence time is gained compared to the optical qubit.

For a successive gate application the Bell state is mapped back to the optical qubit (map $^{-1}$ ) after a waiting time of 20 ms and the gate (MS 2) is applied a second time, disentangling the ions to  $|\uparrow\uparrow\rangle$  in 90.4% of the cases, indicating an error of 3.7%. Another subsequent application of the gate (MS 3) adds an error of 2.9% leading to  $|\downarrow\downarrow\rangle - i|\uparrow\uparrow\rangle$  with a fidelity of 87.8%.

The results with successive gates suggest that the Bell state fidelity depends slightly on whether

the gate is applied to the input state  $|\downarrow\downarrow\rangle$  or  $|\uparrow\uparrow\rangle$ , an effect already observed in previous experiments. This observation can be explained by the different spectator states into which the population can leak by unwanted excitations. The effect is most prominent in a series of measurements where the magnetic field was set to 3.4 G. For this field strength the Zeeman splitting of the ground state and the axial trap frequency coincide to within 10 kHz. Using the transition  $|\downarrow\rangle \leftrightarrow D_{5/2}(F = 4, m_F = 2) \equiv |\uparrow'\rangle$  as optical qubit the polarization of beam 3 (see figure 5.4(a)) is adjusted to suppress the coupling strength to the nearest neighboring transitions. Note that in this geometry and polarization setting, both  $\Delta m = \pm 2$  have optimal coupling, so a higher gate laser power is required as compared to  $|\uparrow\rangle$ . This leads to Bell state fidelities of up to 96.3% after a single gate operation applied to  $|\downarrow\downarrow\rangle$ . The decoherence for these Bell states after mapping to the hyperfine qubit is also shown in figure 6.10(b). Applying the gate operation on the input state  $|\uparrow'\uparrow'\rangle$  the maximum obtained Bell state fidelity after a single gate operation is only 92%. Further measurements at a magnetic field of 1.36 G where we expected no coincidences of spectral components reveal a maximum Bell state fidelity of 95%. For these measurements, beam 1 was used again with  $|\downarrow\rangle \leftrightarrow |\uparrow\rangle$  as the optical qubit.

## 6.4. Comparison between $^{40}\text{Ca}^+$ and $^{43}\text{Ca}^+$ .

Several experiments including this thesis have demonstrated that  $^{40}\text{Ca}^+$  and  $^{43}\text{Ca}^+$  ions are suited for QIP processing. Most DiVincenzo criteria including high fidelity entangling gates have been demonstrated for both isotopes.  $^{40}\text{Ca}^+$  has the advantage of a very simple level structure but lacks the possibility to encode qubits in states with low magnetic field dependence. Furthermore the coherence time of the optical qubit suffers from laser frequency noise. Handling  $^{43}\text{Ca}^+$  is much more difficult due to its complicated level structure. The advantage of  $^{43}\text{Ca}^+$  is that qubits can be encoded in hyperfine and optical states with low magnetic field dependence. The hyperfine qubit has an additional advantage as it can be manipulated by either a Raman laser or a microwave field such that the frequency instability of the driving field is negligible.

Comparing the results for entangling  $^{43}\text{Ca}^+$  ion with the results obtained for entangling  $^{40}\text{Ca}^+$  ions, one can conclude that low errors of the Mølmer-Sørensen interaction on the optical qubit require that the qubit transition is well isolated from other spectral components such that no other transitions are erroneously excited. This view is supported by the observation that the gate mechanism favors a high magnetic field, where the transitions to neighboring lines are spectrally well separated. However, the sensitivity to magnetic field fluctuations of the hyperfine qubit increases for higher fields. Therefore, a particularly interesting regime for  $^{43}\text{Ca}^+$  ions occurs at a magnetic field of 150 G where nonlinearities in ground state Zeeman splitting lead to a first order magnetic field insensitive transition  $S_{1/2}(F = 4, m_F = 0) \leftrightarrow S_{1/2}(F = 3, m_F = 1)$ . This promises even longer coherence times as well as smaller errors for all spectrum dependent operations since the Zeeman splitting is huge compared to the measurements presented here.

The following points summarize and compare the operations used to handle the optical qubit in  $^{40}\text{Ca}^+$  and the optical and hyperfine qubit in  $^{43}\text{Ca}^+$ . Additionally the coherence times achieved in this experiment for different qubits are given.

## 6.4 Comparison between $^{40}\text{Ca}^+$ and $^{43}\text{Ca}^+$ .

---

Doppler-cooling is more complicated for  $^{43}\text{Ca}^+$ :

- $^{40}\text{Ca}^+$ : One  $\pi$ -polarized 397 nm laser and one 866 nm laser is sufficient for Doppler-cooling.
- $^{43}\text{Ca}^+$ : Multiple frequency components in the  $\sigma^+$ -polarized 397 nm laser and the 866 nm laser are necessary for Doppler cooling. Additionally, a second  $\pi$ -polarized 397 nm laser is needed to avoid population trapping in dark states.

State initialization of the  $^{43}\text{Ca}^+$  hyperfine qubit is more complicated than initializing the optical qubit:

- optical qubit: Optical pumping with a  $\sigma^+$ -polarized 397 nm is sufficient to initialize the state of  $^{40}\text{Ca}^+$  to  $S_{1/2}, m = 1/2$  or the state of  $^{43}\text{Ca}^+$  to  $S_{1/2}, F = 4, m_F = 4$ .
- hyperfine qubit: To initialize the state  $S_{1/2}, F = 4, m_F = 0$  two additional  $\pi$  pulses on the quadrupole transition or four microwave  $\pi$  pulses are necessary.

The Mølmer-Sørensen gate operation works better for  $^{40}\text{Ca}^+$  ions:

- $^{40}\text{Ca}^+$ : A Mølmer-Sørensen gate operation has been achieved which generated Bell states with fidelities exceeding 99%. [40]
- $^{43}\text{Ca}^+$ : The gate fidelity is limited by off-resonant excitation of close-by Zeeman-states to about 97%. [77]

The coherence properties of  $^{43}\text{Ca}^+$  qubits are better than the coherence properties of  $^{40}\text{Ca}^+$  qubits:

- $^{40}\text{Ca}^+$  optical qubit: The coherence time for a single ion is limited to about 3 ms by magnetic field fluctuations and laser frequency noise.
- $^{43}\text{Ca}^+$  optical qubit: Due to the availability of magnetic field independent transitions the coherence time is only limited by the laser stability. For a single ion a coherence time of 8 ms was measured.
- $^{43}\text{Ca}^+$  hyperfine qubit: For the hyperfine qubit  $S_{1/2}, F = 4, m_F = 0 \leftrightarrow S_{1/2}, F = 3, m_F = 0$  a coherence time of several seconds has been measured. [154]

Which isotope is chosen for a particular experiment depends on what sets the experimental limit in the sequences that should be run. If the sequence is short and one is interested in the best overall fidelity (considering the current experimental status) and the easiest handling, then  $^{40}\text{Ca}^+$  should be used. If the limit is set by the coherence time then one should consider using  $^{43}\text{Ca}^+$ . It is not absolutely necessary to use the hyperfine qubit in  $^{43}\text{Ca}^+$ . The coherence time can already be increased by choosing a magnetic field independent transition on the optical qubit in  $^{43}\text{Ca}^+$ . This has the advantage that the handling is still quite simple and one avoids the complicated read out and initialization steps of the hyperfine qubit.



---

## 7. Experimental test of quantum contextuality

Since the beginning of quantum mechanics (QM) it has been debated whether hidden variable (HV) theories can account for the intriguing features of QM [64, 156]. Especially the indeterminism of QM was a feature some physicists could not accept and was one of the reasons why HV theories came up. In the sixties, Bell found that local HV theories cannot reproduce the quantum mechanical correlations for local measurements on entangled states [65]. Later, a series of experiments confirmed a conflict between HV and QM theories by realizing a refined version of Bell's "Gedankenexperiment" [66–69]. These experimental refutations led to additional assumptions and restrictions for the structure of local HV theories.

Kochen, Specker and Bell [70–72] proposed another HV theorem testing for non-contextuality of measurements. Non-contextuality is the property of a HV model that the value of a measurement  $v(A)$  is determined, regardless of which other compatible measurement is measured jointly with  $A$ . Two or more measurements  $(A, B, C, \dots)$  are compatible if they can be measured jointly on the same individual system without disturbing each other. Compatible measurements can be made simultaneously or in any order and can be repeated any number of times on the same individual system and must always give the same result independently of the initial state of the system. A context is a set of compatible measurements. A physical model is called non contextual if it assigns a measurement result independent of which other compatible measurements are carried out on the probed system. Non contextuality is a plausible assumption for all physical models especial for measurements on distant systems or in the case of measurements concerning different degrees of freedom on the same system. The KS theorem states that noncontextual HV theories cannot reproduce the predictions of QM.

For some time it has been debated whether the Kochen Specker (KS) theorem could be experimentally tested at all [157, 158]. Nevertheless an experiment has been proposed testing for these HV theories [159]. Here the first experiment testing a complete Kochen Specker theorem [75] falsifying non-contextual HV theories is presented. Recently additional results with photons [73] and NMR qubits [74] have shown similar results.

In the following chapter the notions compatibility and contextuality as well as the KS theorem will be discussed. Then the experimental realization of quantum non-demolition measurements and a test of the Kochen Specker theorem will be shown. At the end of this chapter the results will be analyzed and possible loopholes will be discussed. The first section is taken from reference [160] whereas the experimental findings were already published in reference [75].

## 7.1. The Kochen-Specker theorem

### 7.1.1. Measurement scenario

The situation in the experiment will be the following: On an individual system a sequence of dichotomic measurements (outcomes  $\pm 1$ ) will be performed. The question that arises is: under which conditions can the result of such measurements be explained by HV theories? Or more precisely, which conditions a HV model has to violate to reproduce the QM predictions? The HV model will be described by a distribution  $p(\lambda)$  with the hidden variable  $\lambda \in \Lambda$  from a set  $\Lambda$ . The distribution summarizes all information about the past, including all preparation steps and all measurements already performed. Causality is assumed, so the distribution is independent of any event in the future. It rather determines all the probabilities of the results of all possible future sequences of measurements. We assume that, for a fixed value of the HV, the outcomes of future sequences of measurements are deterministic, hence all indeterministic behavior stems from the probability distribution.

### 7.1.2. Notation

In an experiment the state of the system is prepared in a repeatable way. In the language of HV-models this leads to a probability distribution  $p_{\text{exp}}(\lambda)$  that can be repeatedly produced even though its actual form is unknown. In a single instance of an experiment, one obtains a state determined by the HV  $\lambda_{\text{exp}}$ . Which  $\lambda_{\text{exp}}$  has been prepared cannot be controlled by the experimentalist and the HV is distributed according to  $p_{\text{exp}}(\lambda)$ .

The following notation will be used to describe measurements and their outcomes.  $A_i$  denotes the measurement of the property  $A$  at the position  $i$  in the sequence. A sequence of measurements is denoted by  $A_1B_2C_3$  when  $A$  is measured first, then  $B$  and finally  $C$ . The result of a specific measurement e.g.  $B_2$  in such a sequence is written as  $v(B_2|A_1B_2C_3)$ . In addition  $v(A_1B_2C_3) = v(A_1|A_1B_2C_3)v(B_2|A_1B_2C_3)v(C_3|A_1B_2C_3)$ . For the probability distribution  $p(\lambda)$ , one can define probabilities like  $p(B_2^+|A_1B_2C_3)$  [or  $p(B_2^+C_3^-|A_1B_2C_3)$ ] denoting the probability of obtaining the value  $B_2 = +1$  [and  $C_3 = -1$ ] when the sequence  $A_1B_2C_3$  is measured. Then, one can also consider mean values like  $\langle B_2|A_1B_2C_3 \rangle = p(B_2^+|A_1B_2C_3) - p(B_2^-|A_1B_2C_3)$ , or the mean value of the complete sequence,  $\langle A_1B_2C_3 \rangle = p[v(A_1B_2C_3) = +1] - p[v(A_1B_2C_3) = -1]$ .

### 7.1.3. Compatibility of measurements

First the notion of compatibility has to be defined. In the simplest case, this is a relation between a pair of observables,  $A$  and  $B$ . For that, let  $S_{AB}$  denote the (infinite) set of all sequences, which use only measurements of  $A$  and  $B$ , that is,  $S_{AB} = A_1, B_1, A_1A_2, A_1B_2, B_1A_2, \dots$ . Then one can formulate:

*Definition 1.* Two observables  $A$  and  $B$  are compatible, denoted by  $A \sim B$ , if the following two conditions are fulfilled:

- (i) For any instance of a state (that is, for any  $\lambda_{\text{exp}}$ ) and for any sequence  $S \in S_{AB}$  the obtained

## 7.1 The Kochen-Specker theorem

---

values of A and B remain the same, i.e.

$$\begin{aligned}v(A_k|S) &= v(A_l|S), \\v(B_m|S) &= v(B_n|S),\end{aligned}$$

where k,l,m,n are all possible indices for which the considered observable is measured at the positions k,l,m,n in the sequence  $S$ .

- (ii) For any state preparation (that is for any  $p_{\text{exp}}(\lambda)$ ), the mean values of A and B during the measurement of any two sequences  $S_1, S_2 \in S_{AB}$  stay the same, i.e.

$$\begin{aligned}\langle A_k|S_1 \rangle &= \langle A_l|S_2 \rangle, \\ \langle B_m|S_1 \rangle &= \langle B_n|S_2 \rangle.\end{aligned}$$

Conditions (i) and (ii) are necessary conditions for compatible observables. Two observables which violate one of them cannot be called compatible.

It is important to note that the compatibility of two observables is experimentally testable by preparing all possible  $\lambda_{\text{exp}}$  or  $p_{\text{exp}}(\lambda)$ . The fact that these sets or the set  $S_{AB}$  may be infinite is not a specific problem here, as any measurement device or physical law can only be tested in a finite number of cases.

One should note, that (ii) does not necessarily follow from (i), as will be illustrated by the following example: Consider a HV model where, for any  $\lambda$ , all  $v(A_k|S)$  are +1 when the first measurement in  $S$  is  $A_1$ , while they are -1 when the first measurement is  $B_1$ . The values  $v(B_m|S)$  are always +1. Then, condition (i) is fulfilled, while (ii) is violated, since  $\langle A \rangle = 1$  but  $\langle A_2|B_1A_2 \rangle = -1$ .

Finally, it should be added that the notion of compatibility can be extended to three or more observables. For instance, if three observables A,B,C are investigated, one considers the set  $S_{ABC}$  of all measurement sequences involving measurement of A,B or C and extends conditions (i) and (ii) in an obvious way.

### 7.1.4. Operational definition of noncontextuality

Noncontextuality means that the value of any observable A does not depend on which other compatible observables are measured jointly with A. For the model, noncontextuality is formulated as a condition on a HV model as follows:

*Definition 2.* Let A,B,C be observables in a HV model, where A is compatible with B, and A is also compatible with C: The HV model is noncontextual if it assigns, for any  $\lambda$  an outcome of A which is independent of whether B or C is measured before or after A, that is,

$$v(A_1|A_1B_2) = v(A_2|B_1A_2) = v(A_1|A_1C_2) = v(A_2|C_1A_2). \quad (7.1)$$

Hence, for these sequences one can write down  $v(A)$  as being independent of the sequence. If the condition is not fulfilled, the model is called contextual. If A is an element of several larger sets of compatible observables, the conditions in equation (7.1) can be extended in a straightforward way.

Note that the most important assumptions in (7.1) are that  $v(A_1|A_1B_2) = v(A_2|B_1A_2)$  and  $v(A_1|A_1C_2) = v(A_2|C_1A_2)$ . If these are fulfilled, the remaining equality follows from the physically very plausible assumption, that the result of  $A_1$  should not depend on which other observable is measured after  $A_1$  (this observable may be compatible with A or not). It is important to note that the condition (7.1) is an assumption about the model and — contrary to the definition of compatibility — not experimentally testable. This is due to the fact that for a given instance of a state (corresponding to some unknown  $\lambda$ ) the experimenter has to decide whether to measure A or B first.

In the definition, condition (7.1) is assumed for any  $\lambda$ . One may wonder whether this requirement is too strong, since in any experiment only certain  $\lambda_{\text{exp}}$  can be tested. Assuming, however, that there are certain  $\lambda$  which can never occur as a  $\lambda_{\text{exp}}$  does not make much sense, as in such a HV theory these  $\lambda$  cannot affect any experimentally observed measurement result, as any  $p_{\text{exp}}(\lambda)$  has to assign a vanishing probability density to them. Hence, one can disregard this case. Finally, let us add here that if larger sets of compatible observables are considered, definitions (1) and (2) have to be extended to longer sequences. For instance, if the observables in each of the sets  $\{A, B, C\}$  and  $\{A, a, \alpha\}$  are all compatible, then, the condition that the assignment of a value to A is independent of the context results in conditions similar to equation (7.1), but with sequences of length three.

$$v(A_1|A_1B_2C_3) = v(A_2|B_1A_2C_3) = v(A_1|A_1a_2\alpha_3) = v(A_2|\alpha_1A_2a_3) = \dots \quad (7.2)$$

### 7.1.5. The Kochen Specker inequality for noncontextual models

The KS theorem states that noncontextual HV models cannot reproduce all predictions of QM. Here one (out of many) possible inequalities is discussed involving compatible measurements, which holds for the QM case but is violated by noncontextual HV theories.

Let's consider the following array (Mermin Peres square [161, 162]) of observables of a four-level quantum system (for instance two spin- $\frac{1}{2}$ -particles)

$$\begin{array}{lll} A = \sigma_z^{(1)} \otimes I^{(2)} & B = I^{(1)} \otimes \sigma_z^{(2)} & C = \sigma_z^{(1)} \otimes \sigma_z^{(2)} \\ a = I^{(1)} \otimes \sigma_x^{(2)} & b = \sigma_x^{(1)} \otimes I^{(2)} & c = \sigma_x^{(1)} \otimes \sigma_x^{(2)} \\ \alpha = \sigma_z^{(1)} \otimes \sigma_x^{(2)} & \beta = \sigma_x^{(1)} \otimes \sigma_z^{(2)} & \gamma = \sigma_y^{(1)} \otimes \sigma_y^{(2)} \end{array} \quad (7.3)$$

and the measurement products of each row  $R_k$  and column  $C_k$  given by

$$\begin{array}{ll} R_1 = v(A) \cdot v(B) \cdot v(C) & C_1 = v(A) \cdot v(a) \cdot v(\alpha) \\ R_2 = v(a) \cdot v(b) \cdot v(c) & C_2 = v(B) \cdot v(b) \cdot v(\beta) \\ R_3 = v(\alpha) \cdot v(\beta) \cdot v(\gamma) & C_3 = v(C) \cdot v(c) \cdot v(\gamma). \end{array} \quad (7.4)$$

Here,  $\sigma_i^{(k)}$  denotes the Pauli matrix acting on the  $k$ -th particle, and all the observables have the outcomes  $\pm 1$ . Moreover, in each of the rows or columns of (7.3), the observables are compatible. In any row or column, their measurement product  $R_k$  or  $C_k$  equals 1, except for the third column where it equals  $-1$ . Therefore, quantum mechanics yields for the product  $\prod_{k=1,2,3} R_k C_k$  a value of  $-1$ , in contrast to non-contextual models.

## 7.2 Experimental realization of QND measurements

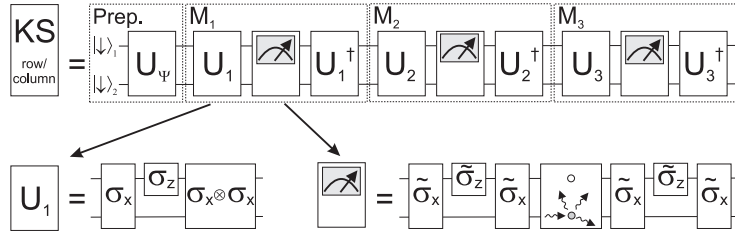


**Figure 7.1.:** Experimental measurement scheme. **a** For the measurement of the  $j$ th row (column) of the Mermin-Peres square (7.3), a quantum state is prepared on which three consecutive QND measurements  $M_k$ ,  $k = 1, 2, 3$ , are performed measuring the observables  $A_{jk}$  ( $A_{kj}$ ). Each measurement consists of a composite unitary operation  $U_k$  that maps the observable of interest onto one of the single-qubit observables  $\sigma_z^{(1)}$  or  $\sigma_z^{(2)}$  which are measured by fluorescence detection. The unitary operations  $U$  are synthesized from single-qubit and maximally entangling gates. In the lower line,  $\sigma_i$ ,  $\tilde{\sigma}_i$  symbolize, respectively, the Hamiltonian acting on the qubit and on the  $D_{5/2}$  Zeeman subspace spanned by  $\{|\downarrow\rangle, |a\rangle\} = \{S_{1/2}, m_j = 1/2, D_{5/2}, m_j = 5/2\}$  which is used for hiding one ion's quantum state from fluorescence light during detection[49].

To test this property, it has to be expressed as an inequality since no experiment yields ideal quantum measurements. Recently, it has been shown that the inequality

$$\langle \mathcal{X}_{KS} \rangle = \langle R_1 \rangle + \langle R_2 \rangle + \langle R_3 \rangle + \langle C_1 \rangle + \langle C_2 \rangle - \langle C_3 \rangle \leq 4 \quad (7.5)$$

holds for all non-contextual theories [159], where  $\langle \dots \rangle$  denotes the ensemble average. Quantum mechanics predicts for *any* state that  $\langle \mathcal{X}_{KS} \rangle = 6$ , thereby violating inequality (7.5). For an experimental test, an ensemble of quantum states  $\Psi$  needs to be prepared and each realization subjected to the measurement of one of the possible sets of compatible observables. Here, it is of utmost importance that all measurements of  $A_{ij}$  are context-independent [159], i.e.,  $A_{ij}$  must be detected with a quantum non-demolition (QND) measurement that provides no information whatsoever about any other compatible observable.

## 7.2. Experimental realization of QND measurements

As pointed out in the preceding theory section QND measurements are necessary to test the Kochen Specker theorem. The two qubit observables listed in table 7.3 can be measured in a non destructive way by applying a unitary transformation  $U$  to the state  $\Psi$  prior to measuring  $\sigma_z$  on one ion, and its inverse operation  $U^\dagger$  after the measurement (see chapter 2.1.3). The gate decompositions of the unitary operations necessary to perform all two qubit observables for the Mermin Peres square are given in table 7.1. These pulse sequences will be used in the chapter 7.3 to determine all observables for a test of contextual hidden variable theories. The decompositions of  $U_{ij}$  into the elementary gate operations available in our setup were found by a gradient-ascent based numerical search routine [135]. The unitary transformations are designed such that the information about the observable is mapped onto a single ion (in this case ion 1). The state detection of ion 1 only ensures that a single bit of information is acquired. The final inverse operation guarantees that

$$\begin{aligned}
 U[\sigma_x \otimes \sigma_x] &= U_y^{MS}(-\frac{\pi}{2})U_z^1(\frac{\pi}{2}) & U[\sigma_x \otimes \sigma_z] &= U_x^{MS}(-\frac{\pi}{2})U_x(\frac{\pi}{2}) \\
 U[\sigma_y \otimes \sigma_y] &= U_x^{MS}(-\frac{\pi}{2})U_z^1(\frac{\pi}{2}) & U[\sigma_z \otimes \sigma_x] &= U_y^{MS}(-\frac{\pi}{2})U_x(-\frac{\pi}{2}) \\
 U[\sigma_z \otimes \sigma_z] &= U_y^{MS}(-\frac{\pi}{2})U_z^1(\frac{\pi}{2})U_y(\frac{\pi}{2})
 \end{aligned}$$

**Table 7.1.:** Gate decomposition of the mapping operations  $U[\sigma_i \otimes \sigma_j]$  employed for measuring the five two-qubit spin correlations in the Mermin Peres square.

the two ions are in an eigenstate of the measurement.

It is important to note that some of the observables listed in table 7.3 require unitary transformations that are two qubit entangling gates (see table 7.1). As it turns out the most complicated series of measurements (row 3 and column 3 in the Mermin Peres square) requires a total of 6 two-qubit gate operations. This, by it self, is already quite demanding but gets even more difficult by the fact that the state of one ion has to be detected in between the unitary transformations. The problem that arises with state detection is that the ions do not remain in the ground state but get heated to the Doppler limit. Fortunately the Mølmer-Sørensen gate operation is insensitive to the motional state of the ions (see chapter 6.1). This enabled us to omit complicated re-cooling schemes, as demonstrated in [55], in the experimental realization of the QND measurements.

The measurement scheme that has to be employed to measure one row or column of the Mermin Peres square can be seen in figure 7.1. In the following this scheme will be explained in more detail by an example where  $(|\downarrow\rangle - |\uparrow\rangle)_1 \otimes (|\downarrow\rangle - |\uparrow\rangle)_2$  is created as an input state and the last row in the Mermin Peres square is measured.

For this example and the experiment described in the following section, a pair of  $^{40}\text{Ca}^+$  ions is trapped in a linear Paul trap with axial and radial vibrational frequencies of  $\omega_{ax} = (2\pi) 1.465$  MHz and  $\omega_r \approx (2\pi) 3.4$  MHz in a magnetic field of  $B = 4$  Gauss. The ions are Doppler-cooled by exciting the  $S_{1/2} \leftrightarrow P_{1/2}$  and  $P_{1/2} \leftrightarrow D_{3/2}$  dipole transitions. Optical pumping initializes an ion with a fidelity of 99.5% to the qubit state  $|\downarrow\rangle \equiv |S_{1/2}, m_j = 1/2\rangle$ , the second qubit state being  $|\uparrow\rangle \equiv |D_{5/2}, m_j = 3/2\rangle$ .

The unitary operation to create the input state  $(|\downarrow\rangle - |\uparrow\rangle)_1 \otimes (|\downarrow\rangle - |\uparrow\rangle)_2$  is a  $\pi/2$ -pulse on both ions  $U_\Psi = U_y(\frac{\pi}{2})$ . After the state preparation the first QND measurement, determining the parity  $\sigma_z \otimes \sigma_z$  of the input state, has to be carried out. This can be done by applying a unitary transformation which is equivalent to a CNOT operation (see chapter 2.1.3) followed by a PMT detection of ion 1. This unitary operation maps the parity of the state on ion 1 and is given in terms of gate operations available in the experiment:  $U_1 = U_y^{MS}(-\frac{\pi}{2})U_z^1(\frac{\pi}{2})U_y(\frac{\pi}{2})$  which can be written in matrix representation as

$$U_1 = \begin{pmatrix} 1 & 0 & 0 & 1 \\ 0 & 1 & -1 & 0 \\ i & 0 & 0 & -i \\ 0 & i & i & 0 \end{pmatrix}. \quad (7.6)$$

This operation maps the input state to  $|\downarrow\downarrow\rangle - i|\uparrow\uparrow\rangle$ . Detecting the state of ion 1 will result in equally finding  $|\downarrow\rangle$  and  $|\uparrow\rangle$ .  $|\downarrow\rangle$  will be identified with the +1 eigenstate and  $|\uparrow\rangle$  with the -1

### 7.3 Testing the Kochen Specker inequality

eigenstate. By averaging over many realization the measurement shows that the parity of the input state is zero.

State detection of ion 1 is achieved by fluorescence detection. Ion 2 is hidden from the fluorescence laser by transferring the population in the state  $|\downarrow\rangle = S_{1/2}, m_j = 1/2$  to the  $D_{5/2}, m_j = 5/2$  state. The hiding is done by using a pulse sequence similar to the one shown in figure 5.4(b). The only difference is that the  $\frac{\pi}{4}$  pulses are replaced by  $\frac{\pi}{2}$  pulses such that the pulse sequence reads as  $U_x^{(2)}(\pi) = U_x(\frac{\pi}{2})U_z^{(1)}(\pi)U_x(\frac{\pi}{2})$ . The same series of pulses is used to un-hide ion 2 after the state detection. Additional information on the hiding procedure can be found in appendix A.2

The inverse unitary operation to create an eigenstate of the measurement is achieved by applying the pulse sequence  $U_1^\dagger = U_{-y}(\frac{\pi}{2})U_z^1(\frac{\pi}{2})U_y^{MS}(-\frac{\pi}{2})U_z^1(\pi)$  which can be written in matrix representation as

$$U_1^\dagger = \begin{pmatrix} i & 0 & 1 & 0 \\ 0 & i & 0 & 1 \\ 0 & -i & 0 & 1 \\ i & 0 & -1 & 0 \end{pmatrix}. \quad (7.7)$$

If ion 1 was detected in the state  $|\downarrow\rangle$  this operation maps the two ions onto the entangled state  $|\uparrow\uparrow\rangle + |\downarrow\downarrow\rangle$ . Similarly if ion 1 was detected in the state  $|\uparrow\rangle$  the two ions are mapped onto the state  $|\uparrow\downarrow\rangle + |\downarrow\uparrow\rangle$ . Subsequently the other two QND measurements are performed in the same way. With this example one can clearly see that entanglement is created during the measurement process even though the initial state was a product state.

### 7.3. Testing the Kochen Specker inequality

Equipped with the tools described in chapter 5.4 and 6.1, the singlet state  $\Psi = |\uparrow\downarrow\rangle - |\downarrow\uparrow\rangle / \sqrt{2}$  was created by applying the gate-operations  $U_z^{(1)}(\pi)U(\frac{\pi}{2}, \frac{3\pi}{4})U^{MS}(\frac{\pi}{2}, 0)$  to the initial state  $|\downarrow\downarrow\rangle$ . Then the three observables of a row or column of the Mermin-Peres square were measured consecutively (as describe in chapter 7.2). The results obtained for a total of 6,600 copies of  $\Psi$  are visualized in figure 7.2. The three upper panels show the distribution of measurement results  $\{v(A_{i1}), v(A_{i2}), v(A_{i3})\}$  and their products for the observables appearing in the rows of (7.3), the three lower panels show the corresponding results for the columns of the square. Subplot **f** demonstrates that  $\Psi$  is a common eigenstate of the observables  $\sigma_x^{(1)} \otimes \sigma_x^{(2)}, \sigma_y^{(1)} \otimes \sigma_y^{(2)}, \sigma_z^{(1)} \otimes \sigma_z^{(2)}$ , as only one of the spheres has a considerable size. Five of the correlations have a value close to +1 whereas  $\langle C_3 \rangle = -0.91(1)$ . By adding them up and subtracting  $\langle C_3 \rangle$ , one finds a value of  $\langle \mathcal{K}_{KS} \rangle = 5.46(4) > 4$ , thus violating equation (7.5).

To test the prediction of a state-independent violation, the experiment was repeated for nine other quantum states of different purity and entanglement. Figure 7.3 shows that indeed a state-independent violation of the Kochen-Specker inequality occurs,  $\langle \mathcal{K}_{KS} \rangle$  ranging from 5.23(5) to 5.46(4). It was also checked that a violation of (7.5) occurs irrespective of the temporal order of the measurement triples.

Figure 7.4 shows the results for all possible permutations of the rows and columns of (7.3) based on 39,600 realizations of the singlet state. When combining the correlation results for the 36 possible permutations of operator orderings in equation (7.3), all values for the Kochen-Specker

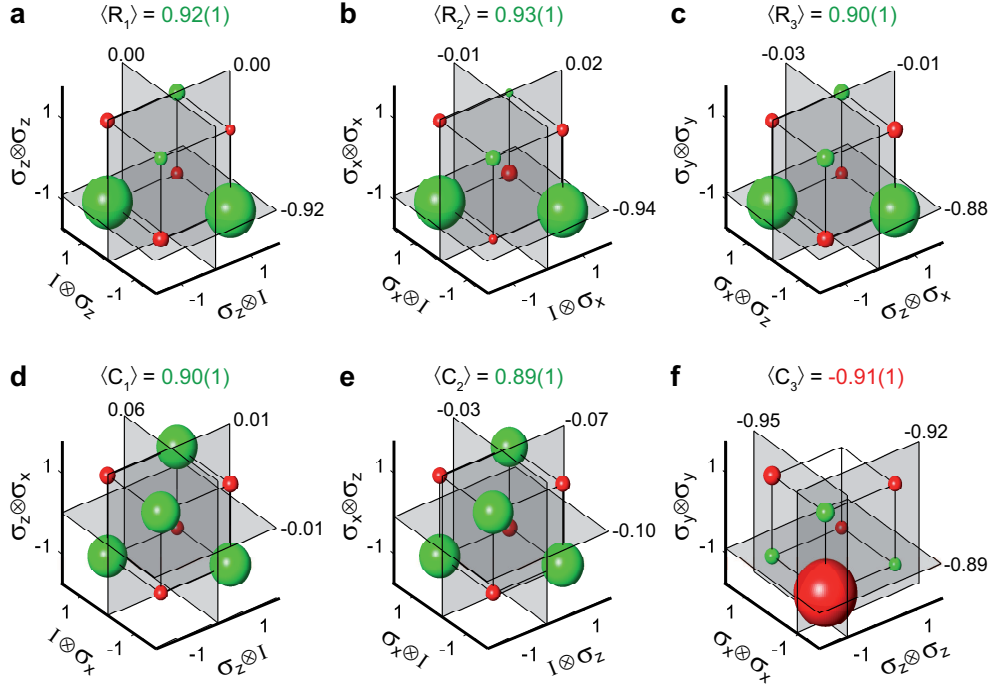


**Figure 7.2.:** Measurement correlations for the singlet state. **a** This subplot visualizes the consecutive measurement of the three observables  $A_{11} = \sigma_z^{(1)}$ ,  $A_{12} = \sigma_z^{(2)}$ ,  $A_{13} = \sigma_z^{(1)} \otimes \sigma_z^{(2)}$  corresponding to row 1 of the Mermin-Peres square. The measurement is carried out on 1,100 preparations of the singlet state. The volume of the spheres on each corner of the cube represents the relative frequency of finding the measurement outcome  $\{v_1, v_2, v_3\}$ ,  $v_i \in \{\pm 1\}$ . The exact probabilities for finding  $\{v_1, v_2, v_3\}$  are given in appendix A.1. The color of the sphere indicates whether  $v_1 v_2 v_3 = +1$  (green) or  $-1$  (red). The measured expectation values of the observables  $A_{1j}$  are indicated by the intersections of the shaded planes with the axes of the coordinate system. The average of the measurement product  $\langle R_1 \rangle$  is given at the top. **b-f** Similarly, the other five subplots represent measurements of the remaining rows or columns of the Mermin-Peres square. Subplot **f** demonstrates that the singlet state is a common eigenstate of the observables  $\sigma_x^{(1)} \otimes \sigma_x^{(2)}$ ,  $\sigma_y^{(1)} \otimes \sigma_y^{(2)}$ ,  $\sigma_z^{(1)} \otimes \sigma_z^{(2)}$ , as only one of the spheres has a considerable volume. Taking into account all the results, we find  $\langle \mathcal{K}_{KS} \rangle = 5.46(4)$  in this measurement. Error bars are  $1\sigma$ .

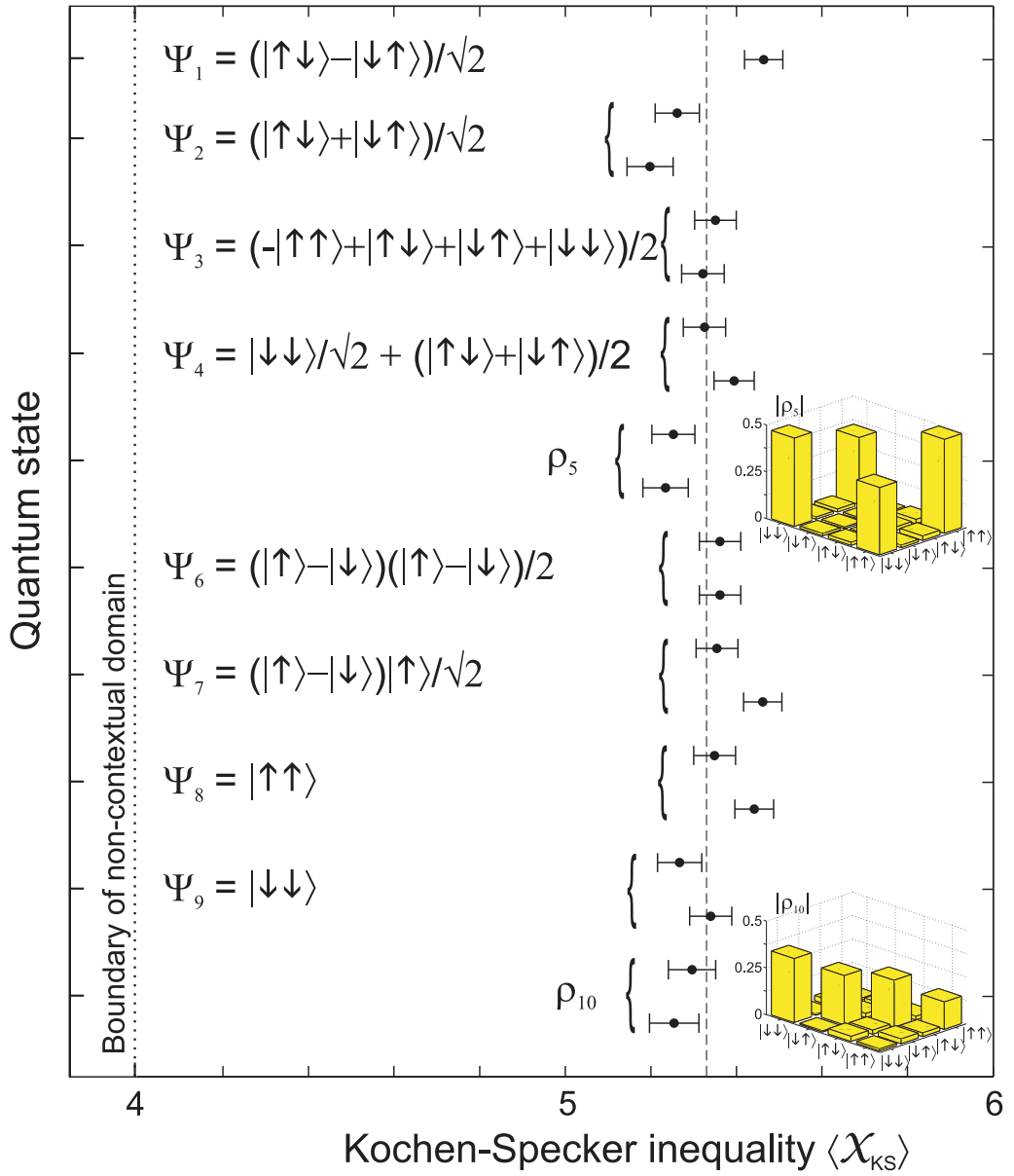


**Figure 7.3.:** State-independence of the Kochen-Specker inequality. The Kochen-Specker inequality was tested for ten different quantum states, including maximally entangled ( $\Psi_1$ - $\Psi_3$ ), partially entangled ( $\Psi_4$ ) and separable ( $\Psi_6$ - $\Psi_9$ ) almost pure states as well as an entangled mixed state ( $\rho_5$ ) and an almost completely mixed state ( $\rho_{10}$ ). All states are analysed by quantum state tomography which yields for the experimentally produced states  $\Psi_1$ - $\Psi_4$ ,  $\Psi_6$ - $\Psi_9$  an average fidelity of 97(2)%. For all states, one obtains a violation of inequality (7.5) which demonstrates its state-independent character, the dashed line indicating the average value of  $\langle \mathcal{X}_{KS} \rangle$ . Error bars are  $1\sigma$  (6,600 state realizations per data point).

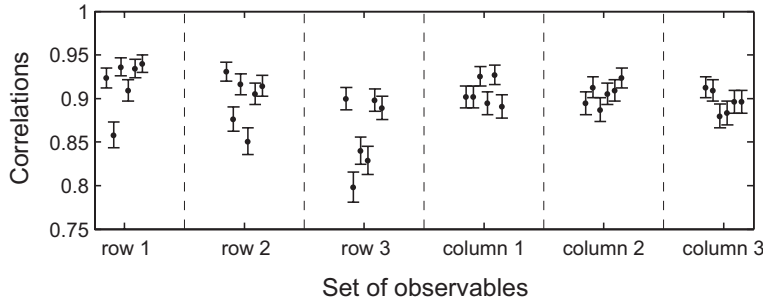


**Figure 7.4.:** Permutation within rows and columns of the Mermin-Peres square. As the three observables of a set are commuting, the temporal order of their measurements should have no influence on the measurement results. The figure shows the measured absolute values of the products of observables for any of the six possible permutations. The scatter in the experimental data is caused by experimental imperfections that affect different permutations differently. For the measurements shown here, in total 39,600 copies of the singlet state were used.

inequality  $\langle \mathcal{X}_{KS} \rangle$  fall within the range of 5.22 to 5.49. Because of experimental imperfections, the experimental violation of the Kochen-Specker inequality falls short of the quantum-mechanical prediction. The dominating error sources are imperfect unitary operations, in particular the entangling gates applied up to six times in a single experimental run. The errors are discussed further in section 7.5.1

## 7.4. Including imperfect measurements to close loopholes

All experimental tests of hidden-variable theories are subject to various possible loopholes. In this experiment, the detection loophole does not play a role, as the state of the ions is detected with near-perfect efficiency. From the point of view of a hidden variable theory, still objections can be made: In the experiment, the observables are not perfectly compatible and since the observables are measured sequentially, it may be that the hidden variables are disturbed (DHV) during the sequence of measurements, weakening the demand to assign to any observable a fixed value independently of the context.

Nevertheless, it is possible to derive inequalities for classical non-contextual models, wherein the hidden variables are disturbed during the measurement process [160]. The starting point to include imperfections is a Clauser-Horne-Shimony-Holt (CHSH) type inequality

$$\langle \mathcal{X}_{\text{CHSH}} \rangle = \langle AB \rangle + \langle CD \rangle + \langle AC \rangle - \langle BD \rangle \quad (7.8)$$

one can derive from equation (7.5) by replacing array (7.3) by

$$\begin{aligned} I^{(1)} \otimes I^{(2)} \quad A &= I^{(1)} \otimes \sigma_y^{(2)} & B &= \sigma_y^{(1)} \otimes \sigma_y^{(2)} \\ I^{(1)} \otimes I^{(2)} \quad C &= \sigma_x^{(1)} \otimes I^{(2)} & D &= \sigma_x^{(1)} \otimes \sigma_x^{(2)} \\ I^{(1)} \otimes I^{(2)} & & & I^{(1)} \otimes I^{(2)}. \end{aligned} \quad (7.9)$$

## 7.4 Including imperfect measurements to close loopholes

---

All nine observables fulfill the condition of compatibility but the inequality, similar to Bell tests, is now violated only by specific states. As most of the observables are now equal to the identity matrix the relevant measurements are  $A, B, C, D$ . A noncontextual HV model has to assign a fixed value to each measurement, and any such model predicts

$$|\langle \mathcal{X}_{\text{CHSH}} \rangle| \leq 2. \quad (7.10)$$

If we now consider the QM state

$$\Psi \propto |\uparrow\uparrow\rangle + i\gamma|\downarrow\uparrow\rangle + \gamma|\uparrow\downarrow\rangle + i|\downarrow\downarrow\rangle \quad (7.11)$$

where  $\gamma = \sqrt{2} - 1$ , we will find for equation 7.8 a value of

$$\langle \mathcal{X}_{\text{CHSH}} \rangle = 2\sqrt{2} \quad (7.12)$$

violating the HV inequality. The choice of observables is not unique and one can transform all observables by a global unitary transformation and obtain another set. In fact transformations are possible that lead to a maximal violation for unentangled states.

To deal with the case of imperfect measurements consider a HV model with a probability distribution  $p(\lambda)$  and let  $p[(A_1^+|A_1)$  and  $(B_1^+|B_1)]$  denote the probability of finding  $A^+$  if  $A$  is measured first and  $B^+$  if  $B$  is measured first, where these conditions are put onto the same instance of the HV. This probability is well defined in all HV models of the considered type but it is impossible to experimentally measure it directly. The aim is now to connect it to probabilities arising in sequential measurements, as this allows one to find contradictions between HV models and QM.

First, note that

$$p[(A_1^+|A_1) \text{ and } (B_1^+|B_1)] \leq p[A_1^+, B_2^+|A_1 B_2] + p[(B_1^+|B_1) \text{ and } (B_2^-|A_1 B_2)]. \quad (7.13)$$

This inequality is valid because if  $\lambda$  is such that it contributes to  $p[(A_1^+|A_1)$  and  $(B_1^+|B_1)]$ , then either the value of  $B$  stays the same when measuring  $A_1 B_2$  (hence  $\lambda$  contributes to  $p[A_1^+, B_2^+|A_1 B_2]$ ) or the value of  $B$  is flipped and  $\lambda$  contributes to  $p[(B_1^+|B_1)$  and  $(B_2^-|A_1 B_2)]$ . The first term  $p[A_1^+, B_2^+|A_1 B_2]$  is directly measurable as a sequence, but the second term is not directly experimentally accessible.

Let us rewrite

$$\langle AB \rangle = 1 - 2p[(A_1^+|A_1) \text{ and } (B_1^-|B_1)] - 2p[(A_1^-|A_1) \text{ and } (B_1^+|B_1)], \quad (7.14)$$

as the mean value obtained from the probabilities  $p[(A_1^\pm|A_1)$  and  $(B_1^\pm|B_1)]$ . Then, using equation (7.13), it follows that

$$\langle A_1 B_2 \rangle - 2p^{\text{flip}}[AB] \leq \langle AB \rangle \leq \langle A_1 B_2 \rangle + 2p^{\text{flip}}[AB], \quad (7.15)$$

where we used  $p^{\text{flip}}[AB] = p[(B_1^+|B_1) \text{ and } (B_2^-|A_1 B_2)] + p[(B_1^-|B_1) \text{ and } (B_2^+|A_1 B_2)]$  which can be interpreted as a probability that  $A$  flips a predetermined value of  $B$ .

Furthermore, using (7.8), we obtain within a HV model

$$|\langle \mathcal{X}_{\text{CHSH}} \rangle| \leq 2(1 + p^{\text{flip}}[AB] + p^{\text{flip}}[CD] + p^{\text{flip}}[AC] + p^{\text{flip}}[BD]). \quad (7.16)$$

The terms  $p^{\text{flip}}[AB]$ , etc. in inequality (7.16) are not experimentally accessible. Now we will discuss how they can be experimentally estimated when some assumptions on the HV model are made.

In order to obtain an experimentally testable version of inequality (7.16), we will assume that

$$p[(B_1^+|B_1) \text{ and } (B_2^-|A_1B_2)] \leq p[(B_1^+|B_1) \text{ and } (B_1^+, B_3^-|B_1A_2B_3)] = p[B_1^+, B_3^-|B_1A_2B_3]. \quad (7.17)$$

We must stress at this point that we do not assume that the set of HV values giving  $[(B_1^+|B_1) \text{ and } (B_2^-|A_1B_2)]$  is contained in the set giving  $(B_1^+, B_3^-|B_1A_2B_3)$ , the assumption only relates the sizes of these two sets. The motive is the following experimental procedure: Let us assume that one has a physical state, for which one surely finds  $B_1^+$ , if  $B_1$  is measured first, but one finds  $B_2^-$  if the sequence  $A_1B_2$  is measured. Physically, one would explain this behavior with a disturbance of the system due to the experimental procedures made when measuring  $A_1$ . The left hand side of (7.17) can be viewed as the amount of this disturbance. The right hand side quantifies the disturbance of  $B$  when the sequence  $B_1A_2B_3$  is measured. In real experiments, it can be expected that this disturbance is larger than when measuring  $A_1B_2$ , because of the additional experimental procedures involved. Note that in real experiments, a measurement of  $B$  will also disturb the value of  $B$  itself, as can be seen from the fact that sometimes the values of  $B_1$  and  $B_2$  will not coincide, if the sequence  $B_1B_2$  is measured (see chapter 7.5.1).

Assumption (7.17) gives a measurable upper bound on  $p^{\text{flip}}[AB]$ . One directly has

$$\begin{aligned} |\langle \mathcal{X}_{DHV} \rangle| = |\langle \mathcal{X}_{\text{CHSH}} \rangle| - 2(p^{\text{err}}[B_1A_2B_3] + p^{\text{err}}[D_1C_2D_3] + \\ + p^{\text{err}}[C_1A_2C_3] + p^{\text{err}}[D_1B_2D_3]) \leq 2, \end{aligned} \quad (7.18)$$

where we used  $p^{\text{err}}[B_1A_2B_3] = p[B_1^+, B_3^-|B_1A_2B_3] + p[B_1^-, B_3^+|B_1A_2B_3]$ , denoting the total disturbance probability of  $B$  when measuring  $B_1A_2B_3$ .

The point with this inequality is that if the observable pairs  $(A, B)$ ,  $(C, D)$ ,  $(A, D)$ , and  $(B, D)$  fulfill approximately the condition (i) of definition 1 in the definition of compatibility, the terms  $p^{\text{err}}$  will become small, and a violation of inequality (7.18) can be observed. To test this inequality we prepared the state  $\Psi$  and performed the measurements listed in (7.9). We find for the value  $\langle \mathcal{X}_{DHV} \rangle = 2.23(5) > 2$ . This proves that even disturbances of the hidden variables for not perfectly compatible measurements cannot explain the given experimental data. In principle, our analysis of measurement disturbances and dynamical hidden variable models can be extended to the full Mermin-Peres square. The error terms considering now four measurements in a row look like

$$p^{\text{flip}}[(AB)C] \leq p^{\text{err}}[(AB)C] = p[C_1^+ C_4^- | C_1 A_2 B_3 C_4] + p[C_1^- C_4^+ | C_1 A_2 B_3 C_4]. \quad (7.19)$$

Then, if one writes down the generalized form of inequality (7.5) there are more correction terms than in inequality (7.18), moreover they occur now with weight 4. On average, these  $p^{\text{err}}$  terms have to be smaller than  $2/48 \approx 0.0417$  in order to allow a violation. As can be seen in the next

## 7.5 Experimental results on imperfect measurements

**Table 7.2.:** Measurement correlations  $\langle A_i A_j | A_1 \dots A_5 \rangle$  between repeated measurements of  $A = \sigma_z \otimes I$  for a maximally mixed state. Observing a correlation of  $\langle A_i A_j | A_1 \dots A_5 \rangle = \alpha_{ij}$  means that the probability for the measurement results of  $A_i$  and  $A_j$  to coincide equals  $(\alpha_{ij} + 1)/2$ .

$\alpha_{ij}$	2	3	4	5
1	0.97(1)	0.97(1)	0.96(1)	0.95(1)
2		0.97(1)	0.97(1)	0.96(1)
3			0.98(1)	0.98(1)
4				0.98(1)

**Table 7.3.:** Measurement correlations  $\langle A_i A_j | A_1 \dots A_5 \rangle$  between repeated measurements of  $A = \sigma_x \otimes \sigma_x$  for a maximally mixed state. Observing a correlation of  $\langle A_i A_j | A_1 \dots A_5 \rangle = \alpha_{ij}$  means that the probability for the measurement results of  $A_i$  and  $A_j$  to coincide equals  $(\alpha_{ij} + 1)/2$ .

$\alpha_{ij}$	2	3	4	5
1	0.94(1)	0.88(1)	0.82(2)	0.80(2)
2		0.93(1)	0.87(2)	0.84(2)
3			0.90(1)	0.87(2)
4				0.93(1)

section the experimental techniques have to be improved to get in this regime and find a violation.

## 7.5. Experimental results on imperfect measurements

The fact that the results falls short of the quantum mechanical prediction of  $\langle \mathcal{X}_{KS} \rangle = 6$  is, as pointed out, due to imperfections in the measurement procedure. These imperfections could be incorrect unitary transformations but also errors occurring during the fluorescence measurement.

An instructive test consists in repeatedly measuring the same observable on a single quantum system and analyzing the measurement correlations. Table 7.2 shows the results of five consecutive measurements of  $A = \sigma_z \otimes I$  on a maximally mixed state based on 1100 experimental repetitions.

As expected, the correlations  $\alpha_{i,j} = \langle A_i A_j | A_1 \dots A_5 \rangle$  for  $j=i+1$  are independent of the measurement number  $i$  within the error bars. However, the correlations  $\alpha_{i,j}$  for  $j=i+k$  become smaller and smaller the bigger  $k$  gets. Table 7.3 shows another set of measurements correlations  $\langle A_i A_j | A_1 \dots A_5 \rangle$  where  $A = \sigma_x \otimes \sigma_x$ . Here, the correlations are smaller, since entangling interactions are needed for mapping  $A$  onto  $\sigma_z \otimes I$  which is experimentally the most demanding step.

It is also interesting to compare the correlations  $\langle A_1 A_3 | A_1 A_2 A_3 \rangle$  with the correlations  $\langle A_1 A_3 | A_1 B_2 A_3 \rangle$  for an observable  $B$  that is compatible with  $A$ . For  $A = \sigma_x \otimes \sigma_x$  and  $B = \sigma_z \otimes \sigma_z$ , we find  $\langle A_1 A_3 | A_1 A_2 A_3 \rangle = 0.88(1)$  and  $\langle A_1 A_3 | A_1 B_2 A_3 \rangle = 0.83(2)$  when measuring a maximally mixed state, i. e. it seems that the intermediate measurement of  $B$  perturbs the correlations slightly more than an intermediate measurement of  $A$ . Similar results are found for a singlet state, where  $\langle A_1 A_3 | A_1 A_2 A_3 \rangle = 0.92(1)$ ,  $\langle B_1 B_3 | B_1 B_2 B_3 \rangle = 0.91(1)$ , but  $\langle A_1 A_3 | A_1 B_2 A_3 \rangle = 0.90(1)$ , and  $\langle B_1 B_3 | B_1 A_2 B_3 \rangle = 0.89(1)$ . Because of  $\langle B_1 B_3 | B_1 A_2 B_3 \rangle = 1 - 2p^{\text{err}}(B_1 A_2 B_3)$ , correlations of the type  $\langle B_1 B_3 | B_1 A_2 B_3 \rangle$  are required for checking the inequality (7.18) that takes into account disturbed HVs.

### 7.5.1. Experimental limitations

There are a number of error sources contributing to imperfect state correlations, the most important being:

(i) *Wrong state assignment based on fluorescence data.* As described in chapter 4.5 we use a 250  $\mu\text{s}$  detection time to determine the state of the ion. The photon count distributions slightly overlap. Therefore, if the threshold for discriminating between the dark and the bright state is set properly the probability for wrongly assigning the quantum state is 0.3%. Making the detection period longer would reduce this error but increase errors related to decoherence of the other ion's quantum state that is not measured.

(ii) *Imperfect optical pumping.* During fluorescence detection, the ion leaves the computational subspace  $\{|0\rangle, |1\rangle\}$  if it was in state  $|1\rangle$  and can also populate the state  $|S_{1/2}, m_S = -1/2\rangle$ . To prevent this leakage, the ion is briefly pumped on the  $S_{1/2} \leftrightarrow P_{1/2}$  transition with  $\sigma_+$ -circularly polarized light to pump the population back to  $|1\rangle$ . Due to imperfectly set polarization and misalignment of the pumping beam with respect to the quantization axis, this pumping step fails with a probability of about 0.5%.

(iii) *Interactions with the environment.* Due to the non-zero differential Zeeman shift of the ion's states used for storing quantum information, superposition states dephase in the presence of slowly fluctuating magnetic fields. In particular, while measuring one ion by fluorescence detection, quantum information stored in the other ion dephases. We partially compensate for this effect by spin-echo-like techniques [23] that are based on a transient storage of superposition states in a pair of states having an opposite differential Zeeman shift as compared to the states  $|0\rangle$  and  $|1\rangle$ <sup>1</sup>. A second interaction to be taken into account is spontaneous decay of the metastable state  $|0\rangle$  which however only contributes an error of smaller than 0.1%.

(iv) *Imperfect unitary operations.* The mapping operations are not error-free. This concerns in particular the entangling gate operations needed for mapping the eigenstate subspace of a spin correlation  $\sigma_i \otimes \sigma_j$  onto the corresponding subspaces of  $\sigma_z \otimes I$ . For this purpose, a Mølmer-Sørensen gate operation  $U^{MS}(\pi/2, \phi)$  is used. This gate operation has the crucial property of requiring the ions only to be cooled into the Lamb-Dicke regime. In the experiments, the center-of-mass mode used for mediating the gate interaction is in a thermal state with an average of 18 vibrational quanta. In this regime, the gate operation is capable of mapping  $|11\rangle$  onto a state  $|00\rangle + e^{i\phi}|11\rangle$  with a fidelity of about 98% (see chapter 6.1). Taking this fidelity as being indicative of the gate fidelity, one might expect errors of about 4% in each measurement of spin correlations  $\sigma_i \otimes \sigma_j$  as the gate is carried out twice, once before and once after the fluorescence measurement.

These error sources prevented us from testing a generalization of inequality (7.5). A measurement of the correlations  $\langle B_1 B_3 | B_1 A_2 B_3 \rangle$  and  $\langle C_1 C_4 | C_1 A_2 B_3 C_4 \rangle$  resulted in error terms  $p^{\text{err}}$  that were about 0.06 for sequences involving three measurements and about 0.1 for sequences with four measurements, i. e. more than twice as big as required for observing a violation of (7.5).

<sup>1</sup>The state of the ion not to be measured is stored in a superposition of  $D_{5/2}, m = 3/2$  and  $D_{5/2}, m = 5/2$  during the detection. After remapping the state to  $D_{5/2}, m = 3/2$  and  $S_{1/2}, m = 1/2$  a waiting time is implemented during which the states partially rephase.

---

## 8. Quantum simulation of the Dirac equation

Quantum simulation aims at simulating a quantum system using a controllable laboratory system with the same underlying mathematical model. In this way, it is possible to simulate quantum systems that can neither be efficiently simulated on a classical computer [2] nor easily accessed experimentally, while allowing parameter tunability over a wide range.

Here, a proof-of-principle quantum simulation of the one-dimensional Dirac equation using a single trapped ion [117] is demonstrated. The ion is set to behave as a free relativistic quantum particle. The particle position was measured as a function of time and *Zitterbewegung* was studied for different initial superpositions of positive and negative energy spinor states, as well as the cross-over from relativistic to nonrelativistic dynamics. The high level of control of trapped-ion experimental parameters makes it possible to simulate elegantly textbook examples of relativistic quantum physics.

### 8.1. Introduction

The difficulties in observing real quantum relativistic effects have sparked significant interest in performing quantum simulations of their dynamics. Examples include black holes in Bose-Einstein condensates [163], and *Zitterbewegung* for massive fermions in solid state physics [164] none of which have been experimentally realized so far. Graphene is studied widely in connection to the Dirac equation [165–167].

The Dirac equation is a cornerstone in the history of physics [168], merging successfully quantum mechanics with special relativity, providing a natural description of the electron spin and predicting the existence of anti-matter [169]. Furthermore, it is able to reproduce accurately the spectrum of the hydrogen atom and its realm, relativistic quantum mechanics, is considered as the natural transition to quantum field theory. However, the Dirac equation also predicts some peculiar effects such as Klein’s paradox [170] and *Zitterbewegung*, an unexpected quivering motion of a free relativistic quantum particle first examined by Schrödinger [171]. These and other predictions would be difficult to observe in real particles, while constituting key fundamental examples to understand relativistic quantum effects. Recent years have seen an increased interest in simulations of relativistic quantum effects in different physical setups [117, 163, 164, 172–175], where parameter tunability allows accessibility to different physical regimes.

Trapped ions are particularly interesting for the purpose of quantum simulation [176–178], as they allow for exceptional control of experimental parameters, and initialization and read-out can be achieved with high fidelity. Recently, for example, a proof-of-principle simulation of a

quantum magnet has been performed [63] using trapped ions. The full three-dimensional Dirac equation Hamiltonian can be simulated with lasers coupling to the three vibrational eigenmodes and the internal states of a single trapped ion [117]. The setup can be significantly simplified when simulating the Dirac equation in 1+1 dimensions.

## 8.2. The Dirac equation

This section closely follows reference [179] to explain the effects observed in the experiment. The Dirac equation for a spin-1/2 particle with rest mass  $m$  is given by

$$i\hbar \frac{\partial \psi}{\partial t} = (c \boldsymbol{\alpha} \cdot \hat{\mathbf{p}} + \beta mc^2) \psi. \quad (8.1)$$

Here  $c$  is the speed of light,  $\hat{\mathbf{p}}$  is the momentum operator,  $\boldsymbol{\alpha}$  and  $\beta$  are the Dirac matrices, which are usually given in terms of the Pauli matrices  $\sigma_i$  [168] and the Identity  $I_2$  (as defined in chapter 2.1.2)

$$\alpha_i = \begin{pmatrix} 0 & \sigma_i \\ \sigma_i & 0 \end{pmatrix}, \quad \beta = \begin{pmatrix} I_2 & 0 \\ 0 & -I_2 \end{pmatrix}. \quad (8.2)$$

Each of the entries in these matrices is again a 2 x 2 matrix with  $i = x, y, z$  for the three components of the momentum operator. The wave functions  $\psi$  are 4-component spinors related on one hand to the spin of the particle and on the other hand to positive and negative energy solutions. The original idea by Dirac was that the negative energy states correspond to anti-particles while positive energy states correspond to the particle. The problem with this interpretation is that by radiative interaction positive energy states could be transformed into negative energy states and atoms would not be stable. Again Dirac proposed a possible solution [180]. All negative energy states are filled such that no transition is possible due to the Pauli exclusion principle. If one of these negative energy electrons is excited it will leave a hole in this sea of particles with a positive charge representing the anti particle. This interpretation has to be handled with care as a number of problems appear. The ground state has an infinitely high negative energy. There is an asymmetry between particles and anti-particles and we have a multi particle system. A complete solution of these problems is only achieved by using a full quantum electro-dynamics theory.

To describe the realized experiment we restrict ourselves to the 1+1 dimensional case of the Dirac equation

$$i\hbar \frac{\partial \psi}{\partial t} = H_D \psi = (c \hat{p} \sigma_x + mc^2 \sigma_z) \psi. \quad (8.3)$$

This restriction does not affect the appearance of the most stunning effects of the Dirac equation, such as *Zitterbewegung* and the Klein paradox. The two components of the spinor in 1+1 dimension do not describe the spin as in one dimension all magnetic fields are pure gauge fields [179] and spin does not exist. They rather represent the appearance of positive and negative energy states

$$\Psi(x, t) = \begin{pmatrix} \Psi_1(x, t) \\ \Psi_2(x, t) \end{pmatrix}. \quad (8.4)$$

## 8.2 The Dirac equation

---

For a further investigation the Dirac Hamiltonian is rewritten in matrix form

$$H_D = \begin{pmatrix} mc^2 & c\hat{p} \\ c\hat{p} & -mc^2 \end{pmatrix}. \quad (8.5)$$

This matrix has two eigenvalues  $E(p) = \pm\sqrt{p^2c^2 + m^2c^4}$  so there are two types of plane wave solutions to the Dirac equation  $u_{\pm}(p; x, t)$

$$u_{\pm}(p; x, t) = \frac{1}{\sqrt{2\pi}} u_{\pm}(p) e^{ipx/\hbar \mp iE(p)/\hbar t} \quad (8.6)$$

with  $u_{\pm}$  the eigenvectors to the respective eigenvalues  $E(p)$ . As a solution for the Dirac equation we hence have plane waves with positive and negative energy

$$H_D u_{\pm}(p; x, t) = \pm E(p) u_{\pm}(p; x, t). \quad (8.7)$$

To account for a real physical situation, that is to find the particle between  $x = +\infty$  and  $x = -\infty$  with probability 1, we have to demand that the integral

$$\int_{-\infty}^{+\infty} (|\Psi_1(x, t)|^2 + |\Psi_2(x, t)|^2) dx = 1 \quad (8.8)$$

is equal to one. The same argument holds for the Fourier transformed spinors  $\hat{\Psi}_{1,2}(p, t) = \mathfrak{F}(\hat{\Psi}_{1,2}(x, t))$  reflecting the momentum distribution. The unitary time evolution of the Dirac equation guarantees that the normalization of the Dirac spinor is time-independent. One has to note though, that this is not necessarily true for the individual components  $\Psi_{1,2}$ . What holds true is, that if there is a particle at the beginning there will be a particle in the end. The Dirac equation cannot describe particle creation or annihilation.

Square-integrable wave packets can be obtained by superposition of plane waves

$$\Psi(x, t) = \int_{-\infty}^{+\infty} (\hat{\Psi}_+(p) u_+(p; x, t) + \hat{\Psi}_-(p) u_-(p; x, t)) dp. \quad (8.9)$$

The coefficient functions  $\hat{\Psi}_{\pm}(p)$  can be obtained by a projection of  $\Psi(p, 0)$  onto the positive and negative energy subspace

$$\hat{\Psi}_{\pm}(p) = P^{\pm}(p) \Psi(p, 0). \quad (8.10)$$

$\Psi(p, 0)$  is obtained by Fourier transforming the initial wave function  $\Psi(x, 0)$ . In momentum space, the projection operators are given by

$$P^{\pm}(p) = \frac{1}{2} \left( I_2 \pm \frac{c\hat{p}\sigma_x + mc^2\sigma_z}{\sqrt{c^2\hat{p}^2 + m^2c^4}} \right). \quad (8.11)$$

Note that in general the projection operators do not project onto the spinor basis states except for the case where  $p = 0$ . Only in this case the projector (8.11) becomes diagonal in the spinor basis.

In the Dirac equation in 1+1 dimensions, as given in equation (8.3), there is only one motional degree of freedom and the spinor is encoded in two internal levels, related to positive and negative

energy states [117]. The velocity of the free Dirac particle is given by

$$d\hat{x}/dt = [\hat{x}, H_D]/i\hbar = c\sigma_x \quad (8.12)$$

in the Heisenberg picture. For a massless particle  $[\sigma_x, H_D] = 0$  and hence  $\sigma_x$  is a constant of motion. For a massive particle  $[\sigma_x, H_D] \neq 0$ , and the evolution of the particle is described by [171]

$$\hat{x}(t) = \hat{x}(0) + \hat{p}c^2 H_D^{-1}t + i\hat{\xi}(e^{2iH_D t/\hbar} - 1), \quad (8.13)$$

with  $\hat{\xi} = \frac{1}{2}\hbar c(\sigma_x - \hat{p}cH_D^{-1})H_D^{-1}$ . The first two terms represent an evolution linear in time, as expected for a free particle, while the last oscillating term may induce *Zitterbewegung*.

*Zitterbewegung* is understood as an interference effect between the positive and negative energy parts of the spinor and does not appear for spinors that consist entirely out of positive (or negative) energy. Furthermore, it is only present when these parts have significant overlap in position and momentum space and is therefore not a sustained effect under most circumstances [168]. For a free electron, the Dirac equation predicts the *Zitterbewegung* to have an amplitude of the order of the Compton wavelength  $R_{ZB} \sim 10^{-12}$  m and a frequency of  $\omega_{ZB} \sim 10^{21}$  Hz and has so far been experimentally inaccessible. The real existence of *Zitterbewegung*, in relativistic quantum mechanics and in quantum field theory, has been a recurrent subject of discussion in the last years [181, 182].

Note that a particle consisting of positive and negative energy states can have zero average momentum but a non-zero average velocity. The average velocity of a wave packet is given by the operator known from classical relativistic mechanics (see equation (8.13))

$$\hat{v}_{CL}(p) = c^2 \hat{p} H_D^{-1}. \quad (8.14)$$

This relation depends on the sign of the energy. For a wave packet with negative energy, a negative momentum corresponds to a positive velocity. Thus for an equal superposition of positive and negative energy states it is possible that the respective average momenta cancel while the average velocities are the same. Exactly this situation is simulated in figure 8.1 of the following chapter.

### 8.3. Experimental realization

For the simulation, a single  $^{40}\text{Ca}^+$  ion is trapped in a linear Paul trap [76] with trapping frequencies  $\omega_{ax} = 2\pi \times 1.36$  MHz axially and  $\omega_{rad} = 2\pi \times 3$  MHz in the radial directions. Doppler cooling, optical pumping, and resolved sideband cooling on the  $S_{1/2} \leftrightarrow D_{5/2}$  transition in a magnetic field of 4 G prepare the ion in the axial motional ground state and in the internal state  $|S_{1/2}, m = 1/2\rangle$ . A narrow linewidth laser at 729 nm couples the states  $\binom{0}{1} := |S_{1/2}, m = 1/2\rangle$  and  $\binom{1}{0} := |D_{5/2}, m = 3/2\rangle$  which we identify as our spinor states. A bichromatic light field resonant with the upper and lower axial motional sidebands of the  $\binom{1}{0} \leftrightarrow \binom{0}{1}$  transition with appropriately set phases [183] realizes the first part, proportional to  $\sigma_x \hat{p}$ , of the Hamiltonian (see chapter 3.6)

$$H_D = 2\eta\Delta\tilde{\Omega}\sigma_x\hat{p} + \hbar\Omega\sigma_z. \quad (8.15)$$

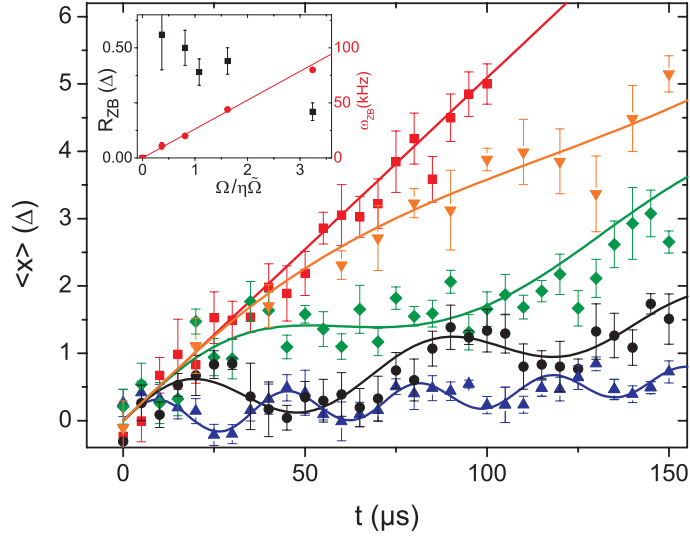


**Figure 8.1.:** Expectation values  $\langle \hat{x}(t) \rangle$  for particles with different masses. The linear curve (■) represents a massless particle ( $\Omega = 0$ ) moving with the speed of light given by  $c = 2\eta\tilde{\Omega}\Delta = 0.052 \Delta/\mu\text{s}$  for all curves. The other curves are for particles with increasing mass moving down from the linear curve. Their Compton wavelengths are given by  $\lambda_C := 2\eta\tilde{\Omega}\Delta/\Omega = 5.4\Delta$  (▼),  $2.5\Delta$  (◆),  $1.2\Delta$  (●) and  $0.6\Delta$  (▲), respectively. The solid curves represent numerical simulations. The figure shows *Zitterbewegung* for the crossover from the relativistic  $2\eta\tilde{\Omega} \gg \Omega$  to the nonrelativistic limit  $2\eta\tilde{\Omega} \ll \Omega$ . The inset shows fitted *Zitterbewegung* amplitude  $R_{ZB}$  (■) and frequency  $\omega_{ZB}$  (●) versus the parameter  $\Omega/\eta\tilde{\Omega}$  (which is proportional to the mass). Error bars are  $1\sigma$ .

The component proportional to  $\sigma_z$  (equivalent to a light shift) is achieved by detuning the red and blue light field by  $\Omega$  from resonance<sup>1</sup>.  $\Delta = \sqrt{\hbar/2\tilde{m}\omega_{ax}}$  is the size of the ground-state wave function with  $\tilde{m}$  the ion's mass, not to be confused with the mass  $m$  of the simulated particle,  $\eta = 0.06$  is the Lamb-Dicke parameter,  $\hat{p} = \frac{a^\dagger - a}{2i} \frac{\hbar}{\Delta}$  is the momentum operator and  $a^\dagger$  and  $a$  are the usual raising and lowering operators for the motional state along the axial direction. The first term in equation 8.15 describes a state-dependent motional excitation with coupling strength  $\eta\tilde{\Omega}$ , corresponding to a displacement of the ion's wave packet in the harmonic trap. The parameter  $\tilde{\Omega}$  is controlled by setting the intensity of the bichromatic light field. The second term is equivalent to an optical Stark shift and arises when the bichromatic light field is detuned from resonance by  $2\Omega$ . Equation (8.15) reduces to the 1+1 dimensional Dirac Hamiltonian if we make the identifications  $c := 2\eta\tilde{\Omega}\Delta$  and  $mc^2 := \hbar\Omega$ . The momentum and position of the Dirac particle are then mapped onto the corresponding quadratures of the trapped ion harmonic oscillator.

In order to study relativistic effects such as *Zitterbewegung* it is necessary to measure the expectation value of the position operator  $\langle \hat{x}(t) \rangle$  of the harmonic oscillator. It has been noted theoretically that such expectation values could be measured using very short probe times, without reconstructing the full quantum state [115–117]. As pointed out in chapter 3.6.1, for measuring  $\langle \hat{x} \rangle$  of a motional state  $\rho_m$ , we have to (i) prepare the ion's internal state in an eigenstate of  $\sigma_y$ , (ii) apply a unitary transformation  $U(\tau)$  that maps information about  $\rho_m$  onto the internal states, and (iii) record the changing excitation by a fluorescence measurement [76] as a function of the probe time

<sup>1</sup>Both light fields are detuned in the same direction unlike a Mølmer-Sørensen interaction.

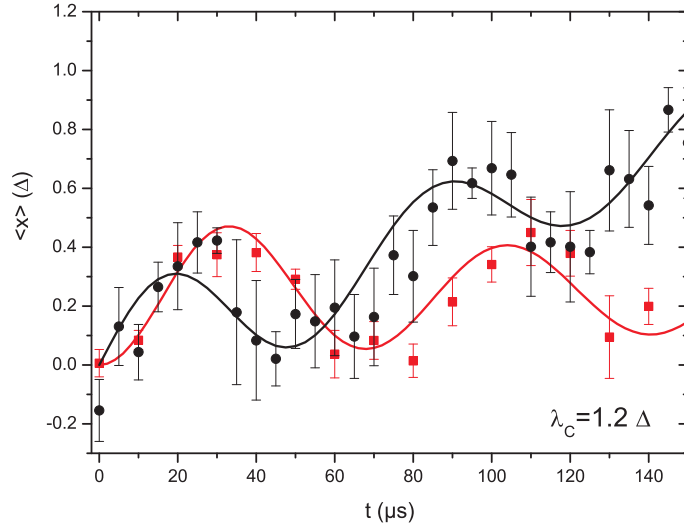


**Figure 8.2.:** Evolution of the expectation value  $\langle \hat{x}(t) \rangle$  for particles with mass  $\lambda_c = 1.2\Delta$  and an electronic state which is an eigenstate of  $\sigma_x$  ( $\bullet$ ) (data taken from figure 8.1) or an eigenstate of  $\sigma_y$  ( $\blacksquare$ ). *Zitterbewegung* appears again due to interference of positive and negative energy parts of the state. Even though the simulated particles have the same mass their behavior is completely different. For the  $\sigma_y$  eigenstate the initial velocity is zero (see equation 8.12) whereas the particle in an eigenstate of  $\sigma_x$  has an initial velocity equal to the speed of light. The solid curve represents a numerical simulation. Error bars are  $1\sigma$ .

$\tau$  (see chapter 3.6.1). In this protocol, the unitary operator  $U(\tau) = \exp(-i\eta\Omega_p\sigma_x\hat{x}\tau/\Delta)$ , with  $\hat{x} = (a^\dagger + a)\Delta$  and probe Rabi frequency  $\Omega_p$ , effectively transforms the observable  $\sigma_z$  into  $\sin k\hat{x}$ , with  $k = 2\eta\Omega_p\tau/\Delta$ , so that  $\langle \hat{x} \rangle$  can be determined by monitoring the rate of change of  $\langle \sin k\hat{x} \rangle$  for short probe times (see chapter 3.6.1). Since the Dirac Hamiltonian generally entangles the motional and internal state of the ion, we first incoherently recombine the internal state population in  $\binom{0}{1}$  before proceeding to (i).<sup>2</sup> Then, we apply the Hamiltonian generating  $U$  with the probe Rabi frequency set to  $\Omega_p = 2\pi \times 13$  kHz and for interaction times  $\tau$  of up to  $14 \mu\text{s}$ , with  $1\text{-}2 \mu\text{s}$  steps. The change of excitation was obtained by a linear fit each based on  $10^4$  to  $3 \cdot 10^4$  measurements.

We simulate the Dirac equation by applying  $H_D$  for varying amounts of time and for different particle masses. In the experiment we set  $\tilde{\Omega} = 2\pi \times 68$  kHz, corresponding to a simulated speed of light  $c = 0.052 \Delta/\mu\text{s}$ . The measured expectation values  $\langle \hat{x}(t) \rangle$  are shown in figure 8.1 for a particle initially prepared in the spinor state  $\psi(x; t=0) = (\sqrt{2\pi}2\Delta)^{-\frac{1}{2}} e^{-\frac{x^2}{4\Delta^2}} \binom{1}{1}$  by sideband cooling and application of a  $\pi/2$ -pulse. *Zitterbewegung* appears for particles with non-zero mass, obtained by varying  $\Omega$  in the range of  $0 < \Omega \leq 2\pi \times 13$  kHz by changing the detuning of the bichromatic lasers.

We investigate the particle dynamics in the cross-over from relativistic to nonrelativistic dynamics. The data in figure (8.1) match well with numerical simulations based on the Hamiltonian (8.15)

<sup>2</sup>This is done by first shelving the population initially in  $\binom{0}{1}$  to  $|D_{5/2}, m=5/2\rangle$  using a Rapid Adiabatic Passage transfer (RAP). A second RAP transfers the population in  $\binom{1}{0}$  to  $\binom{0}{1}$ . A  $100 \mu\text{s}$  laser pulse at  $854 \text{ nm}$  transfers the population in  $|D_{5/2}, m=5/2\rangle$  to  $|P_{3/2}, m=3/2\rangle$  from which it spontaneously decays to  $\binom{0}{1}$ . The transfer efficiency is  $> 99\%$ , limited by the small branching ratio to the  $D_{3/2}$  state. In the transfer steps a probability exists that the motional state of the ion is changed. This probability is however very small due to the small Lamb-Dicke parameter but could be eliminated completely by a separate measurement of the motional states of the spinor states  $\binom{0}{1}$  and  $\binom{1}{0}$ , at the expense of a longer data acquisition time.

### 8.3 Experimental realization

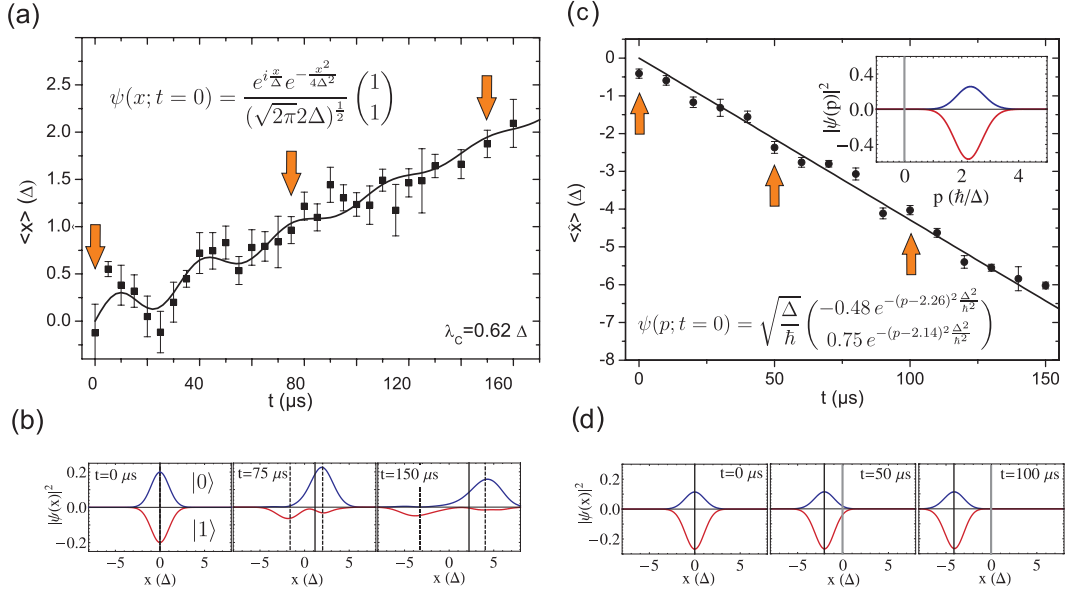


**Figure 8.3:** (a) *Zitterbewegung* for a state with non-zero average momentum. Initially, *Zitterbewegung* appears due to interference of positive and negative energy parts of the state. As these parts separate, the oscillatory motion fades away. The solid curve represents a numerical simulation. (b) Numerically calculated probability distributions  $|\psi(x)|^2$  at the times  $t = 0, 75$  and  $150 \mu\text{s}$  (as indicated by the arrows in (a)). The probability distribution corresponding to the state  $\begin{pmatrix} 0 \\ 1 \end{pmatrix}$  is inverted for clarity. The vertical solid line represents  $\langle \hat{x} \rangle$  as plotted in (a). The two dashed lines are the expectation values for the positive and negative energy parts of the spinor. (c) Time evolution for a negative energy eigenstate with  $\lambda_C = 1.2\Delta$ . Laser pulses create a negative energy spinor with average momentum  $\langle \hat{p} \rangle = 2.2\hbar/\Delta$ . The corresponding initial momentum distribution  $|\tilde{\psi}(p)|^2$  is shown in the inset. The solid lines represent a numerical calculation. The curve in (c) shows no *Zitterbewegung*. (d) Simulated probability distributions  $|\psi(x)|^2$  for three different evolution times are shown (as indicated by the arrows in (c)). Error bars are  $1\sigma$ .

shown as solid lines. The error bars are obtained from a linear fit assuming quantum projection noise which dominates over noise caused by fluctuations of control parameters. In addition, the data were fitted with a heuristic model function of the form  $\langle \hat{x}(t) \rangle = at + R_{ZB} \sin \omega_{ZB} t$  to extract the effective amplitude  $R_{ZB}$  and frequency  $\omega_{ZB}$  of the *Zitterbewegung* shown in the inset. As the particle's initial momentum is not dispersion-free, the amplitude and frequency are only approximate concepts. From these data it can be seen that the frequency grows linearly with increasing mass  $\omega_{ZB} \approx 2\Omega$ , whereas the amplitude decreases as the mass is increased. Since the mass of the particle is increased but the momentum and the simulated speed of light remain constant, the data in figure (8.1) show the crossover from the far relativistic to nonrelativistic limits. Hence, the data confirm that *Zitterbewegung* vanishes in both limits, as theoretically expected. In the far relativistic case this is because  $\omega_{ZB}$  goes to zero, and in the nonrelativistic case because  $R_{ZB}$  vanishes.

The tools used for simulating the Dirac equation can also be applied to precisely set the initial state of the simulated particle. A first simple change is to prepare an electronic eigenstate of  $\sigma_y$ . The wave function of the particle is given by  $\psi(x; t=0) = (\sqrt{2\pi}2\Delta)^{-\frac{1}{2}} e^{-\frac{x^2}{4\Delta^2}} \begin{pmatrix} 1 \\ i \end{pmatrix}$ . The evolution of

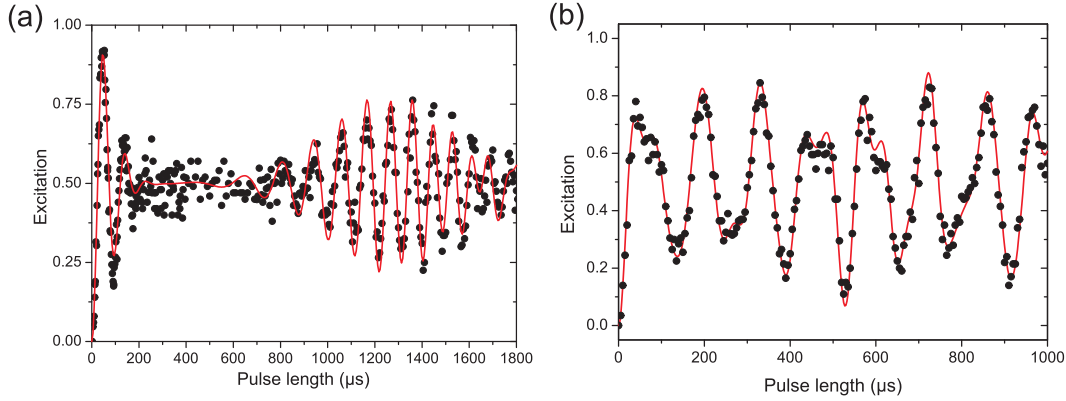


**Figure 8.4.:** (a) Blue sideband oscillations after a  $100 \mu\text{s}$  application of Hamiltonian (8.15) with  $\Omega = 0$  and  $\tilde{\Omega} = 2\pi \times 68 \text{ kHz}$  demonstrating the coherence of the displacement. The oscillations for the coherent state with  $\langle n \rangle = 6.3$  die out quickly and revive after  $500 \mu\text{s}$ . The solid line was obtained by simulating the phonon distribution and coherently adding the individual state evolutions. (b) Blue sideband oscillations for the same parameters except  $\lambda_c = 1.2\Delta$ . The solid line was again obtained by simulating the phonon distribution and coherently adding the individual state evolutions.

the expectation values  $\langle x \rangle$  shown in figure 8.2 for particles with equal mass  $\lambda_c = 1.2\Delta$  but different electronic state is quite different. The particle initially in an eigenstate of  $\sigma_y$  has zero velocity at  $t=0$  (see equation (8.12)) whereas the particle in an eigenstate of  $\sigma_x$  has an initial velocity equal to the speed of light.

The particle in figure 8.3a was given an average initial momentum  $\langle \hat{p}(t=0) \rangle = \hbar/\Delta$  by a displacement operation with the Hamiltonian  $H = \hbar\eta\tilde{\Omega}\sigma_x\hat{x}/\Delta$ . The initial state of this particle is built up out of a positive energy component with positive velocity and a negative energy component with negative velocity[179]. The positive energy component moves to the right and both spinor states can be seen to contribute to this part (see appendix B.1), the negative component moves to the left. As long as these parts overlap, *Zitterbewegung* is observed which dies out as the parts separate. For an additional illustration how the vanishing of the *Zitterbewegung* comes about the evolution of the probability distributions are shown in figure 8.3 b. The solid lines are obtained by numerical simulations. The probability distribution corresponding to the state  $\binom{0}{1}$  is inverted for clarity.

It is also possible to initialize the spinor in a pure negative or positive energy state (see appendix B.1). In figure 8.3 c, the time evolution  $\langle \hat{x}(t) \rangle$  of a negative energy spinor with average momentum  $\langle \hat{p} \rangle = 2.2\hbar/\Delta$  is shown. The corresponding simulated probability distributions are displayed in figure 8.3 d and it can be seen that there is indeed no *Zitterbewegung* or splitting of the wave function which arises only if there are positive and negative energy contributions to the wave function.

An additional test to compare experimentally obtained states with theory can be performed by an excitation on the blue sideband after recombining the internal state population. An excitation on the blue sideband will lead to oscillations that die out quickly but revive after some time due to an interference of the coherently populated states  $|\downarrow, n\rangle$ . This interference occurs because all phonon states are excited from the  $S_{1/2}$  ground state to the  $D_{5/2}$  excited state at the same

### 8.3 Experimental realization

---

time however their Rabi frequency is different. The populations will thus oscillate at different frequencies between ground and excited state and the sum of these oscillations is quickly decaying. Figure 8.4 (a) shows oscillations on the blue sideband after a  $100 \mu\text{s}$  application of Hamiltonian 8.15 acting on the initial spinor state  $\psi(x; t = 0) = (\sqrt{2\pi}2\Delta)^{-\frac{1}{2}} e^{-\frac{x^2}{4\Delta^2}} \begin{pmatrix} 1 \\ 1 \end{pmatrix}$ . The parameters in the Hamiltonian were set to  $\Omega = 0$  and  $\tilde{\Omega} = 2\pi \times 68 \text{ kHz}$ . The displacement created a coherent state with  $\langle n \rangle = 6.3$  corresponding to  $\alpha = 2.5$ . Similar curves have already been observed in David Winelands group [184]. Figure 8.4 (b) shows blue sideband oscillations for the same initial state and parameters, except  $\Omega = 2\pi \times 7 \text{ kHz}$ . The solid lines in both figures were obtained by simulating the phonon distribution and summing over it,

$$\rho_{DD}(t) = \sum_{n=0}^{\infty} p_n \sin^2(\Omega_{n,n+1}t), \quad (8.16)$$

with  $\Omega_{n,n+1}$  the Rabi frequency for coupling the motional states  $n$  and  $n+1$  and  $p_n$  the occupation probability of the motional state  $|n\rangle$ .



---

## 9. Summary and Outlook

The main results of this thesis can be divided into three topics: QIP with  $^{40}\text{Ca}^+$  and  $^{43}\text{Ca}^+$  ions realizing high fidelity entangling operations, a test of a hidden variable theory where the test procedure relies on QIP techniques and finally the quantum simulation of the Dirac equation. All experiments encode the quantum information in Zeeman levels of the  $S_{1/2}$  ground state and the meta-stable  $D_{5/2}$  state of calcium ions.

An entangling gate operation is necessary to meet the DiVincenzo criteria to realize a quantum computer. For this purpose a Mølmer-Sørensen entangling operation was implemented creating Bell states with  $^{40}\text{Ca}^+$  ions with a fidelity of 99.3%. Assuming that the Bell state fidelity is a good measure for the gate-operation, the errors are in principle low enough to be in the fault tolerant regime, although the overhead in the number of qubits is enormous. A detailed experimental investigation of the gate mechanism identified possible error sources. The high quality of the gate operation allowed for concatenations of up to 21 individual gate-operations. Furthermore it was shown for the first time, that this kind of gate operation does not depend on ground state cooling. Bell states with a fidelity of 98.4(2)% were realized with ions cooled to a thermal state with a mean vibrational quantum number  $\langle n \rangle = 18(2)$ .

Implementing the gate operation with three ions was the next obvious step. GHZ states were created with a fidelity of 97.9(2)%. This is so far the highest achieved fidelity for a three ion GHZ state. By using an off-resonant tightly focused beam a selective entanglement of two out of three ions was achieved. The off-resonant beam was used to switch on and off the Mølmer-Sørensen interaction on each qubit individually. This scheme is an important building block for realizing NMR like techniques in ion traps. The ideas developed in Volckmar Nebendahls [150] thesis promise simple algorithms realizing e.g. error correction with 9 pulses or a Toffoli gate with 11 pulses.

The knowledge gained with  $^{40}\text{Ca}^+$  was transferred to the more complicated level structure of  $^{43}\text{Ca}^+$ . A clever choice of polarization and geometrical dependencies helped to suppress the coupling strength of unwanted transitions. This paved the way to create entangled states using  $^{43}\text{Ca}^+$  ions with a fidelity of 96.9(3)% despite the presence of spectator states. To protect the susceptible quantum state against magnetic field fluctuations it was mapped onto the hyperfine clock state of  $^{43}\text{Ca}^+$ . The mapping pulses work with a fidelity of better than 99% such that the fidelity of the Bell state encoded in the hyperfine qubits was 96.7%. After a storage time of 20 ms the state was mapped back to the optical qubit and two additional entangling operations were applied. The fidelity after this sequence was still 87.8%. This result demonstrates the combination of a high fidelity gate operation on an optical qubit with the long coherence times of a hyperfine qubit in a single realization.

The improvements that have to be incorporated for future QIP experiments are manifold. One

of the main goals is to unify all building blocks: high fidelity gates, long coherence times, high fidelity state initialization and read out, in one scalable system. The focus of current technology development will lie on micro-fabricated traps that provide an environment for ions suitable to do QIP. Along this development progress has to be made on many aspects. All techniques have to be modified such that they work reliably on a bigger number of ions at the same time. All experimental parameters have to be controlled with higher precision e.g. laser intensity, trap frequencies and magnetic field. Achieving this control of parameters is quite challenging. It might be more fruitful to develop and improve alternative methods like coherent control [185] or an encoding in decoherence free subspaces [52] that are more robust against parameter fluctuations.

As it turned out, ion trap systems are a good test bed for fundamental questions in quantum physics or rather hidden variable theories. For this purpose measurements of the form  $\sigma_i \otimes \sigma_i$  were realized by mapping the state of two qubits on a single qubit prior to the fluorescence measurement. The non-demolition measurement was completed by a second operation mapping the state projected on  $|\uparrow\rangle$  or  $|\downarrow\rangle$  onto an eigenstate of the measurement. This technique allowed us to do a series of quantum non-demolition measurements on a single quantum state. The investigated high fidelity entangling gate working on thermal ions was a necessary prerequisite for this task. This measurement technique was the key ingredient to do, for the first time, a state-independent experimental test of the Kochen Specker theorem. A violation of the Kochen Specker inequality was found with  $\langle \mathcal{X}_{KS} \rangle = 5.46(4) > 4$  indicating that hidden variable theories cannot explain the observed effects. The theory predicts that this violation will be found for all possible quantum states. This prediction was tested by performing the same measurements on 10 different input states, finding a violation for all states. A possible loophole, incompatibility of measurements, was closed by carefully evaluating possible error sources and including them in a refined theory. We found that quantum mechanics violates a CHSH like inequality including the errors such that  $\langle \mathcal{X}_{DHV} \rangle = 2.23(5) > 2$ . For a violation of the original Kochen Specker inequality incorporating imperfect measurements the errors of the mapping operations have to be improved by more than a factor of two.

Due to the huge success of ion traps with QIP one tends to forget that an ion trap is “the“ model system for a quantum harmonic oscillator. In QIP applications it serves as a mere mediator to couple different ions, not exploiting the full available Hilbert space. In this thesis the harmonic oscillator was utilized to realize a simulation of the Dirac equation. Momentum and position of a free Dirac particle were mapped onto the respective observables of the trapped ion harmonic oscillator. The exact Dirac Hamiltonian was implemented and effects like *Zitterbewegung* could be measured. A new method was used to determine the average position of the wave packets. The amount of control of the system allowed for a preparation of specific states where the form of the *Zitterbewegung* is changed, *Zitterbewegung* dies out or does not occur at all.

As it turned out the observable  $A(t) = \cos(2\eta\Omega_p t/\Delta\hat{x})\sigma_z + \sin(2\eta\Omega_p t/\Delta\hat{x})\sigma_y$  used for measuring  $\langle \hat{x} \rangle$  can be adopted to reconstruct the probability distribution of the wave function [78, 186]. This possibility increases the information about the evolution of the system. It nicely visualizes the splitting of the wave packet and will be a valuable tool for future simulations.

Possible extensions of the Dirac equation simulation are to add more spatial dimensions or to incorporate potentials to simulate e.g. Klein’s paradox. An interesting example is a Dirac particle

---

on a slope. The Hamiltonian in 1+1 dimensions reads as

$$H_{pot} = c\hat{p}\sigma_x + mc^2\sigma_z + ca\hat{x}I = H_D + ca\hat{x}I. \quad (9.1)$$

The additional potential  $ca\hat{x}$  could be realized with a second ion in the trap.  $H_D$  will be implemented with the first ion using the very same light fields as already demonstrated. A displacement operator on the second ion working on different electronic levels but on the same motional mode creates the desired potential. All that is needed in addition to the presented work is a second bichromatic light field tuned to a different transition. Simulations suggest that a particle running up this slope could tunnel through the potential by switching to the negative energy eigenstate. This eigenstate sees an inverted slope and is thus accelerated away from the turning point into the classically forbidden region. This effect corresponds to Klein's paradox. Another proposal that could be simulated using similar interactions is the 2+1 dimensional Dirac oscillator [172].

Several other proof of principle quantum simulation experiments have been demonstrated in the last years [63, 186, 187]. So simulations of simple quantum systems are already feasible in ion traps. Besides the already realized experiments a huge variety of quantum simulations has been proposed [178] for trapped ions. Some examples are the Unruh effect [188, 189], spin models [177], spin boson models [190], cosmological particle creation [191] and the Frenkel-Kontorova model [192]. It seems that in the near future more complicated experimental realizations with a few tens of ions are within reach. Such problems would already be hard to simulate with classical computers.



# A. The Kochen Specker measurements

## A.1. Detailed results for the Kochen Specker measurements

The measurement correlations shown in figure 7.2 are based on experiments where measurements on a total of 6,600 realizations of the quantum state  $\Psi = \frac{1}{\sqrt{2}}(|\uparrow\downarrow\rangle - |\downarrow\uparrow\rangle)$  were performed. In these experiments, the results were observed  $(v_1, v_2, v_3)$ ,  $v_i \in \{-1, +1\}$ , with the frequencies listed in the table.

Observables	$M_1$	$\sigma_z^{(1)}$	$\sigma_x^{(2)}$	$\sigma_z^{(1)} \otimes \sigma_x^{(2)}$
	$M_2$	$\sigma_z^{(2)}$	$\sigma_x^{(1)}$	$\sigma_x^{(1)} \otimes \sigma_z^{(2)}$
	$M_3$	$\sigma_z^{(1)} \otimes \sigma_z^{(2)}$	$\sigma_x^{(1)} \otimes \sigma_z^{(2)}$	$\sigma_y^{(1)} \otimes \sigma_y^{(2)}$
Measured correlations	$(-1, -1, -1)$	17	3	20
	$(+1, -1, -1)$	520	516	495
	$(-1, +1, -1)$	511	529	511
	$(+1, +1, -1)$	8	18	8
	$(-1, -1, +1)$	9	15	23
	$(+1, -1, +1)$	4	7	16
	$(-1, +1, +1)$	13	10	11
	$(+1, +1, +1)$	18	2	16
Number of experiments		1100	1100	1100

Observables	$M_1$	$\sigma_z^{(1)}$	$\sigma_z^{(2)}$	$\sigma_z^{(1)} \otimes \sigma_z^{(2)}$
	$M_2$	$\sigma_x^{(2)}$	$\sigma_x^{(1)}$	$\sigma_x^{(1)} \otimes \sigma_x^{(2)}$
	$M_3$	$\sigma_z^{(1)} \otimes \sigma_x^{(2)}$	$\sigma_x^{(1)} \otimes \sigma_z^{(2)}$	$\sigma_y^{(1)} \otimes \sigma_y^{(2)}$
Measured correlations	$(-1, -1, -1)$	11	13	1010
	$(+1, -1, -1)$	281	298	8
	$(-1, +1, -1)$	250	276	14
	$(+1, +1, -1)$	11	18	9
	$(-1, -1, +1)$	237	264	26
	$(+1, -1, +1)$	16	13	11
	$(-1, +1, +1)$	17	14	22
	$(+1, +1, +1)$	277	204	0
Number of experiments		1100	1100	1100

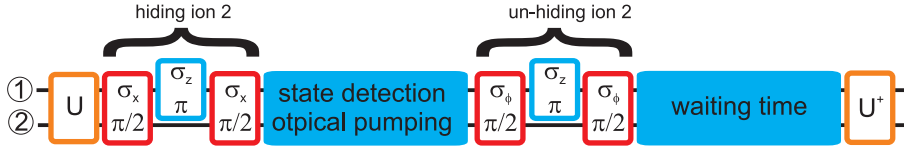


**Figure A.1.:** Sequence used in the Kochen Specker measurements to hide one ion and detect the state of the other ion. The waiting time counteracts stepwise magnetic field fluctuations.

## A.2. Hiding the second ion in the Kochen Specker measurements

The QND measurements performed in chapter 7 required the hiding of the S-state of the second ion from the fluorescence laser in the  $D_{5/2}, m_j = 5/2$  state. The hiding was done by using a pulse sequence similar to the one shown in figure 5.4(b) using an addressed AC stark pulse. The pulse sequence is given by  $U_x^{(2)}(\pi) = U_x(\frac{\pi}{2})U_z^{(1)}(\pi)U_x(\frac{\pi}{2})$ . The un-hiding after the detection is done in the same way. The phases of the two carrier pulses  $\phi$  that un-hide the ion have to be corrected for the phase difference the state  $D_{5/2}, m_j = 5/2$  acquires relative to the  $S_{1/2}, m_j = 1/2$  state. The whole pulse sequence for a Kochen Specker measurement including the detection, un-hiding and unitary transformations can be seen in figure A.1.

One problem we were facing in these measurements was a slow sometimes stepwise variation of the magnetic field. The slow variations are tracked by our automatic measurement scheme determining the magnetic field and laser drift (see chapter 5.3). If a step occurs in the magnetic field by  $\Delta B$  then the carrier pulses are off-resonant for some time until the change is detected (in the worst case this can be up to a minute). Due to the detuning the unitary operations following the un-hiding will have the wrong phase. This problem can be reduced by the waiting time in the pulse sequence.

The phase difference the qubit acquires when stored in the D-states is given by

$$\phi_{DD'} = \mu_B \cdot g_D \cdot \Delta B \cdot \Delta t \quad (\text{A.1})$$

(see equation 2.41) where  $\Delta t$  is the time needed for state detection and optical pumping. The phase the qubit acquires during the waiting time  $\Delta t'$  is given by

$$\phi_{SD} = \mu_B \cdot (g_S \cdot \frac{1}{2} - g_D \cdot \frac{3}{2}) \Delta B \cdot \Delta t'. \quad (\text{A.2})$$

The total phase the qubit acquires is thus given by  $\phi_{total} = \phi_{SD} + \phi_{DD'}$ . It turns out that this phase can be canceled by choosing

$$\Delta t' = \frac{g_D}{3/2g_D - 1/2g_S} \Delta t. \quad (\text{A.3})$$

This trick only works if the laser is more stable than the magnetic field as the length of the whole pulse sequence is increased. The best compromise in our case was achieved by choosing  $\Delta t = \Delta t'$  which results in a partial compensation of the phase.

---

## B. Methods for simulating the Dirac equation

### B.1. Constructing a pure negative energy spinor

The spinor state in figure 8.3 c was engineered backwards by projecting out the negative energy part of a wavepacket with average momentum  $\langle \hat{p} \rangle = 2.2\hbar/\Delta$  and renormalizing the spinor.

The complete sequence for approximating the negative energy state is conveniently described in the basis of the eigenstates  $|\pm\rangle_y = \frac{1}{\sqrt{2}}\begin{pmatrix} 1 \\ \pm i \end{pmatrix}$  of  $\sigma_y$ . After ground state cooling we prepare the state  $|+\rangle_y$ , then we displace this state to an average momentum state  $\langle \hat{p} \rangle = 2.2\hbar/\Delta$  by the displacement Hamiltonian  $H = \hbar\eta\tilde{\Omega}\sigma_y\hat{x}/\Delta$ . Next, a far detuned laser pulse rotates the internal state to  $0.84|+\rangle_y + i0.53|-\rangle_y$ . The displacement Hamiltonian  $H = -\hbar\eta\tilde{\Omega}\sigma_y\hat{x}/\Delta$  shifts these parts in opposite directions to create the required asymmetry between the average momenta of the components. A final  $\pi/2$ -pulse creates the state shown in figure 8.3 c. This state has  $> 99\%$  overlap with the desired negative energy state.

### B.2. Setting the phase of the Displacement pulse

Two phases  $\phi_+, \phi_-$  have to be set (see Hamiltonian 3.37) to get the right electronic and motional interaction in the displacement Hamiltonian (8.3). The sum phase  $\phi_+$  can be set by the overall phase of the light field (see figure 4.7 AO2 ). The right value in the massless case ( $\Omega = 0$ ) can be found by a simple experiment. Applying a  $U_y(\pi/2)$  pulse to the ion we create an eigenstate of  $\sigma_x$ . If we then apply Hamiltonian 8.3 with  $\Omega = 0$  the electronic state of the qubit should not change. This was confirmed by a second  $U_y(\pi/2)$  pulse completing the rotation to the excited state. By scanning the overall phase of the bichromatic light field we can find the phase value that corresponds to a  $\sigma_x$  interaction and implements the desired Hamiltonian.

In the case where  $\Omega \neq 0$  (simulation of a particle with mass) finding the right phase was a little bit more complicated. We again perform the same experiment,  $U_y(\pi/2)$  - apply  $H_D$  -  $U_y(\pi/2)$  and scan the length of the bichromatic pulse. If the phase is set correctly, we find a change of excitation as shown in figure B.1. The parameters of the displacement pulse were set to  $\tilde{\Omega} = 2\pi \times 68$  kHz and  $\Omega = 2\pi \times 13$  kHz. Comparing these data with simulations (also shown in figure B.1) we found that the right phase can be determined by varying the phase  $\phi_+$  and minimizing the excitation after a  $40 \mu s$  bichromatic pulse. The difference phase  $\phi_-$  can be set by changing the relative phases of the RF-signal generators driving AO3 (see figure 4.7). Setting the absolute value of  $\phi_-$  of the red and blue light field is not necessary as we can define our phase space such that the displacement we do is along x. To get a displacement along p we have to add an additional phase difference

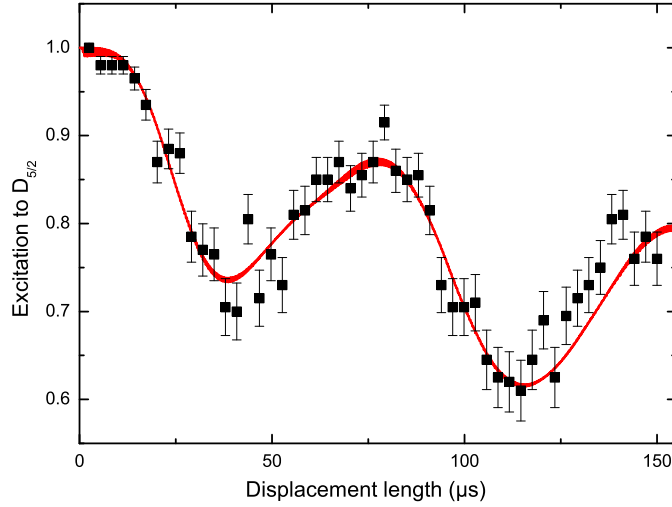


**Figure B.1.:** Excitation evolution for a pulse length scan of the bichromatic pulse in the experiment  $U_y(\pi/2) - \text{apply } H_D - U_y(\pi/2)$  ( $\bullet$ ). The parameters of the bichromatic pulse were  $\tilde{\Omega} = 2\pi \times 68$  kHz and  $\Omega = 2\pi \times 13$  kHz. Here the phase of the bichromatic pulse was set right realizing 8.3. The right phase can be determined by minimizing the excitation after a  $40 \mu\text{s}$  pulse length. The red line is a simulation based in 8.3.

of  $90^\circ$  to  $\phi_-$  while keeping the sum frequency  $\phi_+$  the same. This  $90^\circ$  phase shift of  $\phi_-$  can be achieved by introducing a switchable delay line in the RF line supplying the blue light field. At the same time we have to change the phase of the light field by  $90^\circ$  to maintain the same value for  $\phi_+$  and thus the same electronic interaction. A more sophisticated way to change the motional interaction in a continuous way from x to p can be achieved by opening up the axial confinement. When we change the trap frequency by an amount of  $\Delta$  we have to replace the operators  $a$  and  $a^\dagger$  in equation (3.38) by  $a e^{i\Delta t}$  and  $a^\dagger e^{-i\Delta t}$ . So phase space will start to rotate with respect to the unchanged laser frequency that serves as a reference oscillator. If we change the axial trapping potential by  $\Delta$ , wait for an appropriate amount of time  $t$  and switch back to the initial confinement we have rotated phase space by  $\Delta t$ .

A fast switching of the axial trap frequency was achieved with the setup used for shifting the ions (see chapter 4.1) but supplying both tips from one of the outputs of the circuit shown in figure 4.2. We can change the trap frequency by about 6 kHz which corresponds to a switching time from x to p of about  $40 \mu\text{s}$ .

## C. Physical and optical properties of Calcium

speed of light	$c$	299 792 458 m/s (exact)
permeability of vacuum	$\mu_0$	$4 \pi \cdot 10^{-7}$ (exact)
permittivity of vacuum	$\epsilon_0$	$1/(\mu_0 c^2)$ (exact)
Planck's constant	$h = 2\pi\hbar$	$6.626\ 068\ 96(33) \cdot 10^{-34}$ J s
elementary charge	$e$	$1.602\ 176\ 487(40) \cdot 10^{-19}$ C
Bohr magneton	$\mu_B$	$927.400\ 915(23) \cdot 10^{-26}$ J T <sup>-1</sup>
atomic mass unit	$u$	$1.660\ 538\ 782(83) \cdot 10^{-27}$ kg
electron mass	$m_e$	$9.109\ 382\ 15(45) \cdot 10^{-31}$ kg
fine structure constant	$\alpha$	$7.297\ 352\ 5376(50) \cdot 10^{-3}$
Boltzmann constant	$k_B$	$1.380\ 6504(24) \cdot 10^{-23}$

**Table C.1.:** Fundamental physical constants relevant to the experiment (2006 CODATA recommended values)

transition	$\lambda_{air}(nm)$	Isotope shift (MHz)	reference
$4S_{1/2} \leftrightarrow 3D_{5/2}$	411.042 129 776 393.3(1.0) THz	4134.711 720 (390)	[94, 122, 193]
$4S_{1/2} \leftrightarrow 3D_{3/2}$	732.389	4145(43)	[194]
$4S_{1/2} \leftrightarrow 4P_{1/2}$	396.847	706(42)	[194]
$4S_{1/2} \leftrightarrow 4P_{3/2}$	393.366	713(31)	[194]
$3P_{1/2} \leftrightarrow 3D_{3/2}$	866.214	-3464.3(3.0)	[100]
$3P_{3/2} \leftrightarrow 3D_{3/2}$	849.802	-3462.4(2.6)	[100]
$3P_{3/2} \leftrightarrow 3D_{5/2}$	854.209	-3465.4(3.7)	[100]

**Table C.2.:**  $^{40}\text{Ca}^+$  wavelength in air ( $\lambda_{air}$ ) and the corresponding isotope shifts (IS) between  $^{40}\text{Ca}^+$  and  $^{43}\text{Ca}^+$ . The transition frequency for  $4S_{1/2} \leftrightarrow 3D_{5/2}$  is given in THz.

quantity	value	reference
life time $3D_{3/2}$	1.20(1) s	[96]
life time $3D_{5/2}$	1.168(7) s	[96]
life time $4P_{1/2}$	7.098(20) ns	[97]
life time $4P_{3/2}$	6.924(19) ns	[97]
$g_j(4S_{1/2})$	2.00225664(9)	[195]
$g_j(3D_{5/2})$	1.200 334 0(3)	[122, 193]

**Table C.3.:** Atomic properties of calcium

$m'$	-3/2	-1/2	1/2	3/2	5/2
coefficient	$\sqrt{1/5}$	$\sqrt{2/5}$	$\sqrt{3/5}$	$\sqrt{4/5}$	1

**Table C.4.:** Clebsch Gordan Coefficients for the  $^{40}\text{Ca}^+$  quadrupole transition  $S_{1/2}, m = 1/2 \rightarrow D_{5/2}, m'$ . The coupling strength for  $S_{1/2}, m = -1/2 \rightarrow D_{5/2}, m'$  can be derived by exchanging  $m'_j \rightarrow -m'_j$ .

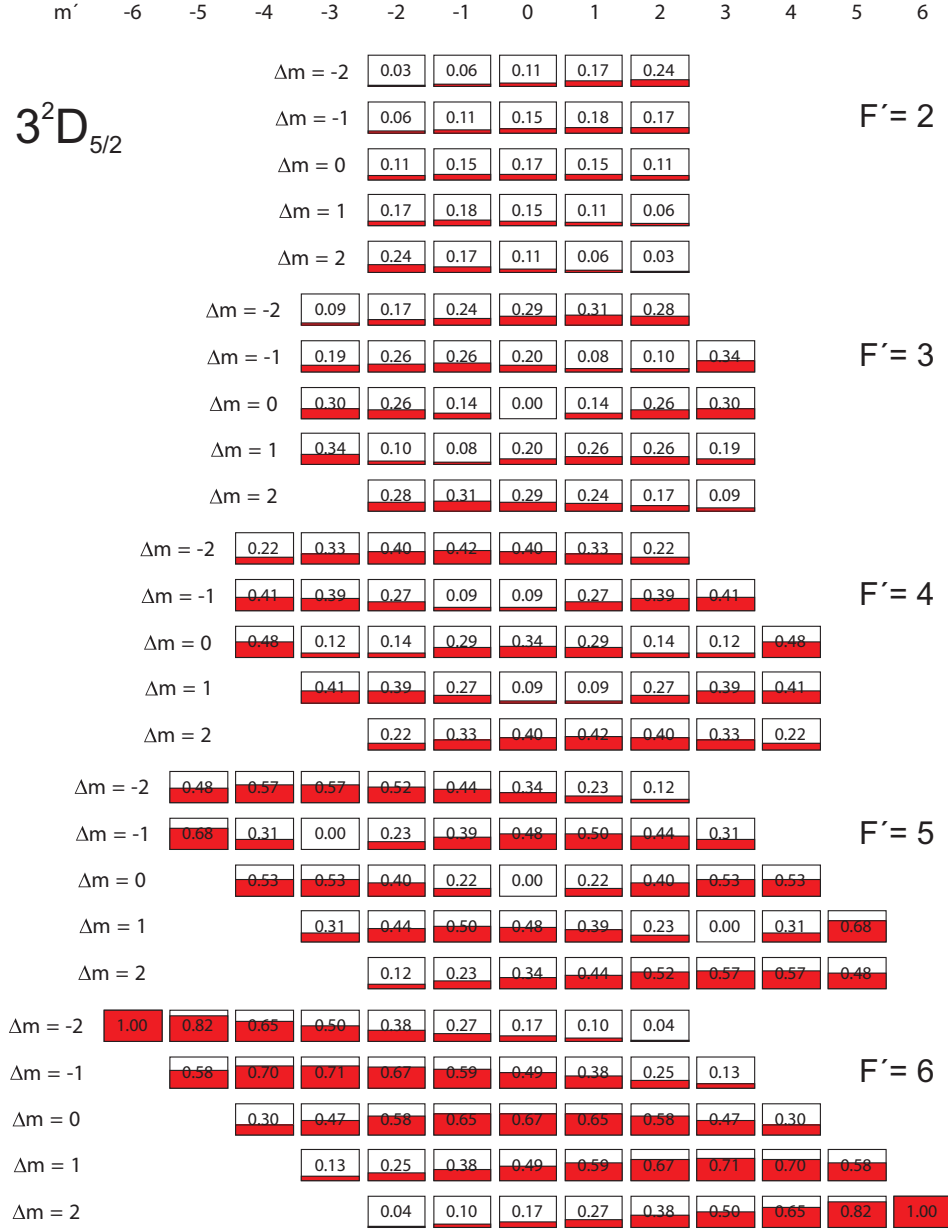


**Figure C.1.:** Coupling strength  $\Lambda(F, m, F', m')$  for the  $^{43}\text{Ca}^+$  quadrupole transitions  $S_{1/2}(F=4, m) \leftrightarrow D_{5/2}(F', m')$  with  $\Delta m = m' - m$  neglecting the geometry and polarization dependence. Figure taken from [94].

---

## D. Journal Publications

The work described in this thesis gave rise to a number of journal publications which are:

1. "High-fidelity entanglement of  $^{43}\text{Ca}^+$  hyperfine clock states."  
G.Kirchmair, J.Benhelm, F.Zähringer, R.Gerritsma, C.F.Roos & R.Blatt  
*Phys. Rev. A*, **79**, 020304 (2009)
2. "Deterministic entanglement of ions in thermal states of motion."  
G.Kirchmair, J.Benhelm, F.Zähringer, R.Gerritsma, C.F.Roos & R. Blatt  
*New J. Phys.*, **11**, 023002 (2009)
3. "State-independent experimental test of quantum contextuality".  
G. Kirchmair, F. Zähringer, R. Gerritsma, M. Kleinmann, O.Gühne, A.Cabello, R.Blatt & C.F.Roos  
*Nature* **460**, 494 (2009).
4. "Quantum simulation of the Dirac equation."  
R. Gerritsma, G.Kirchmair, F. Zähringer, E.Solano, R.Blatt & C.F.Roos  
*Nature* **463**, 68 (2010)

Further articles that have been published in the framework of this thesis:

5. "Measurement of the hyperfine structure of the  $S_{1/2}$ - $D_{5/2}$  transition in  $^{43}\text{Ca}^+$ ."  
J.Benhelm, G.Kirchmair, U. Rapol, T.Körber, C.F.Roos & R.Blatt,  
*Phys. Rev. A*, **75**, 032506 (2007)
6. "Towards fault-tolerant quantum computing with trapped ions."  
J.Benhelm, G.Kirchmair, C.F.Roos & R.Blatt  
*Nat. Phys.* **4**, 463 (2008)
7. "Experimental quantum-information processing with  $^{43}\text{Ca}^+$  ions."  
J.Benhelm, G.Kirchmair, C.F.Roos & R.Blatt  
*Phys. Rev. A* **77**, 062306 (2008)
8. "Precision measurement of the branching fractions of the  $^4P_{3/2}$  decay of Ca II."  
R. Gerritsma, G. Kirchmair, F. Zähringer, J. Benhelm, R. Blatt, C. F. Roos *Eur. Phys. J. D* **50**,13 (2008)
9. "Absolute Frequency Measurement of the  $^{40}\text{Ca}^+$   $4s^2S_{1/2} - 3d^2D_{5/2}$  Clock Transition."  
M. Chwalla, J. Benhelm, K. Kim, G. Kirchmair, T. Monz, M. Riebe, P. Schindler, A. S. Villar, W. Hänsel, C. F. Roos, R. Blatt, M. Abgrall, G. Santarelli, G. D. Rovera, Ph. Laurent  
*Phys. Rev. Lett.* **102**, 023002 (2009).

10. "Realization of a quantum walk with one and two trapped ions."  
F. Zähringer, G. Kirchmair, R. Gerritsma, E. Solano, R. Blatt & C.F. Roos  
*Phys. Rev. Lett.* **104** 100503 (2010)
11. "Compatibility and noncontextuality for sequential measurements."  
O. Gühne, M. Kleinmann, A. Cabello, J.-A. Larsson, G. Kirchmair, F. Zähringer, R. Gerritsma, C.F. Roos  
*Phys. Rev. A* **81**, 022121 (2010)

---

## Bibliography

- [1] Benioff, P. *Phys. Rev. Lett.* **48**, 1581 (1982).
- [2] Feynman, R. *Int. J. Theoret. Phys.* **21**, 467–488 (1982).
- [3] Shor, P. W. In *Proceedings of the 35th Annual Symposium on Foundations of Computer Science, Santa Fe, NM, Nov. 20-22, IEEE Computer Society Press, pp. 124–134*, (1994).
- [4] Grover, L. K. *Proceeding of the 28th ACM STOC* , 212 (1996).
- [5] Barenco, A., Bennett, C. H., Cleve, R., DiVincenzo, D. P., Margolus, N., Shor, P., Sleator, T., Smolin, J. A., and Weinfurter, H. *Phys. Rev. A* **52**(5), 3457–3467 (1995).
- [6] DiVincenzo, D. P. *Phys. Rev. A* **51**, 1015 (1995).
- [7] DiVincenzo, D. P. *Fortschr. Phys.* **48**, 771–783 (2000).
- [8] Gershenfeld, N. A. and Chuang, I. L. *Science* **275**(5298), 350–356 (1997).
- [9] Makhlin, Y., Schön, G., and Shnirman, A. *Rev. Mod. Phys.* **73**, 357 (2001).
- [10] Majer, J., Chow, J. M., Gambetta, J. M., Koch, J., Johnson, B. R., Schreier, J. A., Frunzio, L., Schuster, D. I., Houck, A. A., Wallraff, A., Blais, A., Devoret, M. H., Girvin, S. M., and Schoelkopf, R. J. *Nature* **449**, 443–447 (2007).
- [11] Loss, D. and DiVincenzo, D. P. *Phys. Rev. A* **57**, 120 (1998).
- [12] Briegel, H. J., Calarco, T., Jaksch, D., Cirac, J., and Zoller, P. *J. Mod. Opt* **47**, 415 (2000).
- [13] Knill, E., Laflamme, R., and Milburn, G. J. *Nature* **409**, 46–52 (2001).
- [14] Cirac, J. I. and Zoller, P. *Phys. Rev. Lett.* **74**(20), 4091–4094 (1995).
- [15] Vandersypen, L. M. K. and Chuang, I. L. *Rev. Mod. Phys.* **76**, 1037 (2004).
- [16] Steffen, M., Ansmann, M., Bialczak, R. C., Katz, N., Lucero, E., McDermott, R., Neeley, M., Weig, E. M., Cleland, A. N., and Martinis, J. M. *Science* **313**, 1423–1425 (2006).
- [17] Plantenberg, J. H., de Groot, P. C., Harmans, C. J. P. M., and Mooij, J. E. *Nature* **447**, 836–839 (2007).
- [18] DiCarlo, L., Chow, J. M., Gambetta, J. M., Bishop, L. S., Johnson, B. R., Schuster, D. I., Majer, J., Blais, A., Frunzio, L., and Schoelkopf, R. J. *Nature* **460**, 240 (2009).
- [19] Clarke, J. and Wilhelm, F. *Nature* **453**, 1031 (2008).

- 
- [20] Karski, M., Förster, L., Choi, J.-M., Steffen, A., Alt, W., Meschede, D., and Widera, A. *Science* **325**, 174–177 (2009).
- [21] Bloch, I. *Nature* **453**, 1016–1022 (2008).
- [22] Hofstetter, W., Cirac, J. I., Zoller, P., Demler, E., and Lukin, M. D. *Phys. Rev. Lett.* **89**, 220407 (2002).
- [23] Häffner, H., Roos, C., and Blatt, R. *Physics Reports* **469**, 155 (2008).
- [24] Wineland, D., Bergquist, J., Itano, W., and Drullinger, R. *Opt. Lett.* **5**, 254 (1980).
- [25] Nagourney, W., Sandberg, J., and Dehmelt, H. *Phys. Rev. Lett.* **56**(26), 2797–2799 (1986).
- [26] Sauter, T., Neuhauser, W., Blatt, R., and Toschek, P. E. *Phys. Rev. Lett.* **57**(14), 1696–1698 (1986).
- [27] Bergquist, J. C., Hulet, R. G., Itano, W. M., and Wineland, D. J. *Phys. Rev. Lett.* **57**(14), 1699–1702 (1986).
- [28] Bollinger, J. J., Heinzen, D. J., Itano, W. M., Gilbert, S. L., and Wineland, D. J. *IEEE Trans. Instr. Meas.* **40**, 126–128 (1991).
- [29] Diedrich, F., Peik, E., Chen, J. M., Quint, W., and Walther, H. *Phys. Rev. Lett.* **59**(26), 2931–2934 (1987).
- [30] Wineland, D. J., Bergquist, J. C., Itano, W. M., Bollinger, J. J., and Manney, C. H. *Phys. Rev. Lett.* **59**(26), 2935–2938 (1987).
- [31] Raizen, M. G., Gilligan, J. M., Bergquist, J. C., Itano, W. M., and Wineland, D. J. *Phys. Rev. A* **45**(9), 6493–6501 (1992).
- [32] Kingdon, K. *Phys. Rev.* **21**, 408 (1923).
- [33] Monroe, C., Meekhof, D. M., King, B. E., Itano, W. M., and Wineland, D. J. *Phys. Rev. Lett.* **75**(25), 4714–4717 (1995).
- [34] Sackett, C. A., Kielpinski, D., King, B. E., Langer, C., Meyer, V., Myatt, C. J., Rowe, M., Turchette, Q. A., Itano, W. M., Wineland, D. J., and Monroe, C. *Nature* **404**, 256–259 (2000).
- [35] DeMarco, B., Ben-Kish, A., Leibfried, D., Meyer, V., Rowe, M., Jelenković, B. M., Itano, W. M., Britton, J., Langer, C., Rosenband, T., and Wineland, D. J. *Phys. Rev. Lett.* **89**(26), 267901 (2002).
- [36] Schmidt-Kaler, F., Häffner, H., Riebe, M., Gulde, S., Lancaster, G. P. T., Deuschle, T., Becher, C., Roos, C. F., Eschner, J., and Blatt, R. *Nature* **422**, 408–411 (2003).
- [37] Leibfried, D., Blatt, R., Monroe, C., and Wineland, D. *Rev. Mod. Phys.* **75**, 281 (2003).
- [38] Haljan, P. C., Brickman, K.-A., Deslauriers, L., Lee, P. J., and Monroe, C. *Phys. Rev. Lett.* **94**(15), 153602 (2005).

## Bibliography

---

- [39] Home, J. P., McDonnell, M. J., Lucas, D. M., Imreh, G., Keitch, B. C., Szwer, D. J., Thomas, N. R., Webster, S. C., Stacey, D. N., and Steane, A. M. *New J. Phys.* **8**, 188 (2006).
- [40] Benhelm, J., Kirchmair, G., Roos, C. F., and Blatt, R. *Nat. Phys.* **4**, 463–466 (2008).
- [41] Riebe, M., Häffner, H., Roos, C. F., Hänsel, W., Benhelm, J., Lancaster, G. P. T., Körber, T. W., Becher, C., Schmidt-Kaler, F., James, D. F. V., and Blatt, R. *Nature* **429**, 734–737 (2004).
- [42] Barrett, M. D., Chiaverini, J., Schaetz, T., Britton, J., Itano, W. M., Jost, J. D., Knill, E., Langer, C., Leibfried, D., Ozeri, R., and Wineland, D. J. *Nature* **429**, 737–739 (2004).
- [43] Chiaverini, J., Leibfried, D., Schaetz, T., Barrett, M. D., Blakestad, R. B., Britton, J., Itano, W. M., Jost, J. D., Knill, E., Langer, C., Ozeri, R., and Wineland, D. J. *Nature* **432**, 602–605 (2004).
- [44] Reichle, R., Leibfried, D., Knill, E., Britton, J., Blakestad, R. B., Jost, J. D., Langer, C., Ozeri, R., Seidelin, S., and Wineland, D. J. *Nature* **443**, 838–841 (2006).
- [45] Leibfried, D., Knill, E., Seidelin, S., Britton, J., Blakestad, R. B., Chiaverini, J., Hume, D. B., Itano, W. M., Jost, J. D., Langer, C., Ozeri, R., Reichle, R., and Wineland, D. J. *Nature* **438**(7068), 639–642 (2005).
- [46] Häffner, H., Hänsel, W., Roos, C. F., Benhelm, J., Chek-al-Kar, D., Chwalla, M., Körber, T., Rapol, U. D., Riebe, M., Schmidt, P. O., Becher, C., Gühne, O., Dür, W., and Blatt, R. *Nature* **438**, 643–646 (2005).
- [47] Gulde, S. *Experimental realization of quantum gates and the Deutsch-Josza algorithm with trapped  $^{40}\text{Ca}^+$ -ions*. PhD thesis, Universität Innsbruck, (2003).
- [48] Brickman, K.-A., Haljan, P. C., Lee, P. J., Acton, M., Deslauriers, L., and Monroe, C. *Phys. Rev. A* **72**, 050306–1 (2005).
- [49] Roos, C. F., Lancaster, G. P. T., Riebe, M., Häffner, H., Hänsel, W., Gulde, S., Becher, C., Eschner, J., Schmidt-Kaler, F., and Blatt, R. *Phys. Rev. Lett.* **92**, 220402 (2004).
- [50] Riebe, M., Kim, K., Schindler, P., Monz, T., Schmidt, P. O., Körber, T. K., Hänsel, W., Häffner, H., Roos, C. F., and Blatt, R. *Phys. Rev. Lett.* **97**, 220407 (2006).
- [51] Kielpinski, D., Meyer, V., Rowe, M. A., Sackett, C. A., Itano, W. M., Monroe, C., and Wineland, D. J. *Science* **291**(5506), 1013–1015 (2001).
- [52] Monz, T., Kim, K., Villar, A. S., Schindler, P., Chwalla, M., Riebe, M., Roos, C. F., Häffner, H., Hänsel, W., Hennrich, M., and Blatt, R. *Phys. Rev. Lett.* **103**, 200503 (2009).
- [53] Moehring, D. L., Maunz, P., Olmschenk, S., Younge, K. C., Matsukevich, D. N., Duan, L.-M., and Monroe, C. *Nature* **449**, 68–71 (2007).
- [54] Olmschenk, S., Matsukevich, D. N., Maunz, Hayes, Duan, M., and Monroe, C. *Science* **323**, 486 (2009).

- 
- [55] Home, J. P., Hanneke, D., Jost, J. D., Amini, J. M., Leibfried, D., and Wineland, D. J. *Science* **325**, 1227–1230 (2009).
- [56] Hanneke, D., Home, J. P., Jost, J. D., Amini, J. M., Leibfried, D., and Wineland, D. J. *Nat. Phys.* **6**, 13 (2009).
- [57] Shor, P. W. *Phys. Rev. A* **52**(4), R2493–R2496 (1995).
- [58] Steane, A. M. *Phys. Rev. Lett.* **77**(5), 793–797 (1996).
- [59] Shor, P. *37th Annual Symposium on Foundations of Computer Science (FOCS '96)* **00**, 56 (1996).
- [60] Knill, E. *Nature* **434**, 39–44 (2005).
- [61] Raussendorf, R. and Harrington, J. *Phys. Rev. Lett.* **98**, 190504 (2007).
- [62] Reichardt, B. W. *arXiv:quant-ph/0406025* (2004).
- [63] Friedenauer, H., Schmitz, H., Glueckert, J., Porras, D., and Schaetz, T. *Nat. Phys.* **4**, 757–761 (2008).
- [64] Einstein, A., Podolsky, B., and Rosen, N. *Phys. Rev.* **47**, 777–780 (1935).
- [65] Bell, J. *Physics* **1**, 195 (1965).
- [66] Weihs, G., Jennewein, T., Simon, C., Weinfurter, H., and Zeilinger, A. *Phys. Rev. Lett.* **81**, 5039–5043 (1998).
- [67] Aspect, A., Grangier, P., and Roger, G. *Phys. Rev. Lett.* **49**, 91–94 (1982).
- [68] Tittel, W., Brendel, J., Zbinden, H., and Gisin, N. *Phys. Rev. Lett.* **81**, 3563–3566 (1998).
- [69] Rowe, M. A., Kielpinski, D., Meyer, V., Sackett, C. A., Itano, W. M., Monroe, C., and Wineland, D. J. *Nature* **409**, 791–794 (2001).
- [70] Specker, E. *Dialectica* **14**, 239–246 (1960).
- [71] Kochen, S. and Specker, E. P. *J. Math. Mech.* **17**, 59–87 (1967).
- [72] Bell, J. S. *Rev. Mod. Phys.* **38**, 447–452 (1966).
- [73] Amselem, E., Rådmark, M., Bourennane, M., and Cabello, A. *Phys. Rev. Lett.* **103**, 160405 (2009).
- [74] Moussa, O., Ryan, C. A., Cory, D. G., and Laflamme, R. *arXiv:0912.0485* (2009).
- [75] Kirchmair, G., Zähringer, F., Gerritsma, R., Kleinmann, M., O., G., Cabello, A., Blatt, R., and Roos, C. F. *Nature* **460**, 494 (2009).
- [76] Kirchmair, G., Benhelm, J., Zähringer, F., Gerritsma, R., Roos, C. F., and Blatt, R. *New J. Phys.* **11**, 023002 (2009).

## Bibliography

---

- [77] Kirchmair, G., Benhelm, J., Zähringer, F., Gerritsma, R., Roos, C. F., and Blatt, R. *Phys. Rev. A* **79**, 020304(R) (2009).
- [78] Gerritsma, R., Kirchmair, G., Zähringer, F., Solano, E., Blatt, R., and Roos, C. F. *Nature* **463**, 68 (2010).
- [79] Nielsen, M. A. and Chuang, I. L. *Quantum computation and quantum information*. Cambridge Univ. Press, Cambridge, (2000).
- [80] Sørensen, A. and Mølmer, K. *Phys. Rev. Lett.* **82**, 1971–1974 (1999).
- [81] Sørensen, A. and Mølmer, K. *Phys. Rev. A* **62**, 022311 (2000).
- [82] Clauser, J. and Shimony, A. *Rep. Prog. Phys.* **41**, 1883 (1978).
- [83] Everett, H. *Rev. Mod. Phys.* **29**, 454 (1957).
- [84] Gröblacher, S., Paterek, T., Kaltenbaek, R., Brukner, S., Zdotukowski, M., Aspelmeyer, M., and Zeilinger, A. *Nature* **446**, 871 (2007).
- [85] Rauschenbeutel, A., Nogues, G., Osnaghi, S., Bertet, P., Brune, M., Raimond, J. M., and Haroche, S. *Science* **288**(5473), 2024–2028 (2000).
- [86] Aspelmeyer, M., Böm, H. R., Gyatso, T., Jennewein, T., Kaltenbaek, R., Lindenthal, M., Molina-Terriza, G., Poppe, A., Resch, K., Taraba, M., Ursin, R., Walther, P., and Zeilinger, A. *Science* **301**, 621–623 (2003).
- [87] Mandel, O., Greiner, M., Widera, A., Rom, T., Hänsch, T. W., and Bloch, I. *Phys. Rev. Lett.* **91**, 010407 (2003).
- [88] Jennewein, T., Simon, C., Weihs, G., Weinfurter, H., and Zeilinger, A. *Phys. Rev. Lett.* **84**(20), 4729–4732 (2000).
- [89] Raussendorf R., Browne D., B. I. J. *Phys. Rev. A* **68**, 022312 (2003).
- [90] Cohen-Tannoudji, Bernard Diu, F. L. *Quantum mechanics I + II*. Wiley, (1977).
- [91] Haroche, S. and Raimond, J.-M. *Exploring the quantum*. Oxford Univ. Press, Oxford, (2006).
- [92] Roos, C. *Controlling the quantum state of trapped ions*. PhD thesis, Universität Innsbruck, (2000).
- [93] Riebe, M. *Preparation of entangled states and quantum teleportation with atomic qubits*. PhD thesis, Universität Innsbruck, (2005).
- [94] Benhelm, J. *Precision spectroscopy and quantum information processing with trapped calcium ions*. PhD thesis, Universität Innsbruck, (2008).
- [95] Gerritsma, R., Kirchmair, G., Zähringer, F., Benhelm, J., Blatt, R., and Roos, C. *Eur. Phys. J. D* **50** (2008).

- 
- [96] Barton, P. A., Donald, C. J. S., Lucas, D. M., Stevens, D. A., Steane, A. M., and Stacey, D. N. *Phys. Rev. A* **62**, 032503 (2000).
- [97] Jin, J. and Church, D. A. *Phys. Rev. Lett.* **70**, 3213–3216 (1993).
- [98] James, D. F. V. *Appl. Phys. B* **66**, 181–190 (1998).
- [99] Arbes, F., Benzing, M., Gudjons, T., Kurth, F., and Werth, G. *Z. Phys. D* **31**, 27–30 (1994).
- [100] Nörtershauser, W., Blaum, K., Icker, K., Muller, P., Schmitt, A., Wendt, K., and Wiche, B. *Eur. Phys. J. D*, 33–39 (1998).
- [101] Breit, G. and Rabi, I. I. *Phys Rev* **38**, 2082 (1931).
- [102] Benhelm, J., Kirchmair, G., Roos, C. F., and Blatt, R. *Phys. Rev. A* **77**, 062306 (2008).
- [103] Häffner, H., Gulde, S., Riebe, M., Lancaster, G., Becher, C., Eschner, J., Schmidt-Kaler, F., and Blatt, R. *Phys. Rev. Lett.* **90**, 143602 (2003).
- [104] Loudon, R. *The Quantum Theory of Light*. Oxford Univ. Press, (1973).
- [105] Schindler, P. Master’s thesis, Universität Innsbruck, (2007).
- [106] Johanning, M., Braun, A., Timoney, N., Elman, V., Neuhauser, W., and Wunderlich, C. *Phys. Rev. Lett.* **102**, 073004 (2009).
- [107] Ospelkaus, C., Langer, C. E., Amini, J. M., Brown, K. R., Leibfried, D., and Wineland, D. J. *Phys. Rev. Lett.* **101**, 090502 (2008).
- [108] Lee, P. J., Brickman, K. A., Deslauriers, L., Haljan, P. C., Duan, L., and Monroe, C. *J. Opt. B* **7**, 371 (2005).
- [109] Leibfried, D., DeMarco, B., Meyer, V., Lucas, D., Barrett, M., Britton, J., Itano, W. M., Jelenković, B., Langer, C., Rosenband, T., and Wineland, D. J. *Nature* **422**, 412–415 (2003).
- [110] Milburn, G. J., Schneider, S., and James, D. F. *Fortschr. Phys.* **48**, 801–810 (2000).
- [111] Solano, E., de Matos Filho, R. L., and Zagury, N. *Phys. Rev. A* **59**, R2539–R2543 (1999).
- [112] Roos, C. F., Monz, T., Kim, K., Riebe, M., Häffner, H., James, D. F. V., and Blatt, R. *Phys. Rev. A* **77**, 040302(R) (2008).
- [113] Schmidt-Kaler, F., Häffner, H., Gulde, S., Riebe, M., Lancaster, G. P. T., Deuschle, T., Becher, C., Hänsel, W., Eschner, J., Roos, C. F., and Blatt, R. *Appl. Phys. B* **77**, 789 (2003).
- [114] Unanyan, R. G. and Fleischhauer, M. *Phys. Rev. Lett.* **90**, 133601 (2003).
- [115] Lougovski, P., Walther, H., and Solano, E. *Eur. Phys. J. D* **38**, 423–426 (2006).
- [116] Santos, M. F., Giedke, G., and Solano, E. *Phys. Rev. Lett.* **98**, 020401 (2007).
- [117] Lamata, L., León, J., Schätz, T., and Solano, E. *Phys. Rev. Lett.* **98**, 253005 (2007).

## Bibliography

---

- [118] Kirchmair, G. Master's thesis, Universität Innsbruck, (2007).
- [119] Notcutt, M., Ma, L.-S., Ye, J., and Hall, J. L. *Opt. Lett.* **30**, 1815–1817 (2005).
- [120] Drever, R. W. P., Hall, J. L., Kowalski, F. V., Hough, J., Ford, G. M., Munley, A. J., and Ward, H. *Appl. Phys. B* **31**, 97–105 (1983).
- [121] Ma, L., Jungner, P., Ye, J., and Hall, J. L. *Opt. Lett.* **19**, 1777 (1994).
- [122] Chwalla, M. *Precision spectroscopy with  $^{40}\text{Ca}^+$  ions in a Paul trap*. PhD thesis, Institute for Experimental Physics, Innsbruck, (2009).
- [123] Pham, P. T. T. Master's thesis, Massachusetts Institute of Technology, (2005).
- [124] Rotter, D. Master's thesis, University of Innsbruck, (2003).
- [125] Ramsey, N. F. *Phys. Rev.* **78**, 695–699 (1950).
- [126] Benhelm, J., Kirchmair, G., Rapol, U., Körber, T., Roos, C. F., and Blatt, R. *Phys. Rev. A* **75**, 032506 (2007).
- [127] Kielpinski, D., Monroe, C., and Wineland, D. J. *Nature* **417**, 709–711 (2002).
- [128] Hensinger, W. K., Olmschenk, S., Stick, D., Hucul, D., Yeo, M., Acton, M., Deslauriers, L., and Monroe, C. *Appl. Phys. Lett.* **88**, 034101 (2006).
- [129] Blakestad, R. B., Ospelkaus, C., VanDevender, A. P., Amini, J. M., Britton, J., Leibfried, D., and Wineland, D. J. *Phys. Rev. Lett.* **102**, 153002 (2009).
- [130] Splatt, F., Harlander, M., Brownnutt, M., Zähringer, F., Blatt, R., and Hänsel, W. *New J. Phys.* **11**, 103008 (2009).
- [131] Home, J. P. and Steane, A. M. *Quant. Inf. Comp.* **6**, 289 (2006).
- [132] Turchette, Q. A., Kielpinski, King, B. E., Leibfried, D., Meekhof, D. M., Myatt, C. J., Rowe, M. A., Sackett, C. A., Wood, C. S., Itano, W. M., Monroe, C., and Wineland, D. J. *Phys. Rev. A* **61**, 063418 (2000).
- [133] Deslauriers, L., Haljan, P. C., Lee, P. J., Brickman, K.-A., Blinov, B. B., Madsen, M. J., and Monroe, C. *Phys. Rev. A* **70**, 043408 (2004).
- [134] Labaziewicz, J., Ge, Y., Antohi, P., Leibbrandt, D., Brown, K., and Chuang, I. *Phys. Rev. Lett.* **100**, 013001 (2008).
- [135] Nebendahl, V., Häffner, H., and Roos, C. F. *Phys. Rev. A* **79**, 012312 (2009).
- [136] Hradil, Z., Řeháček, J., Fiurášek, J., and Ježek, M. *Lect. Notes Phys.* **649**, 59–112 (2004).
- [137] Ježek, M., Fiurášek, J., and Hradil, Z. *Phys. Rev. A* **68**, 012305 (2003).
- [138] Steane, A. *Rep. Prog. Phys.* **61**, 117–173 (1998).

- 
- [139] Rowe, M. A., Ben-Kish, A., DeMarco, B., Leibfried, D., Meyer, V., Beall, J., Britton, J., Hughes, J., Itano, W. M., Jelenković, B., Langer, C., Rosenband, T., and Wineland, D. J. *Quant. Inf. Comp.* **2**, 257–271 (2002).
- [140] Blinov, B., Deslauriers, L., Lee, P., Madsen, M., Miller, R., and Monroe, C. *Phys. Rev. A* **65**, 040304 (2002).
- [141] Barrett, M. D., DeMarco, B., Schaetz, T., Leibfried, D., Britton, J., Chiaverini, J., Itano, W. M., Jelenković, B., Jost, J. D., Langer, C., Rosenband, T., and Wineland, D. J. *Phys. Rev. A* **68**, 042302 (2003).
- [142] Harris, F. J. *Proc. IEEE* **66**, 51–83 (1978).
- [143] Leibfried, D., Barrett, M. D., Schaetz, T., Britton, J., Chiaverini, J., Itano, W. M., Jost, J. D., Langer, C., and Wineland, D. J. *Science* **304**, 1476–1478 (2004).
- [144] Haljan, P. C., Lee, P. J., Brickman, K.-A., Acton, M., Deslauriers, L., and Monroe, C. *Phys. Rev. A* **72**, 062316 (2005).
- [145] Leibfried, D., Knill, E., Ospelkaus, C., and Wineland, D. J. *Phys. Rev. A* **76**, 032324 (2007).
- [146] Roos, C. F. *New J. Phys.* **10**, 013002 (2008).
- [147] Langer, C., Ozeri, R., Jost, J. D., Chiaverini, J., DeMarco, B., Ben-Kish, A., Blakestad, R. B., Britton, J., Hume, D. B., Itano, W. M., Leibfried, D., Reichle, R., Rosenband, T., Schaetz, T., Schmidt, P. O., and Wineland, D. J. *Phys. Rev. Lett.* **95**, 060502 (2005).
- [148] Olmschenk, S., Younge, K. C., Moehring, D. L., Matsukevich, D. N., Maunz, P., and Monroe, C. *Phys. Rev. A* **76**, 052314 (2007).
- [149] Kim, K., Chang, M., Islam, R., Korenblit, S., Duan, L., and Monroe, C. *Phys. Rev. Lett.* **103**, 120502 (2009).
- [150] Nebendahl, V. Master’s thesis, University of Innsbruck, (2008).
- [151] Wang, X., Sørensen, A., and Mølmer, K. *Phys. Rev. Lett.* **86**(17), 3907–3910 (2001).
- [152] Myerson, A. H., Szwer, D. J., Webster, S. C., Allcock, D. T. C., Curtis, M. J., Imreh, G., Sherman, J. A., Stacey, D. N., Steane, A. M., and Lucas, D. M. *Phys. Rev. Lett.* **100**, 200502 (2008).
- [153] Knill, E., Leibfried, D., Reichle, R., Britton, J., Blakestad, R. B., Jost, J. D., Langer, C., Ozeri, R., Seidelin, S., and Wineland, D. J. *Phys. Rev. A* **77**, 012307 (2008).
- [154] Benhelm, J., Kirchmair, G., Roos, C. F., and Blatt, R. *arXiv:0804.1261* (2008).
- [155] Lucas, D. M., Keitch, B. C., Home, J. P., Imreh, G., McDonnell, M. J., Stacey, D. N., Szwer, D. J., and Steane, A. M. *arXiv: 0710.4421v1* (2007).
- [156] Bohr, N. *Phys. Rev.* **48**, 696–702 (1935).

## Bibliography

---

- [157] Cabello, A. and García-Alcaine, G. *Phys. Rev. Lett.* **80**, 1797–1799 (1998).
- [158] Meyer, D. A. *Phys. Rev. Lett.* **83**, 3751–1754 (1999).
- [159] Cabello, A. *Phys. Rev. Lett.* **101**, 210401 (2008).
- [160] Gühne, O., Kleinmann, M., Cabello, A., Larsson, J., Kirchmair, G., Zähringer, F., Gerritsma, R., and Roos, C. *arXiv:0912.4846* (2010).
- [161] Peres, A. *Phys. Lett. A* **151**, 107–108 (1990).
- [162] Mermin, N. D. *Phys. Rev. Lett.* **65**, 3373—3376 (1990).
- [163] Garay, L. J., Anglin, J. R., Cirac, J. I., and Zoller, P. *Phys. Rev. Lett.* **85**, 4643–4647 (2000).
- [164] Schliemann, J., Loss, D., and Westervelt, R. M. *Phys. Rev. Lett.* **94**, 206801 (2005).
- [165] Cserti, J. and Dávid, G. *Phys. Rev. B* **74**, 172305 (2006).
- [166] Katsnelson, M. I., Novoselov, K. S., and Geim, A. K. *Nat. Phys.* **2**, 620–625 (2006).
- [167] Neto, A. H. C., Guinea, F., Peres, N. M. R., Novoselov, K. S., and Geim, A. K. *Rev. Mod. Phys.* **81**, 109–162 (2009).
- [168] Thaller, B. *The Dirac equation*. Springer-Verlag, (1992).
- [169] Anderson, C. D. *Phys. Rev.* **43**, 491–494 (1933).
- [170] Klein, O. *Z. Phys.* **53**, 157–165 (1929).
- [171] Schrödinger, E. *Sitz. Preuss. Akad. Wiss. Phys.-Math. Kl.* **24**, 418–428 (1930).
- [172] Bermudez, A., Martin-Delgado, M. A., and Solano, E. *Phys. Rev. A* **76**, 041801(R) (2007).
- [173] Zhang, X. *Phys. Rev. Lett.* **100**, 113903 (2008).
- [174] Vaishnav, J. Y. and Clark, C. W. *Phys. Rev. Lett.* **100**, 153002 (2008).
- [175] Otterbach, J., Unanyan, R. G., and Fleischhauer, M. *Phys. Rev. Lett.* **102**, 063602 (2009).
- [176] Leibfried, D., DeMarco, B., Meyer, V., Rowe, M., Ben-Kish, A., Britton, J., Itano, W. M., Jelenković, B., Langer, C., Rosenband, T., and Wineland, D. J. *Phys. Rev. Lett.* **89**, 247901 (2002).
- [177] Porras, D. and Cirac, J. I. *Phys. Rev. Lett.* **92**, 207901 (2004).
- [178] Johanning, M., Varón, A. F., and Wunderlich, C. *J. Phys. B* **42**, 154009 (2009).
- [179] Thaller, B. *arXiv:quant-ph/0409079* (2004).
- [180] Schwabl, F. *Quantenmechanik für Fortgeschrittene*. Springer, (2005).
- [181] Krekora, P., Su, Q., and Grobe, R. *Phys. Rev. Lett.* **93**, 043004 (2004).

- 
- [182] Wang, Z.-Y. and Xiong, C.-D. *Phys. Rev. A* **77**, 045402 (2008).
- [183] Wallentowitz, S. and Vogel, W. *Phys. Rev. Lett.* **75**, 2932–2935 (1995).
- [184] Meekhof, D. M., Monroe, C., King, B. E., Itano, W. M., and Wineland, D. J. *Phys. Rev. Lett.* **76**(11), 1796–1799 (1996).
- [185] García-Ripoll, J. J., Zoller, P., and Cirac, J. I. *Phys. Rev. Lett.* **91**(15), 157901 (2003).
- [186] Zähringer, F., Kirchmair, G., Gerritsma, R., Solano, E., Blatt, R., and Roos, C. F. *arXiv:0911.1876* (2009).
- [187] Schmitz, H., Matjeschk, R., Schneider, C., Glueckert, J., Enderlein, M., Huber, T., and Schaetz, T. *Phys. Rev. Lett.* **103**, 090504 (2009).
- [188] Menicucci, N. C. and Milburn, G. J. *Phys. Rev. A* **76**, 052105 (2007).
- [189] Alsing, P. M., Dowling, J. P., and Milburn, G. J. *Phys. Rev. Lett.* **94**, 220401 (2005).
- [190] Porras, D., Marquardt, F., von Delft, J., and Cirac, J. I. *Phys. Rev. A* **78**, 010101 (2008).
- [191] Schützhold, R., Uhlmann, M., Petersen, L., Schmitz, H., Friedenauer, A., and Schätz, T. *Phys. Rev. Lett.* **99**, 201301 (2007).
- [192] García-Mata, I., Zhironov, O. V., and Shepelyansky, D. L. *Eur. Phys. J. D* **41**, 325–330 (2007).
- [193] Chwalla, M., Benhelm, J., Kim, K., Kirchmair, G., Monz, T., Riebe, M., Schindler, P., Villar, A. S., Hänsel, W., and Roos, C. F. *Phys. Rev. Lett.* **102**, 023002 (2009).
- [194] Kurth, F., Gudjons, T., Hilbert, B., Reisinger, T., Werth, G., and Martensson-Pendrill, A. M. Z. *Phys. D* **34**, 227–232 (1995).
- [195] Tommaseo, G., Pfeil, T., Revalde, G., Werth, G., Indelicato, P., and Desclaux, J. *Eur. Phys. J. D* **25**, 113–121 (2003).

---

# Danksagung

Das Gelingen dieser Arbeit wäre ohne die Hilfe und Geduld Vieler nicht möglich gewesen. Ihnen allen möchte hiermit herzlich danken.

An erster Stelle möchte ich mich bei Rainer Blatt bedanken, der es mir ermöglicht hat meine Diplomarbeit und jetzt auch meine Doktorarbeit in seiner Arbeitsgruppe anzufertigen. Durch sein stetiges Bemühen und seinen großen Einsatz hat er ein Klima und wissenschaftliches Umfeld geschaffen indem es eine Freude ist zu arbeiten.

Ein großer Dank gebührt natürlich Christian Roos. Viele der in dieser Arbeit vorgestellten Experimente waren nur durch seine Ideen und Unterstützung möglich. Besonders Bedanken möchte ich mich auch für das Korrekturlesen meiner Arbeit.

Meine Arbeitsweise im Labor wurde am meisten durch Jan Benhelm geprägt. In den vier Jahren unserer Zusammenarbeit konnte ich sehr viel von ihm lernen und meine Doktorarbeit profitierte sehr von seiner sorgfältigen Aufbauarbeit.

Weiters Bedanken möchte ich mich bei Rene Gerritsma und Florian Zähringer die mit mir unzählige Tage im Labor verbracht haben. Die interessanten und witzigen Unterhaltungen während der langen Stunden vor dem Laborrechner werden mir immer in guter Erinnerung bleiben.

Vielen Dank auch an die ganze  $^{40}\text{Ca}^+$ Crew für die gute Zusammenarbeit in den letzten Jahren. Besonders bedanken möchte ich mich bei Philipp Schindler für das betreuen unserer Pulse Box und Michael Chwalla für die Arbeit an den 729 nm cavities und der "real laser front".

Ein großer Dank gebührt auch der ganzen Kochgruppe die, jeden Tag, für ein sehr gutes Essen und eine gute Stimmung während der Mittagspause gesorgt hat.

Nicht zu vergessen sind natürlich meine Freunde. Einen Physiker von seiner Arbeit abzulenken ist nicht immer ganz einfach deshalb ist es ihnen zu verdanken, dass meine sozialen Kompetenzen nicht auf der Strecke geblieben sind.

Ohne die Unterstützung meiner Familie hätte ich diese Doktorarbeit wohl nicht so erfolgreich abschliessen können. Deshalb will ich mich an dieser Stelle auch recht herzlich bei ihnen bedanken.

Ein besonderer Dank gebührt meiner Freundin Astrid die mich all die Jahre durch mein Studium und meine Doktorarbeit begleitet hat. Ihr Verständnis und ihre Unterstützung haben mir geholfen auch die schwierigsten Situationen zu meistern.